

PROGRESS IN BIOMEDICAL OPTICS

Proceedings of

Applications of Ultrashort-Pulse Lasers in Medicine and Biology

Joseph Neev

Chair/Editor

29-30 January 1998

San Jose, California

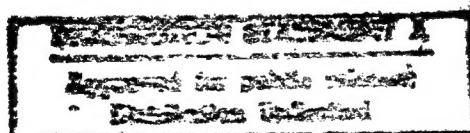
Sponsored by

Air Force Office of Scientific Research

IBOS—International Biomedical Optics Society

SPIE—The International Society for Optical Engineering

19980828 036



Volume 3255

DTIC QUALITY IMPROVED

PROGRESS IN BIOMEDICAL OPTICS

Proceedings of

Applications of Ultrashort-Pulse Lasers in Medicine and Biology

Joseph Neev
Chair/Editor

29–30 January 1998
San Jose, California

Sponsored by
Air Force Office of Scientific Research
IBOS—International Biomedical Optics Society
SPIE—The International Society for Optical Engineering

Published by
SPIE—The International Society for Optical Engineering



Volume 3255

SPIE is an international technical society dedicated to advancing engineering and scientific applications of optical, photonic, imaging, electronic, and optoelectronic technologies.



The papers appearing in this book comprise the proceedings of the meeting mentioned on the cover and title page. They reflect the authors' opinions and are published as presented and without change, in the interests of timely dissemination. Their inclusion in this publication does not necessarily constitute endorsement by the editors or by SPIE.

Please use the following format to cite material from this book:

Author(s), "Title of paper," in *Applications of Ultrashort-Pulse Lasers in Medicine and Biology*, Joseph Neev, Editor, Proceedings of SPIE Vol. 3255, page numbers (1998).

ISSN 0277-786X
ISBN 0-8194-2694-6

Published by
SPIE—The International Society for Optical Engineering
P.O. Box 10, Bellingham, Washington 98227-0010 USA
Telephone 360/676-3290 (Pacific Time) • Fax 360/647-1445

Copyright ©1998, The Society of Photo-Optical Instrumentation Engineers.

Copying of material in this book for internal or personal use, or for the internal or personal use of specific clients, beyond the fair use provisions granted by the U.S. Copyright Law is authorized by SPIE subject to payment of copying fees. The Transactional Reporting Service base fee for this volume is \$10.00 per article (or portion thereof), which should be paid directly to the Copyright Clearance Center (CCC), 222 Rosewood Drive, Danvers, MA 01923. Payment may also be made electronically through CCC Online at <http://www.directory.net/copyright/>. Other copying for republication, resale, advertising or promotion, or any form of systematic or multiple reproduction of any material in this book is prohibited except with permission in writing from the publisher. The CCC fee code is 0277-786X/98/\$10.00.

Printed in the United States of America.

Contents

v Conference Committee

SESSION 1 MODELING OF ULTRASHORT-PULSE INTERACTION WITH MATTER

2 **Ultrashort-pulse lasers: a new tool for biomedical applications [3255-01]**
J. Neev, Consultant

8 **Radially varying dispersion in high-numerical-aperture focusing [3255-03]**
M. Müller, G. J. Brakenhoff, Univ. of Amsterdam (Netherlands); U. Simon, Carl Zeiss Jena GmbH (FRG); J. A. Squier, Univ. of California/San Diego

SESSION 2 ULTRASHORT-PULSE LASERS: INSTRUMENTATION AND MEASUREMENTS

18 **Measurement and modeling of the focusing of 15-fs optical pulses with a high-numerical-aperture objective [3255-05]**
J. A. Squier, V. V. Yakovlev, Univ. of California/San Diego; M. Müller, A. H. Buist, G. J. Brakenhoff, Univ. of Amsterdam (Netherlands); U. Simon, Carl Zeiss Jena GmbH (FRG)

22 **Review of ultrashort-pulse measurement: changing the basic ultrashort-pulse experiment [3255-07]**
D. N. Fittinghoff, Univ. of California/San Diego

SESSION 3 OPHTHALMIC APPLICATIONS OF ULTRASHORT-PULSE LASERS

34 **Laser-induced breakdown in the eye at pulse durations from 80 ns to 100 fs (Invited Paper) [3255-08]**
A. Vogel, J. Noack, K. Nahen, D. Theisen, R. Birngruber, Medical Laser Ctr. Lübeck (FRG); D. X. Hammer, G. D. Noojin, B. A. Rockwell, Air Force Research Lab.

50 **Retinal damage mechanisms from ultrashort laser exposure [3255-09]**
B. A. Rockwell, D. J. Payne, R. A. Hopkins, D. X. Hammer, P. K. Kennedy, R. E. Amnote, B. Eilert, J. J. Druessel, Air Force Research Lab.; C. A. Toth, Duke Univ. Eye Ctr.; W. P. Roach, Air Force Office of Scientific Research; S. L. Phillips, Air Force Research Lab.; D. J. Stolarski, G. D. Noojin, R. J. Thomas, C. P. Cain, The Analytical Sciences Corp.

56 **Optimal laser parameters for intrastromal corneal surgery [3255-11]**
R. M. Kurtz, Univ. of Michigan and Kellogg Eye Ctr./Univ. of Michigan; C. Horvath, Univ. of Michigan and Univ. of Heidelberg (FRG); H.-H. Liu, Univ. of Michigan; T. Juhasz, Univ. of Michigan and Kellogg Eye Ctr./Univ. of Michigan

67 **Laser spot size as a function of tissue depth and laser wavelength in human sclera [3255-12]**
Z. S. Sacks, Univ. of Michigan; R. M. Kurtz, Univ. of Michigan and Kellogg Eye Ctr./Univ. of Michigan; R. Fenn, Kellogg Eye Ctr./Univ. of Michigan; F. H. Loesel, Univ. of Heidelberg (FRG); G. A. Mourou, Univ. of Michigan; T. Juhasz, Univ. of Michigan and Kellogg Eye Ctr./Univ. of Michigan

77 **Damage mechanisms of pico- and femtosecond laser retinal lesions as viewed by electron microscopy [3255-22]**
C. A. Toth, E. K. Chiu, J. M. Jumper, Duke Univ. Medical Ctr.; B. A. Rockwell, Air Force Research Lab.

SESSION 4 ABLATION WITH ULTRASHORT-PULSE LASERS: SURGICAL APPLICATIONS

84 **Ultrashort laser pulses in dentistry: advantages and limitations (Invited Paper) [3255-13]**
M. H. Niemz, Univ. of Heidelberg (FRG)

92 **Plasma luminescence feedback control system for precise ultrashort-pulse laser tissue ablation [3255-14]**
B.-M. Kim, M. D. Feit, A. M. Rubenchik, D. M. Gold, C. B. Darrow, J. E. Marion, L. B. Da Silva, Lawrence Livermore National Lab.

98 **Effect of laser irradiation on the functional activity of enzymes with different structural complexity [3255-15]**
S. A. Ostrovtsova, Institute of Biochemistry (Belarus); A. P. Volodenkov, A. A. Maskevich, State Univ. of Grodno (Belarus); I. M. Artsukevich, Institute of Biochemistry (Belarus); S. S. Anufrik, State Univ. of Grodno (Belarus); A. F. Makarchikov, I. P. Chernikevich, Institute of Biochemistry (Belarus); V. I. Stepuro, State Univ. of Grodno (Belarus)

105 **Preliminary characterization of hard dental tissue ablation with femtosecond lasers [3255-16]**
J. Neev, Consultant; J. A. Squier, Univ. of California/San Diego

SESSION 5 DIAGNOSTICS AND IMAGING WITH ULTRASHORT-PULSE LASERS

118 **Optical parameter measurements by collimated light transmission [3255-19]**
A. Colasanti, G. Guida, A. Kisslinger, R. Liuzzi, M. Quarto, G. Roberti, F. Villani, Faculty of Medicine and Surgery/ Univ. of Naples Federico II (Italy)

123 *Addendum*
124 *Author Index*

Conference Committee

Conference Chair

Joseph Neev, Consultant

Program Committee

Alexander M. Rubenchik, Lawrence Livermore National Laboratory

Jeff A. Squire, University of California/San Diego

Tibor Juhasz, Kellogg Eye Center/University of Michigan

Ron M. Kurtz, M.D., Kellogg Eye Center/University of Michigan

Session Chairs

- 1 Modeling of Ultrashort-Pulse Interaction with Matter

Alexander M. Rubenchik, Lawrence Livermore National Laboratory

- 2 Ultrashort-Pulse Lasers: Instrumentation and Measurements

Jeff A. Squier, University of California/San Diego

- 3 Ophthalmic Applications of Ultrashort-Pulse Lasers

Ron M. Kurtz, M.D., Kellogg Eye Center/University of Michigan

- 4 Ablation with Ultrashort-Pulse Lasers: Surgical Applications

Joseph Neev, Consultant

- 5 Diagnostics and Imaging with Ultrashort-Pulse Lasers

Tibor Juhasz, Kellogg Eye Center/University of Michigan

SESSION 1

Modeling of Ultrashort-Pulse Interaction with Matter

Ultrashort Pulse Lasers: A New Tool for Biomedical Applications

Joseph Neev

950 Acapulco St. Laguna Beach, CA. 92651

INTRODUCTION

The past decade has brought about significant advances in Ultrashort pulse lasers technology. The development of broad-band solid state gain media opened up new possibilities for ultrashort pulse generation. In particular, the development of all-solid-state ultrashort pulse devices promise to make such devices rugged and reduce their cost.

Capitalizing on the evolving technology of ultrashort pulse lasers could result in many advantages for biomedical applications. Tissue interaction characteristics that are superior to conventional surgical technologies and other, longer pulse laser systems can be offered. The major advantages of the ultrashort pulse laser (USPL) tissue ablation method are: 1) efficient ablation due to the small input of laser energy per ablated volume of tissue and the resulting decrease of energy density needed to ablate material; 2) minimal collateral mechanical damage due to the efficient ablation and the short duration of the stress impulse; 3) minimal collateral thermal damage due to the extremely short deposition time and; 4) the ablation threshold and rate are less dependent on tissue type and condition; 5) high precision in ablation depth is achievable because only a small amount of tissue is ablated per pulse; 6) low acoustical (operating) noise level (as compared to the acoustical noise produced by other laser systems); 7) minimized pain due to localization of energy deposition and damage; 8) ability to texture surface by controlled beam profile and rastering; 9) precise spatial control: the intensity-dependent, multiphoton process self-ensures that tissue below or laterally removed from the beam focus will not experience ablative interaction, and finally, 10) since ultrashort pulses interact strongly with all matter regardless of specific

linear absorption characteristics, efficient processing of many tissue types is possible. Finally, the extremely short pulse duration allows ultrashort pulse lasers to become useful in a range of biomedical applications involving diagnostics and biomedical imaging.

Current Status of Ultrashort Pulse Laser Development

Titanium-doped sapphire (Ti:Sapphire) is the most successful laser medium used for ultrashort pulse application because it possesses a broad gain bandwidth of approximately 200nm along with favorable mechanical and thermal properties.

The Generation of Ultrashort Pulses is Currently Most Commonly Achieved Using Chirped Pulse Amplification (CPA) of Ultrashort pulses. Devices utilizing CPA allow increase in peak power to the Hundreds of Terawatt (TW) level and result in decrease of pulse duration down to < 10 fs. Diode-pumped fiber oscillator allow further reduction in size cost.

Types of CPAs

Several types of Chirped pulse oscillator are now available commercially:

Nd:glass amplify Pulses to the 1 ps range.

Ti:Sapphire or Cr:LiSAF result in amplification of pulses as short as 100fs range

and Ti:Sapphire - High average power oscillators allow amplifications to the 10 to 20 fs range

Engineering and Design Considerations

Engineering considerations should emphasize the following operating parameters:

- Stable, Consistent operation
- Compactness and Portability
- Durability and ruggedness
- Delivery
- Control

Commercially Available System include, for example -
A mode-locked, diode-pumped erbium fiber laser repetition rate of 37MHz and average powers of 50mW, (1nJ/pulse) Turn-key, self-start mode-locking; High power ultrashort pulses at 1550nm and 775nm; Fiber gain-guided cavity for ultrastable operation with superb reliability; Wall-plug or battery powered with no water; and a highly compact head (12" x 24")

Presently, an amplified Ti:Sapphire Laser System is characterized by

- Energy of mJ/pulse
- KHz repetition rates
- Pulse widths ranging from sub-50fs to over 10ps
- High contrast ratio and near bandwidth limited
- Wavelengths extending over the entire Ti:Sapphire tuning range

Alternatively, Ti:Sapphire laser systems operating at energy levels of up to 50mJ at 10-20 Hz are also available.

APPLICATIONS

Scientific and non-biomedical Applications:

- Ultrafast Pulses allow the study of physical phenomena that occur in extremely short time scales (picosecond and femtoseconds) and the study of high-speed dynamics
- Snapshots in this time domain reveal the most fundamental mechanisms of molecular, atomic, and electron interactions. Sub 100 fs pulses can probe the rotational and vibrational dynamics of atomic systems such as molecules and condensed matter.
- Monitoring of molecular motion in liquids or gases, and studying of how electrons collide in semiconductors and superconductors, electrons, excitons, and phonons in various condensed-matter media
- Quantum Control of NaI Photo-dissociation Reaction Product States by Ultrafast Tailored Light Pulses
- Studies of high intensity field phenomena
- XUV Pulse generation
- Ultrafast incoherent X-ray generation
- High order harmonic generation

Additional applications were provided by the ultrashort pulse generation of Terahertz Electromagnetic Pulse Generation for Millimeter-Wave Spectroscopy

Terahertz radiation allows:

- differentiation between various materials, chemical compositions, or environments
- determination of fat Content, water content in vegetation, and internal content of containers.
- biomedical imaging of tissue
- chemical-reaction analysis, environmental and pollution control, materials inspection, fault Detection
- profiling of doping and defects in semiconductors, and packaging inspection

Additional biomedical applications include:

Optical coherence tomography

Optical coherence tomography (OCT) is an optical imaging technique that uses low coherence interferometry to obtain micron scale, cross-sectional images of biological systems. OCT has been used to provide topographic images of the transparent structures in the eye. Clinical studies have shown that OCT provides high resolution, cross-sectional images of the retina and can be used to diagnose a wide range of retinal macular diseases. OCT imaging in other human tissues is more difficult due to optical scattering. However, recent *in vivo* studies have shown that OCT can image architectural morphology in highly optically scattering tissues. Performing optical biopsy with OCT requires powerful sources with broad frequency bandwidth. Solid state lasers based on Ti:Al₂O₃ and Cr:Mg₂SiO₄ and rare-earth doped fiber lasers are capable of providing hundreds of milliwatts of single-transverse mode light with coherence lengths as short as a few microns.

Cornea Surgery

Corneal Photo-disruption with ultrashort pulse lasers utilizes laser-induced optical breakdown (LIOB) which take place with the pulse energy density reaches a plasma formation threshold. The reduce thermal and mechanical collateral effects associated with ultrashort pulse interactions offer superior performance for cornea reshaping as well as for intrastromal surgery.

Related topics include:

- Laser-induced breakdown in the eye at pulse durations from 100 ns to 100 fs
- Retinal damage mechanisms from ultrashort laser exposure
- Refractive surgical applications with ultrashort pulsed lasers,

Dental Hard Tissue Removal

While several systems are currently being considered for the purpose of processing of hard dental tissue, undesired thermal collateral damage and the lack of speed and efficiency are major obstacles. Picosecond and femtosecond pulse duration have shown themselves able to produce very precise cavities with only negligible thermal or shock wave collateral damage. Surface quality and morphological characteristics also appear to be superior to those of other laser systems. If a proper deliver system can be identified and developed and if the cost of ultrashort pulse laser system will continue to drop, such devices may become valid alternative to existing technology.

Additional topics include

- Microsurgical Effect of laser irradiation on the functional activity of enzymes with different structural complexity
- Influence of ultrashort-pulse laser on gandioblockade compounds,
- Feedback system for precision ultrashort pulse biotissue ablation
- Light transmission imaging in tissue-like phantom
- Real-time 2-photon confocal microscopy

AREAS OF ACTIVE RESEARCH LEADING TO ENABLING ULTRA SHORT PULSE LASER TECHNOLOGY INCLUDE:

- Ultrashort Pulse Lasers: Instrumentation and Measurements
- Compact ultrafast sources for biomedical applications
- Ultrashort laser pulse propagation through hollow core fibers
- Review of ultrashort pulse measurement: changing the basic ultrashort pulse
- Feedback system for precision ultrashort pulse biotissue ablation
- Modeling of Ultrashort Pulse Interaction with Matter
- Ultrashort Pulse Propagation in Transparent media
- Radially varying dispersion in high-numerical-aperture focusing
- Pressure and temperature evolution induced by ultra-short laser pulse ablation.

Radially varying dispersion in high-numerical-aperture focusing

M. Müller^a, G.J. Brakenhoff^a, U. Simon^b and J. Squier^c.

^aBioCentrum Amsterdam

Department of Molecular Cytology, University of Amsterdam.
Kruislaan 316, 1098 SM Amsterdam, The Netherlands.

^bCarl Zeiss Jena GmbH, Zeiss Group
D-07740 Jena, Germany.

^cElectrical and computer engineering department
University of California San Diego,
La Jolla, CA 92093-0339, USA.

ABSTRACT

Over the last few years a number of microscopical techniques have been developed that take advantage of ultrashort optical pulses. All these techniques rely on temporal pulse integrity at the focal point of a high-numerical aperture (NA) focusing system. We have investigated the dispersion induced broadening for pulses on the optical axis, using the two-photon absorption autocorrelation (TPAA) technique. We demonstrate that the induced broadening can be pre-compensated for by a properly designed dispersion pre-compensation unit for pulses as short as 15 femtoseconds.

Another source of pulse broadening in high-NA focusing systems is due to radial variations in the dispersion over the pupil of the objective. This may cause differences in the group delay between on-axis and outer ray wave packets, as well as differences in the broadening of the wave packets themselves. In this paper we present experimental results on the measurement of these radial variations in the dispersion characteristics over the aperture of high-NA microscope objectives, using a slightly modified TPAA technique.

Keywords: dispersion, group delay, multi-photon microscopy

1. INTRODUCTION

The advances in recent years in ultrashort laser pulse technology - notably all-solid state tunable lasers which routinely produce sub-100 fs optical pulses - has opened the way to the application of non-linear optical techniques in new fields, such as high resolution multi-photon microscopy [Denk, et al., 1990; Webb, 1990; Piston & Webb, 1991; Hell, et al., 1996; Szmacinski, et al., 1996]. Since the fluorescence intensity in two- and three-photon absorption depends non-linearly on the excitation intensity, maximum efficiency is attained when both the spatial focusing conditions are diffraction limited and the optical pulses have a minimum pulse duration at focus. This is especially important for microscopy of biological objects where the radiation load on the specimen is to be kept at a minimum to prevent biological damage, while at the same time extracting the maximum of information in terms of high signal-to-noise microscopic images.

The application of femtosecond pulses - which inherently have a substantial bandwidth - to microscopy leads to a new regime of imaging where the effects of (temporal) dispersion should be taken into account. In general this dispersion will cause broadening and even distortion of the optical pulses, leading in turn to a reduced efficiency in multi-photon absorption. Especially since the microscope objectives consist of a large number of, highly dispersive, glass elements, the effects of dispersion are generally non-negligible. Previously we investigated the influence of on-axis dispersion on the optical pulse duration at the focal point of high-numerical aperture (NA) microscope objectives and we developed methods to measure and pre-compensate the induced dispersion [Brakenhoff, et al., 1995; Müller, et al., 1995; Müller, et al., 1997]. In this paper we extend the analysis of dispersion induced by high-NA microscope objectives to include dispersion which is a function of the normalised radius with respect to the entrance pupil of the objective.

2. DISPERSION IN HIGH-NA OBJECTIVES

Dispersion of femtosecond optical pulses is the result of the functional dependence of the refractive index on the wavelength. This results in a frequency dependent phase shift experienced by the optical pulse. To separate out the various contributions to the total dispersion we expand the phase $\varphi(\omega)$ in a Taylor series:

$$\begin{aligned}\varphi(\omega) &= \varphi(\omega_0) + \left(\frac{d\varphi}{d\omega}\right)_{\omega_0} (\omega - \omega_0) + \frac{1}{2!} \left(\frac{d^2\varphi}{d\omega^2}\right)_{\omega_0} (\omega - \omega_0)^2 + \dots \\ &= \varphi_0 + \varphi_1 + \varphi_2 + \dots\end{aligned}\tag{1}$$

Here ω_0 denotes the centre frequency of the pulse. φ_0 is merely a phase offset and φ_1 is the group delay (GD) experienced by the pulse. The higher order terms - φ_2 : group delay dispersion (GDD), φ_3 : third-order dispersion (TOD), etc. - lead to a broadening of the pulse and to a distortion of the pulse shape. The total amount of dispersion induced on a pulse propagating through a material depends both on the material properties (through $n(\omega)$), the pathlength and the frequency bandwidth of the pulse.

In the case of dispersion induced by high-NA microscope objectives we should discriminate between two possible sources of dispersion. The first is the ordinary dispersion resulting from the propagation of the pulse through the various glass elements in the objective. We will refer to this as the *on-axis dispersion*. The second source for possible temporal broadening and distortion of the pulse at the focal point is dispersion which is a function of the relative position of the line of propagation with respect to the objective's entrance pupil. In other words, differences in dispersion between rays propagating through the centre of the lens or through the outer parts. We will refer to this as *radially varying dispersion*. Clearly for the *on-axis dispersion* only the second and higher order dispersion terms are important since they will cause a general broadening and distortion of the pulse. For the *radially varying dispersion* however, we also need to consider differences in the GD experienced between on-axis and off-axis rays (i.e. $GD(r)$), as well as radially varying higher orders of dispersion $GDD(r)$, $TOD(r)$, etc..

3. MEASURING THE DISPERSION AT THE FOCAL POINT OF A HIGH-NA LENS

In the measurement of the dispersion induced by high-NA microscope objectives we discriminate between: *on-axis dispersion* and *radially varying dispersion*. Two techniques have been developed to measure each of these separately.

3.1 Two-photon absorption autocorrelation (TPAA)

Since the TPAA technique has been discussed in detail elsewhere [Brakenhoff, et al., 1995; Müller, et al., 1995; Müller, et al., 1997], we summarise the main characteristics here. The general scheme of the measurement is depicted in figure 1. The laser beam first passes a dispersion pre-compensation unit, based on the double prism pair compensation configuration, permitting the addition of a variable amount of dispersion - from positive to negative - to the pulses. The pulses are then split in two parts, one passing a variable delay line before being recombined with the other part. The recombined parts then propagate collinearly either to a conventional second harmonic generation (SHG) set-up for a reference pulse duration measurement, or are focused by the objective under investigation in a dye solution (10^{-3} M Rhodamine 6G in water) to generate two-photon absorption (TPA). The fluorescence

is detected in the backscattering direction. The autocorrelation signal consists of the measurement of either the SHG signal or the TPA fluorescence signal as a function of the time delay, induced by the variable pathlength in the variable delay, between the pulses.

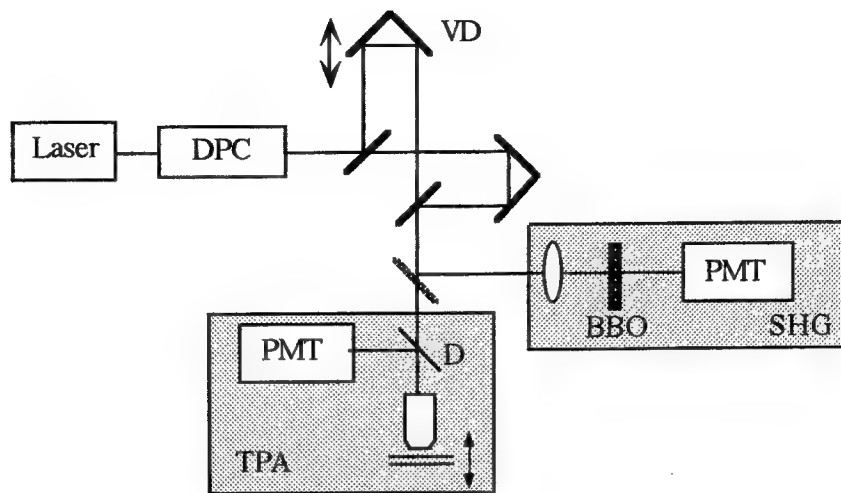


Figure 1. General schematic of the TPAA set-up. Symbols used: DPC: dispersion pre-compensation unit; VD: variable delay; D: dichroic mirror; BBO: type I BBO doubling crystal; PMT: photo multiplier tube.

The procedure for the TPAA measurements is then as follows. First, the system is optimised to produce the minimal pulse width in the SHG autocorrelation. For the laser system used in these experiments this resulted in near transform limited ($\Delta\nu\Delta t \sim 37$, assuming a Sech² input pulse) pulses of 15.5 fs. This provides the “zero-setting” of the dispersion pre-compensation unit. Next, the beam is directed through the microscope objective to be investigated. Again the dispersion pre-compensation unit is optimised to provide the minimal pulse duration in the TPA autocorrelation. Note that this corresponds to a maximum in the TPA fluorescence. From the adjustment required in the dispersion pre-compensation unit the induced dispersion by the objective can be calculated.

A typical result of the TPAA signal obtained in this manner is shown in figure 2. The objective under study in this case was a Zeiss CP-APOCHROMAT 100x/1.25 oil. The configuration of the dispersion pre-compensation set-up corresponded to an induced dispersion of GDD = -579 fs², TOD = -209 fs³ and FOD = -156 fs⁴. A dispersive ray-tracing calculation of the same system - based on the optical data provided for this objective - gives: GDD = +579.4 fs², TOD = +129.9 fs³ and FOD = +24.3 fs⁴, demonstrating excellent agreement between the experimental results and the theoretical modeling. Note that we ensured that the entrance pupil of the microscope objective was significantly under-filled to eliminate any possible effects from radially varying dispersion.

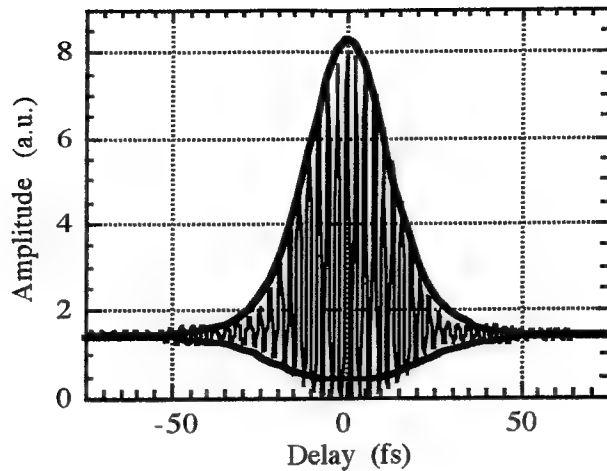


Figure 2. TPAA signal for a dispersion pre-compensation setting (579 fs^2) giving minimal pulse width for the Zeiss CP-APOCHROMAT 100x/1,25 oil microscope objective. The best fit was obtained assuming a Sech^2 input pulse.

Similar measurements have been done for a number of microscope objectives, the results of which are summarised in table I. These results clearly show that it is possible, using a properly designed dispersion pre-compensation unit, to focus 15 fs optical pulses with high-NA microscope objectives. It is important to note that the slight increase in pulse width for the higher GDD pre-compensation values results from residual third-order dispersion from the pre-compensation unit. This shows that it is possible - using a specially designed dispersion pre-compensation set-up - to obtain the original pulse width at the focal point of any of these microscope objectives.

Table I

Objective	Pulse width (fs)	GDD (fs^2)
SHG	15.5	0
Zeiss C-APOCHROMAT 63x/1,2W Korr	18.4	-1140
Zeiss C-APOCHROMAT 40x/1,2W Korr	18.4	-1104
Zeiss Plan Neofluar 100x/1,3 oil	14.7	-778
Zeiss Plan Neofluar 63x/1,25 oil	16.4	-887
Zeiss Plan Neofluar 40x/1,3 oil	17.5	-1104
Zeiss CP-Achromat 100x/1,3 oil	15.9	-579

Table I. The minimum pulse width obtained in the TPAA measurements for a series of microscope objectives and the dispersion pre-compensation value required to obtain this pulse width.

3.2 Two-photon absorption cross-correlation (TPAC)

Since the pathlengths through the various glass elements in a microscopic objective are different for the chief and marginal rays, we need to consider dispersion variations as a function of the radial position with respect to the entrance pupil. To be able to measure this, the general TPAA set-up is modified to cross-correlate the outer rays with the central rays. Figure 3 shows a schematic of the modifications.

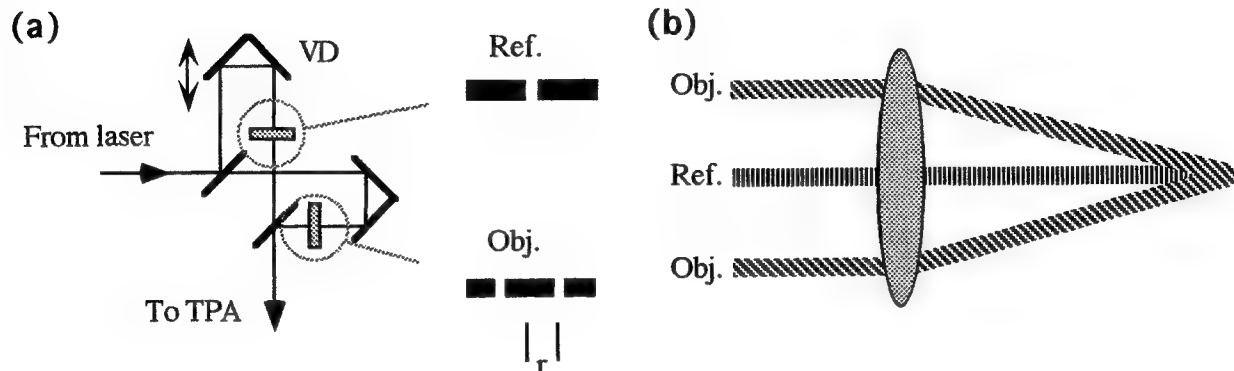


Figure 3. Schematic of the modifications to the TPAA set-up (figure 1) to enable TPAC. (a) In the “reference” arm of the autocorrelator an iris is placed passing only the centre of the beam. In the “object” arm of the autocorrelator an annulus of variable radius (r) is placed. (b) When focused in a non-linear medium a TPA cross-correlation signal is produced as a function of the relative delay between object and reference pulse.

In one of the beams in the autocorrelator - to be denoted by “reference” beam - an iris is positioned, passing only the centre of the beam. In the other beam - denoted by “object” - an annulus of variable radius is positioned. The TPA signal will thus consist of a cross-correlation between the central rays and the rays passed by the annulus. The relative time position of the maximum of this cross correlation signal determines the relative delay between the reference and object rays. The delay equals zero value is taken for the (auto) cross-correlation with two irises in both arms. The principle of the TPAC measurement is to measure the relative delay value for the maximum of the cross-correlation signal as a function of the radius of the annulus in the object beam.

A typical result of such a measurement is shown in figure 4 for the Zeiss CP-Achromat 100x/1,3 oil microscope objective. The central rays are delayed more than the outer rays. In case of the 15 fs pulses used in these experiments this effectively means that there is no interaction between pulses propagating through the centre of the lens and pulses propagating through the outer part. Clearly this temporal effect is coupled to the spatial domain and consequently may affect the point spread function of the system.

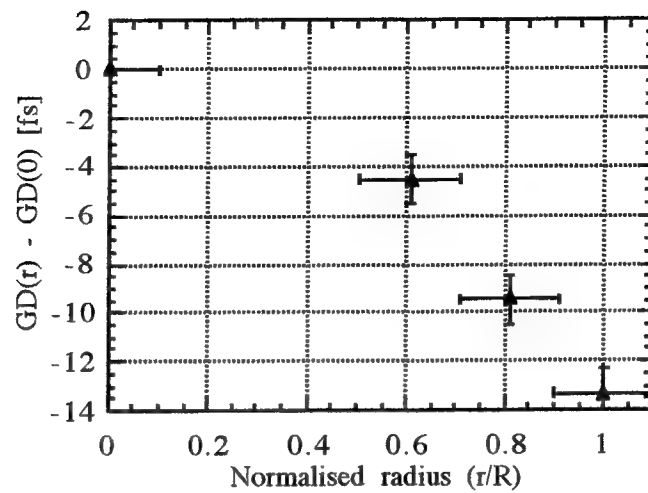


Figure 4. TPAC signal for the Zeiss CP-Apochromat 100x/1,25 oil microscope objective, showing an increasing group delay as a function of normalised radius.

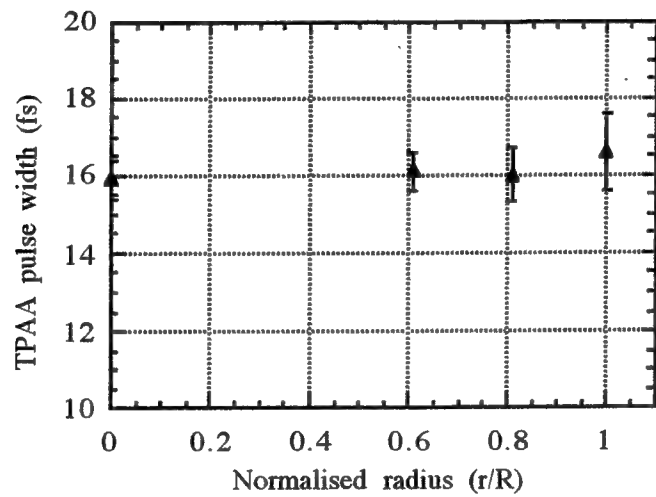


Figure 5. TPAA signal as a function of normalised radius at a dispersion pre-compensation setting giving the minimal pulse width at $r/R=0$ for the Zeiss CP-Apochromat 100x/1,25 oil microscope objective. The best fit was obtained assuming a Sech^2 input pulse.

The methods of TPAA and TPAC can be combined to measure the pulse broadening as a function of radius. In this case, equal annuli are placed in both arms of the autocorrelator and the TPAA signal is measured in a similar manner as in section 3.1. As is shown in figure 5 there is negligible pulse broadening for this objective as a function of radius.

4. CONCLUSION.

Significant amounts of dispersion are induced by microscope objectives on femtosecond optical pulses. There are two contributions to this dispersion: (i) an on-axis contribution; and (ii) a radially varying contribution. The *on-axis dispersion* causes a substantial broadening of the optical pulse, which can however be compensated for by a properly designed dispersion pre-compensation unit. It has been shown that it is possible to pre-compensate the dispersion for pulses as short as 15 femtoseconds. The *radially varying dispersion* is primarily due to a radially varying group delay. This causes wave packets propagating through the centre of the lens to experience a larger delay than wave packets propagating through the outer part of the objective. This effect, which is independent of the pulse duration itself, becomes relatively more important for pulses of decreasing pulse duration. The effect of a radially varying group delay may potentially reduce the numerical aperture of the system and consequently degrade the resolution in microscopic applications. Experiments are under way to determine how the resolution is affected. We have shown that the pulse broadening itself - due to GDD - is approximately constant over the radius of the pupil of the objective.

ACKNOWLEDGMENT

This research was financially supported in part by the Stichting voor Fundamenteel Onderzoek der Materie (FOM), Utrecht, The Netherlands, under grant no. 94RG02.

REFERENCES

Brakenhoff, G.J., Müller, M. & Squier, J. (1995) Femtosecond pulse width control in microscopy by Two-photon Absorption autocorrelation. *J. Microsc.* **179**(3), 253-260.

Denk, W., Strickler, J.H. & Webb, W.W. (1990) Two-photon laser scanning fluorescence microscopy. *Science* **248**, 73-76.

Hell, S.W., Bahlmann, K., Schrader, M., Soini, A., Malak, H., Gryczynski, I. & Lakowicz, J.R. (1996) Three-photon excitation in fluorescence microscopy. *J. Biomed. Opt.* **1**(1), 71-74.

Müller, M., Squier, J. & Brakenhoff, G.J. (1995) Measurement of femtosecond pulses in the focal point of a high-numerical-aperture lens by two-photon absorption. *Opt. Lett.* **20**(9), 1038-1040.

Müller, M., Squier, J., Wolleschensky, R., Simon, U. & Brakenhoff, G.J. (1997) Dispersion pre-compensation of 15 femtosecond optical pulses for high-numerical-aperture objectives. Accepted for publication: *J. Microsc.*.

Piston, D.W. & Webb, W.W. (1991) Three dimensional imaging of intracellular calcium activity using two-photon excitation of fluorescent indicator dye Indo-1. *Biophys. J.* **59**, 156.

Szmacinski, H., Gryczynski, I. & Lakowicz, J.R. (1996) Three-photon induced fluorescence of the Calcium probe Indo-1. *Biophys. J.* **70**, 547-555.

Webb, W.W. (1990) Two photon excitation in laser scanning fluorescence microscopy. Conference: *MICRO 90* (London).

SESSION 2

Ultrashort-Pulse Lasers: Instrumentation and Measurements

Measurement and modeling of the focusing of 15 femtosecond optical pulses with a high-numerical-aperture objective

J. Squier^a, V. V. Yakovlev^a, M. Müller^b, A. Buist^b, G.J. Brakenhoff^b,
^cU. Simon

^a University of California, San Diego, 9500 Gilman dr., La Jolla, Ca, 92093, U.S.A

^bUniversity of Amsterdam, Kruislaan 316, 1098 SM Amsterdam, The Netherlands.

^cCarl Zeiss Jena GmbH, Zeiss Group, D-07740 Jena, Germany.

ABSTRACT

Pulse broadening of ultrashort optical pulses, as short as 15 femtoseconds (fs), due to the propagation through high-numerical-aperture (NA) microscope objectives can be pre-compensated to ensure temporal pulse integrity at the focal point. The predictions from dispersive ray-tracing calculations show excellent agreement with the experimental results from two-photon absorption autocorrelation (TPAA) for the Zeiss CP-Achromat 100x/1,25 oil microscope objective. From this, general predictions can be inferred for dispersion in most types of microscope objectives. Key element to the work is a carefully designed dispersion pre-compensation configuration, which minimizes pulse broadening due to residual third order dispersion. The capability to focus these ultrashort pulses with control of the pulse definition at the focal point is important for two-photon absorption (TPA) and time-resolved microscopy.

Keywords: High numerical aperture objectives, ultrashort pulses, dispersive ray-tracing, two-photon absorption autocorrelation

1. Measurement and modeling the propagation of ultrashort pulses in a high NA system

Laser systems which routinely produce sub-100 fs optical pulses have recently become widely available. These systems have inspired the application of ultrashort optical pulses in various areas of microscopy, including two-photon absorption (TPA) microscopy (e.g.: [1, 2]), multi-photon absorption imaging (e.g. [3, 4]), fluorescence lifetime imaging ([5, 6]) and optical coherence tomography (e.g. [7, 8]). For effective application, all these techniques rely on proper focusing of femtosecond optical pulses with a high numerical aperture (NA) microscope objective. Because these objectives consist of multiple lens elements, they induce substantial dispersion to - inherently broad band - femtosecond pulses. Proper understanding of this induced dispersion facilitates the application of dispersion pre-compensation techniques to ensure optimal temporal - and spatial - focusing of the femtosecond pulses.

In earlier work [9-12] the general characteristics of focusing > 50 fs pulses has been investigated. It has been found that for these pulses the induced broadening is primarily caused by group delay dispersion. The effect of phase time delay was found non-negligible only for lenses with substantial chromatic aberration over the band width of the pulse [13]. In this paper we investigate in detail the induced dispersion when focusing 15 fs optical pulses with a Zeiss CP-Achromat 100x/1,25 oil microscope objective.

The induced dispersion by the NA objective is measured using the TPAA technique, which has been described in detail elsewhere [9]. Figure 1 shows a schematic of the experimental set-up. The output from a home-built Ti:Sapphire oscillator, operating at 800 nm, 80 MHz, passes a dispersion pre-compensation unit based on a double prism set-up. The dihedral reflector R₁ is mounted on a translation stage to permit varying from negative to positive induced dispersion. The fused silica prisms, with an apex angle of 69°, are used at 55°20' angle of incidence. The beam then passes a dispersion balanced Mach-Zehnder interferometric autocorrelation unit. Insertion of mirror M₁ directs the beam to an off-axis parabolic mirror which focuses it in a 100 μm, type I KDP crystal, producing a second harmonic generation (SHG) signal, which is detected through a BG39 filter with a photomultiplier tube (PMT). Alternatively, the mirror M₁ can be removed and the beam is focused by a high NA objective (Zeiss CP-Achromat 100x/1,25 oil) into a 10⁻³ M solution of Rhodamine 6G in water. The fluorescence generated in the induced TPA process is detected in the backscattering direction, reflected off a dichroic mirror, through a BG39 filter with a photomultiplier tube (PMT). The TPAA amplitude showed a quadratic dependence on the input pulse power, demonstrating that the absorption is indeed a two-photon process.

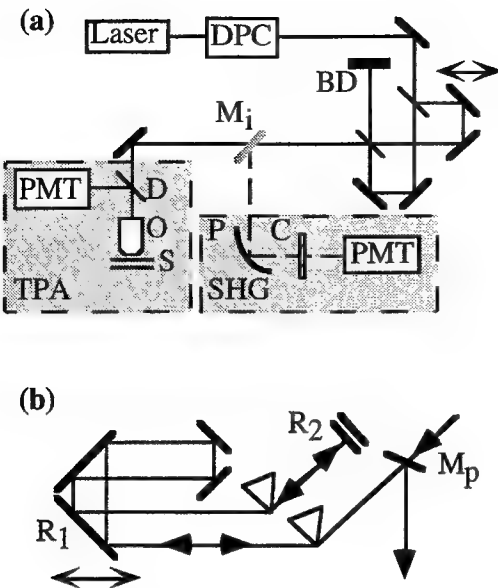


Figure 1.

Schematic of TPAA set-up. (a) DPC: dispersion pre-compensation unit; BD: beam dump; D: dichroic mirror; O: objective, S: sample; C: 100 μ m type I KDP crystal; PMT: photomultiplier tube. Insertion or removal of mirror M_1 permits switching between SHG and TPA autocorrelation respectively. (b) Detail of DPC. R_2 is a dihedral step-up mirror which retro reflects the beam at an elevated plane with respect to the incoming beam. The pick-off mirror M_p reflects the beam at this elevated plane out of the DPC.

prism pairs have been made from dispersive glasses such as SF10 in order to produce large amounts of dispersion with modest prism spacings. The difficulty with the more dispersive glasses, however, is that the rate of group delay dispersion (GDD) to third order dispersion (TOD) produced by the prism pair is a poor match to the material path length in the objective it is attempting to compensate. Thus, the residual TOD due to the prism compressor quickly becomes dominating, and it is this term that ultimately limits the compressed pulse width. Indeed, attempting to compress the pulse with SF10 prisms resulted in minimum compressed pulsewidths no better than 30 fs. For this reason, fused silica prisms are used. The prism compressor separation increases due to the lower dispersion of the fused silica, but the residual phase errors are smaller enabling the pulse to be recompressed to essentially its transform limit.

Using the optical data for the CP-Achromat 100x/1.25 oil microscope objective, the dispersion characteristics were theoretically modeled. The geometric optical pathlength propagated by a certain ray is calculated using straight forward ray-tracing. The dispersion of each element is then calculated using a Taylor expansion of the frequency dependent phase ($\varphi(\omega)$) [14]:

$$\varphi(\omega) = \varphi(\omega_0) + \left(\frac{d\varphi}{d\omega} \right)_{\omega_0} (\omega - \omega_0) + \frac{1}{2!} \left(\frac{d^2\varphi}{d\omega^2} \right)_{\omega_0} (\omega - \omega_0)^2 + \dots \quad (1)$$

By expressing the derivatives ($d^n\varphi/d\omega^n$) in terms of ($d^n n/d\lambda^n$), multiplied by the geometric pathlength through each lens element in the objective, the total dispersion of the microscope objective can be calculated to any desired order. The first two terms in equation (1) represent a phase shift and the group delay and do not alter the shape of the pulse. The higher order terms denoted by group delay dispersion (GDD), third order dispersion (TOD) and fourth order dispersion (FOD) respectively cause pulse broadening and distortion. A dispersive ray-tracing calculation for the on-axis ray of the objective gives a relative contribution of these terms of: GDD = 579.4 fs²; TOD = 129.9 fs³ and FOD = 24.3 fs⁴. Note that the factorial preceding each coefficient is already included in these dispersion numbers, and those reported throughout this paper.

Figure 2b shows the TPAA signal for the dispersion pre-compensation unit set to minimum pulse width. The best fit to data was obtained for a sech² input pulse, yielding an almost transform limited ($\Delta\omega\Delta t \sim 39$) pulse width of 15.9 (± 0.1) fs. Note that all, noise induced, errors in the pulse width measurements reported here are based on the change in pulsewidth measurement from acquisition to acquisition. Compared to the dispersion setting to obtain a minimum in the SHG autocorrelation signal of 15.5 (± 0.1) fs (figure 2a), an additional -579 fs² of dispersion was required to compensate for the dispersion induced by the objective. Figure 2c shows the dependence of the pulse width and TPAA amplitude as a function of induced dispersion pre-compensation. As expected, the TPA efficiency increases close to linearly with decreasing pulse width. The fact that the minimum TPAA pulse width almost equals the minimum pulse width obtained with SHG autocorrelation indicates the absence of sample induced broadening. This was further substantiated in independent experiments, where the KDP crystal was substituted for a solution of Rhodamine 6G, and the all reflective optic geometry was used.

The choice of prism material is critical for optimal compensation. Traditionally,

for optimal compensation. Traditionally,

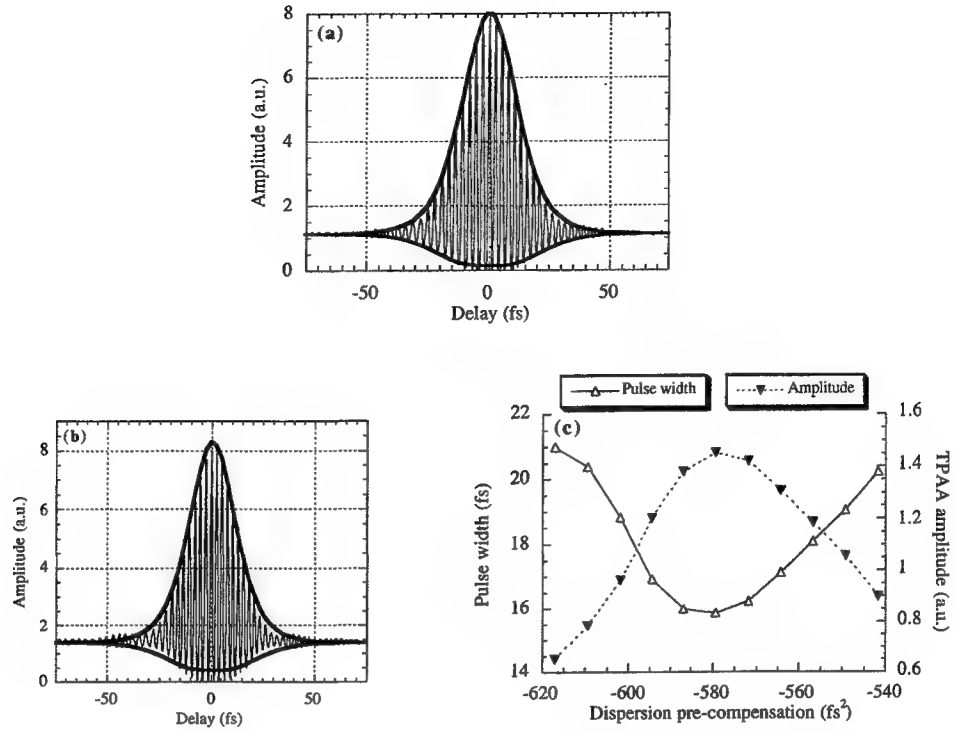


Figure 2.

(a) SHG interferometric autocorrelation signal. (b) TPAA signal for a dispersion pre-compensation setting (-579 fs^2) giving minimal pulse width for the CP-Achromat 100x/1.25 oil microscope objective. The best fit was obtained assuming a sech^2 input pulse. (c) TPAA pulse width and amplitude as function of induced dispersion pre-compensation.

Based on the same principles of dispersive ray-tracing, the induced dispersion at each setting of the dispersion pre-compensation unit (figure 2c) can be calculated. The setting for the minimum TPAA pulse width (figure 2b) for the prism compressor is calculated to correspond to $\text{GDD} = -579 \text{ fs}^2$, $\text{TOD} = -209 \text{ fs}^3$ and $\text{FOD} = -156 \text{ fs}^4$. This includes the dispersion of the coatings in the prism compressor. When the net dispersion of the system is used (prism compressor dispersion plus objective dispersion) it is calculated that a $15.5 \text{ fs} \text{ sech}^2$ pulse should only broaden by $\sim 0.8 \text{ fs}$, which is in excellent agreement with the measured pulse broadening.

At these pulse durations, optical coatings can also produce significant effects. All turning optics in this experiment were silvered mirrors (Denton Vacuum, Inc., coating FSS-99), with the exception of the dihedral mirror R_2 used to change the beam height in the prism compressor. This is a CVI, TLM1 coating for s-polarization, 45 degree angle-of incidence. The effect of this coating was investigated by taking multiple reflections off the mirror, and measuring the induced pulse broadening as a function of number of mirror bounces. A $19.7 (\pm 0.1) \text{ fs}$ pulse was found to broaden to $22.3 (\pm 0.1) \text{ fs}$ after 40 reflections off this coating. This is the expected pulse broadening given the calculated dispersion values for this coating found in the CVI catalog [15]. Thus, for our application, this is an excellent coating when using sub-20 fs pulses.

In these experiments, the beam diameter ($\text{FWHM} \approx 5 \text{ mm}$) just fills the pupil of the objective (4.1 mm). The drop in intensity of the beam near the pupil edges, substantially reduces the contribution of any radially varying dispersion terms, such as group delay, to the TPAA signal. The combination of a radially varying group delay, and the fact that the autocorrelation is measured under high NA conditions leads to a slight decrease in the normally expected 8:1 contrast of the interferometric autocorrelation trace.

In conclusion, we have shown that with proper dispersion compensation it is possible to produce 15-fs pulses at the focus of a high numerical aperture objective. The entire system, prism dispersion compensator plus objective, has been modeled using a straight forward dispersive ray-tracing analysis. Model and experiment are in excellent agreement. We have shown that by the appropriate choice of prism material the pulse width can be optimized, below the 20-30 fs pulse width

limit shown for other materials such as SF10 glass [12]. Further, with proper accounting of all higher order dispersion, including the quartic phase, it is reasonable to expect that systems can be designed for even shorter pulse durations. A radially varying group delay will also play a more significant role as the pulse duration is decreased. This must be accounted for, by some type of radially varying correction, or the effective numerical aperture over which the pulse duration is essentially constant will be reduced.

2. Acknowledgements

This research was financially supported in part by the Stichting voor Fundamenteel Onderzoek der Materie, Utrecht, The Netherlands, under grant no. 94RG02. The experimental portion of this work was performed at the University of California, San Diego.

3. References

1. W. Denk, J. H. Strickler and W. W. Webb, "Two-photon laser scanning fluorescence microscopy," *Science* **248**, 73 (1990).
2. D. W. Piston and W. W. Webb, "Three dimensional imaging of intracellular calcium activity using two-photon excitation of fluorescent indicator dye Indo-1," *Biophys. J.* **59**, 156 (1991).
3. S. W. Hell, K. Bahlmann, M. Schrader, A. Soini, H. Malak, I. Gryczynski and J. R. Lakowicz, "Three-photon excitation in fluorescence microscopy," *J. Biomed. Opt.* **1**(1), 71 (1996).
4. H. Szmacinski, I. Gryczynski and J. R. Lakowicz, "Three-photon induced fluorescence of the Calcium probe Indo-1," *Biophys. J.* **70**, 547 (1996).
5. M. Müller, R. Ghauharali, K. Visscher and G. Brakenhoff, "Double-pulse fluorescence lifetime imaging in confocal microscopy," *J. Microsc.* **177**(2), 171 (1995).
6. A. H. Buist, M. Müller, E. J. Gijsbers, G. J. Brakenhoff, T. S. Sosnowski, T. B. Norris and J. Squier, "Double pulse fluorescence lifetime measurements", *J. Microsc.* **186**(3), 212-220.
7. J. G. Fujimoto, S. D. Silvestri, E. P. Ippen, C. A. Puliafito, R. Margolis and A. Oseroff, "Femtosecond optical ranging in biological systems," *Opt. Lett.* **11**(3), 150 (1986).
8. D. Huang, E. A. Swanson, C. P. Lin, J. S. Schuman, W. G. Stinson, W. Chang, M. R. Hee, T. Flotte, K. Gregory, C. A. Puliafito and J. G. Fujimoto, "Optical coherence tomography," *Science* **254**, 1178 (1991).
9. M. Müller, J. Squier and G. J. Brakenhoff, "Measurement of femtosecond pulses in the focal point of a high-numerical-aperture lens by two-photon absorption," *Opt. Lett.* **20**(9), 1038 (1995).
10. P. E. Hänninen and S. W. Hell, "Femtosecond pulse broadening in the focal region of a two-photon fluorescence microscope," *Bioimaging* **2**, 117 (1994).
11. G. J. Brakenhoff, M. Müller and J. Squier, "Femtosecond pulse width control in microscopy by Two-photon Absorption autocorrelation," *J. Microsc.* **179**(3), 253 (1995).
12. J. B. Guild, C. Xu and W. W. Webb, "Measurement of group delay dispersion of high numerical aperture lenses using two-photon excited fluorescence," *Appl. Opt.* **36**(1), 397 (1997).
13. C. Radzewicz, M. J. I. Grone and J. S. Krasinski, *Opt. Commun.* **126**, 185 (1996).
14. J.-C. Diels and W. Rudolph, in *Ultrashort laser pulse phenomena*. P. F. Liao, P. L. Kelley, I. Kaminow, ed. (Academic Press, San Diego (CA), USA, 1996).
15. CVI Laser Cooperation, Optics and coatings catalogue , (1996).

Review of Ultrashort Pulse Measurement: Changing the Basic Ultrashort Pulse Experiment

David N. Fittinghoff

University of California, San Diego, Dept. of Chemistry, La Jolla, CA 92093-0339

ABSTRACT

Until recently, experiments in ultrashort pulse science have involved measuring the spectrum and autocorrelation of the input pulse(s) and only measuring the integrated energy or perhaps time-resolved energy of the output signal. These experiments ignored the information contained in the input and output pulse phases and intensity profiles. New pulse measurement techniques such as frequency-resolved optical gating (FROG), when combined with older techniques such as spectral interferometry, now allow the complete characterization of the pulses. These techniques allow measurements of the intensity, phase, and polarization state of ultrashort pulses as functions of time (or frequency) and space. These techniques work for wavelengths from the UV to the IR and for extremely weak pulses and very high power pulses. They also allow entirely new classes of experiments for measuring ultrafast phenomena. Now the phases and temporal profiles of the input pulses may be measured and controlled, and the intensity and phase of the output pulses can also be measured. These new measurement techniques have thus greatly increased the obtainable information in ultrafast experiments. This paper reviews current pulse measurement methods including frequency-resolved optical gating and spectral interferometry and describes how they are changing the way that ultrashort pulse experiments are performed.

Keywords: frequency-resolved optical gating, spectral interferometry, autocorrelation, ultrashort pulses, ultrafast science

1. INTRODUCTION

From their first use,^{1,2} autocorrelators were the main device used for measuring the temporal characteristics of short laser pulses. When combined with a measured spectrum, the autocorrelation gave an estimate of the pulse length, and of how close the width of the pulse was to the spectral limit (the limit set by the Fourier transform of the spectrum assuming a constant phase). As these were the best measurements available, the generic experiment in ultrashort pulse science involved measuring the spectrum and autocorrelation of the input pulse(s) and the integrated energy or perhaps time-resolved energy of the output signal. Figure 1 shows a schematic of this type of experiment. The main difficulty with this generic experiment is that it ignores most of the information contained in the input and output pulses. If we ignore the spatial behavior of the pulse and assume that it is linearly polarized, a pulse is defined by its electric field as a function of time, $E(t)$, where

$$E(t) = \text{Re} \left\{ \sqrt{I(t)} \exp(i\omega_0 t - i\phi(t)) \right\}. \quad (1)$$

Here $I(t)$ and $\phi(t)$ are the time-dependent intensity and phase of the pulse, and ω_0 is a carrier frequency. The intensity contains information about the relative amounts of energy contained in the pulse at given times, while the time-dependent phase contains the frequency versus time information. The instantaneous frequency of the pulse, $\omega(t)$, is

Further Author information
Email: dnf@chem.ucsd.edu; Telephone: 619-534-0290 ext. 46; Fax: 619-534-7654

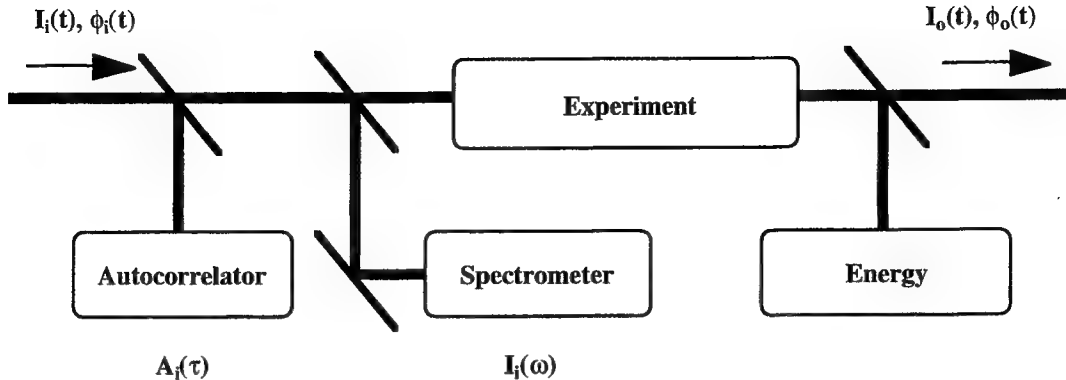


Figure 1 Schematic of the old generic experiment in ultrafast science. The input pulse has intensity $I_i(t)$ and phase $\phi_i(t)$, and the output pulse has intensity $I_o(t)$ and phase $\phi_o(t)$. The only characteristics of the input pulse that are measured are the autocorrelation and spectrum, and only the energy (or time resolved energy) is measured for the output pulse. The input pulse and the output pulse are *not* completely characterized.

$$\omega(t) = \omega_0 - \frac{d\phi}{dt}. \quad (2)$$

The pulse may also be described in the frequency domain as $E(\omega)$, the Fourier transform of $E(t)$. Ignoring the negative-frequency term of the Fourier transform gives

$$E(\omega) = \text{Re} \left\{ \sqrt{I(\omega - \omega_0)} \exp(i\phi(\omega - \omega_0)) \right\}. \quad (3)$$

Here $I(\omega - \omega_0)$ is the spectrum, and $\phi(\omega - \omega_0)$ is the spectral phase. While the spectrum is directly measurable, an autocorrelation gives little information about the spectral phase, so measuring the autocorrelation and spectrum allows for a large uncertainty in the behavior of the pulses that are being measured.

New pulse measurement techniques, however, such as frequency-resolved optical gating (FROG) combined with older techniques such as spectral interferometry, now allow the complete characterization of the intensity and phase of ultrashort pulses. These techniques work for wavelengths from the UV to the IR and for extremely weak pulses and very high power pulses. They also allow entirely new classes of experiments for measuring ultrafast phenomena. Now the phases and temporal profiles of the input may be measured and controlled, and the intensity and phase of the output pulses can also be measured. These new measurement techniques have thus greatly increased the information that can be obtained in ultrafast experiments. This paper reviews current pulse measurement methods including frequency-resolved optical gating and spectral interferometry and describe how they are changing the way that ultrashort pulse experiments are performed.

2. AUTOCORRELATIONS AND SPECTRA

2.1. Autocorrelations

When measuring the duration of an event, the method normally used is to compare it to a faster event. We measure years by the passing of seasons or days. We measure days or hours by the passage of the sun, or the swing of a pendulum. As technology has advanced, we have compared fractions of seconds to vibrations of quartz crystals or other very rapid events. In measuring an ultrashort laser pulse, however, the problem is that the pulse is by far the fastest available signal in the laboratory. How, then, do we measure a pulse when we don't have anything faster than it for a reference? The autocorrelation was one of the first real attempts to answer this question. The key to the technique is to allow the pulse to measure itself. Specifically, autocorrelation involves splitting the pulse into two replica pulses, introducing a time delay between the replicas and spatially overlapping them in an instantaneously responding nonlinear medium. The autocorrelation is then the signal produced by the nonlinear interaction of the two replicas in the medium as a function of the time delay.

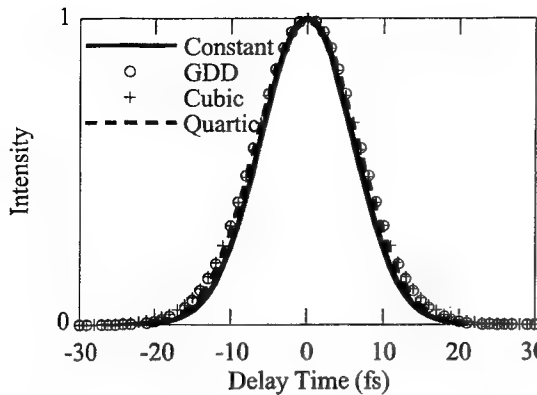


Figure 2 SHG autocorrelations for a spectrally limited 10 fs Gaussian pulse (constant phase), and the same pulse after adding 17.5 fs²/radian of GDD, 250 fs³/radian² of cubic phase, and 1400 fs⁴/radian³ of quartic phase. The full width at half maxima of the autocorrelations are 14.1 fs, 15.7 fs, and 15.3 fs, respectively. Since the non-spectrally limited pulses have approximately 11 fs full width at half maxima, the error in estimating the pulsewidth based on the spectrally limited pulseshape is small. Note, however, that the different phase distortions produce essentially identical shapes of the SHG autocorrelation.

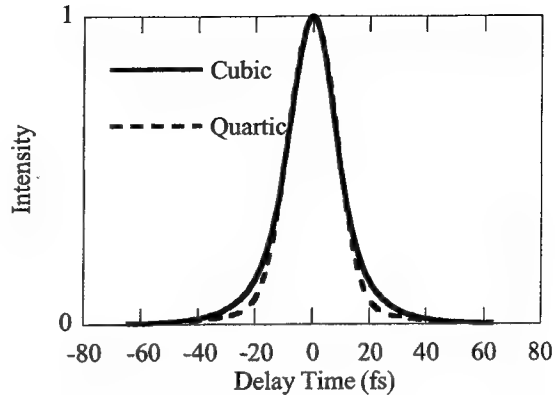


Figure 3 The SHG autocorrelations of an initially 10-fs spectrally limited Gaussian after adding 850 fs³/radian² and 7000 fs⁴/radian³ quartic phase. Both of these pulses have 14.3 fs intensity FWHM, and the autocorrelations are virtually identical except for small differences in the size of the wings of the autocorrelations. These autocorrelations are nearly identical for most experimental purposes, and provide essentially no information about the order of the phase.

The most common nonlinear interaction used for autocorrelation is second-harmonic generation (SHG). The signal produced by an SHG autocorrelator occurs at twice the center frequency of the input pulse and has a form given by

$$A(\tau) = \int_{-\infty}^{\infty} I(t)I(t-\tau)dt. \quad (4)$$

Here τ is the time delay between the pulses. Looking at Equation 4, we see that the signal is essentially obtained by using one of the replica pulses—here $I(t-\tau)$ —to gate out part of the other pulse. Thus the autocorrelation uses the pulse to measure itself. Unfortunately, this measurement yields a smeared out version of $I(t)$ that often masks complicated pulse structure. Satellite pulses, for instance, often look exactly the same as a long smooth tail on the pulse. Worse, while an estimate of the pulsewidth may be made by assuming a specific pulseshape, the estimate obtained is highly dependent on the assumed shape. This makes predictions based on SHG autocorrelation unreliable. There are a number of different autocorrelation methods based on other nonlinearities or specific interferometric.³⁻⁸ None of these autocorrelations eliminate all of these problems.

For the moment, let us consider pulses with durations close to the spectral limit. By measuring the spectrum of the pulse and assuming a constant phase, the spectrally limited pulsewidth can be determined. Then direct calculation gives the autocorrelation of the spectrally limited pulse. If the measured autocorrelation of the actual pulse matches that of the spectrally limited pulse, then the pulse must be near the transform limit. Consider, for example, making an SHG autocorrelation of a spectrally limited 10 fs Gaussian. As shown in Figure 2, adding 17.5 fs²/radian of GDD, 250 fs³/radian² of cubic phase or 1400 fs⁴/radian³ of quartic phase produces an only marginally different autocorrelation. The autocorrelation full width at half maxima for these four cases are 14.1 fs, 15.7 fs, 15.5 fs, and 15.3 fs, respectively. Since the non-spectrally limited pulses have approximately 11 fs FWHM, the error in estimating the pulsewidth based on the spectrally limited pulse shape is small. Unfortunately differentiating between these different phases based on these autocorrelations is impossible. This is not true just for pulses that are close to the spectral limit. Figure 3 shows the autocorrelations of an initially 10-fs spectrally

limited Gaussian after adding 850 fs³/radian² of cubic phase or 7000 fs⁴/radian³ of quartic phase. Both of these pulses have 14.3 fs intensity FWHM. Again the autocorrelations are very similar except for small changes in the wings of the autocorrelations. For experimental purposes, these autocorrelations are nearly identical, and provide almost no information about the phase distortion that is present. Even the parity of the distortion cannot be determined. Other forms of autocorrelation are all relatively insensitive to the exact phase as well; although, some third-order autocorrelators are sensitive to the parity of the dominant phase term.

2.2. The Spectrum

As mentioned above, the spectrum is directly measurable, and entire books have been written on how to build optical spectrometers.⁹ Thus the measurement is generally a matter of buying the appropriate spectrometer. The spectrum is related to the field by

$$\tilde{I}(\omega) = \left| \int_{-\infty}^{\infty} E(t) \exp(-i\omega t) dt \right|^2. \quad (5)$$

The definition given in Equation 3 shows that, when combined with the appropriate spectral phase, the spectrum gives the Fourier transform of the electric field of the pulse. Without the phase, however, nothing is known about the temporal behavior of the pulse. Even though there have been attempts to deduce the phase from the spectrum and autocorrelation, taking the two measurements at the same time still does not remove all the uncertainties in the behavior of the pulse.^{10,11}

3. FREQUENCY-RESOLVED OPTICAL GATING

3.1. Introduction

The real goal for developing ultrashort pulse measurements has been full characterization of the intensity and phase of the pulse, and recently a burst of new techniques operating in the time-frequency domain have achieved full characterization.¹² Of these techniques, the most widely applied is frequency-resolved optical gating (FROG)¹³. FROG involves measuring a spectrogram of the pulse. Mathematically, the spectrogram of a pulse is given by

$$S(\omega, \tau) = \left| \int_{-\infty}^{\infty} E(t) g(t-\tau) \exp(-i\omega t) dt \right|^2. \quad (6)$$

Here $g(t-\tau)$ is a variable-delay gate function. The spectrogram then is the set of all parts of $E(t)$ that are gated out as τ is varied. To within an absolute phase factor, the spectrogram of the pulse determines $E(t)$ completely.

What, however, is the gate function in the laboratory? The gate pulse must be shorter than the pulse to be measured or spectral information, and hence phase information, will be lost. In the field of acoustics where the spectrogram has been used for decades, the sound pulses being measured are relatively long, and it is a trivial matter to produce electronic pulses can be used as a gate. For ultrafast pulses, however, the pulse to be measured is usually by far the fastest event in the laboratory. Thus, as in an autocorrelator, the pulse must be used to gate itself.

3.2. Combining the Autocorrelator and Spectrometer

Since the pulse must be used to gate itself, a nonlinear-optical process must be used as the gating interaction. Consider a SHG autocorrelator. The signal field produced by the autocorrelator is

$$E_{sig}^{SHG}(t, \tau) = E(t) E(t-\tau) \quad (7)$$

where as before t is time and τ is the time delay between the two pulses as they arrive at the second-harmonic material. If that signal field is then spectrally resolved in a spectrometer, the result is

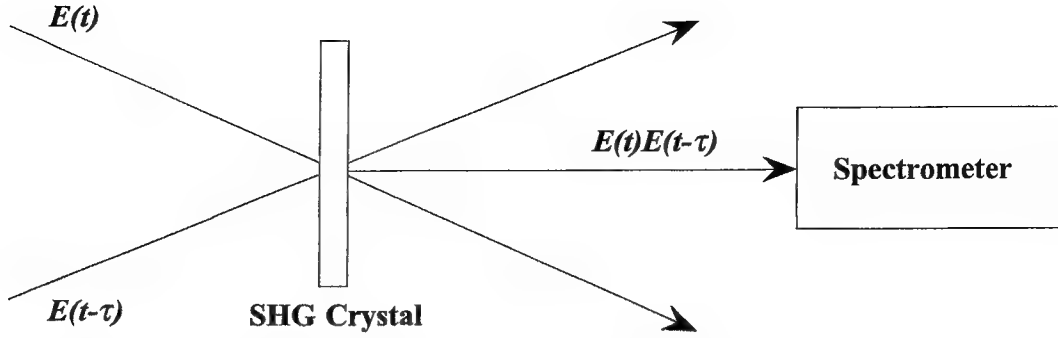


Figure 4 Schematic of an SHG FROG device. The SHG FROG is simply a second-harmonic generation autocorrelator followed by a spectrometer that spectrally resolves the autocorrelation signal as a function of the time delay, τ , between the input pulse

$$I_{FROG}^{SHG}(\omega, \tau) = \left| \int_{-\infty}^{\infty} E(t)E(t-\tau) \exp(-i\omega t) dt \right|^2. \quad (8)$$

This measurement, also called the SHG FROG trace,¹⁴⁻¹⁶ is a spectrogram with the gate pulse equal to the signal pulse. Experimentally, the old methods of characterization involved taking separate autocorrelations and spectra. FROG is not particularly more complicated because it simply involves moving the spectrometer after the autocorrelator and taking spectra of autocorrelations. Figure 4 shows a schematic of an SHG FROG. Note too that other FROG beam geometries are possible based on polarization gating (PG)¹⁵, self diffraction (SD), third-harmonic generation (THG)¹⁷, and many other near instantaneous nonlinear interactions.¹³ The variety of possible beam geometries makes FROG useful from the ultraviolet to the infrared and for multi-shot or single-shot experiments.¹³ While the forms of the signal field $E_{sig}(t, \tau)$ may be different from that given above for SHG, the FROG measurements are all given by

$$I_{FROG}(\omega, \tau) = \left| \int_{-\infty}^{\infty} E_{sig}(t, \tau) \exp(-i\omega t) dt \right|^2. \quad (9)$$

3.3. Phase Retrieval

Mathematically, using the pulse to gate itself complicates the problem. The FROG trace must be inverted to find the intensity and phase of the pulse. Spectrogram inversion algorithms used to obtain the field (or intensity and phase) require knowledge of the gate function. Since the gate is related to the pulse and is unknown, such algorithms cannot be used for FROG. Other methods are needed. The solution to the inversion of FROG data is to recast the problem as a two-dimensional phase retrieval problem.^{14-16,18} Instead of thinking of the problem as a gating problem, consider the signal field $E_{sig}(t, \tau)$ to be the Fourier transform with respect to τ of a new quantity $E_{sig}(t, \Omega)$. We note that once $E_{sig}(t, \Omega)$ is found, the pulse field is easily obtained by setting Ω equal to zero. That is $E(t) = E_{sig}(t, \Omega=0)$ to within a complex multiplicative constant that is typically unimportant. Thus finding $E_{sig}(t, \Omega)$ is equivalent to finding $E(t)$. Rewriting the expression for the FROG trace in terms of $E_{sig}(t, \Omega)$ gives

$$I_{FROG}(\omega, \tau) = \left| \int_{-\infty}^{\infty} \int_{-\infty}^{\infty} E_{sig}(t, \Omega) \exp(-i\omega t - i\Omega \tau) dt d\Omega \right|^2. \quad (10)$$

Thus the measured quantity $I_{FROG}(\omega, \tau)$ is the squared magnitude of the two-dimensional Fourier transform of $E_{sig}(t, \Omega)$. The FROG trace thus yields the magnitude, but not the phase, of the two-dimensional Fourier transform of $E_{sig}(t, \Omega)$. Finding the phase of the Fourier transform of $E_{sig}(t, \Omega)$ is the two-dimensional phase retrieval problem, which is a solved problem from

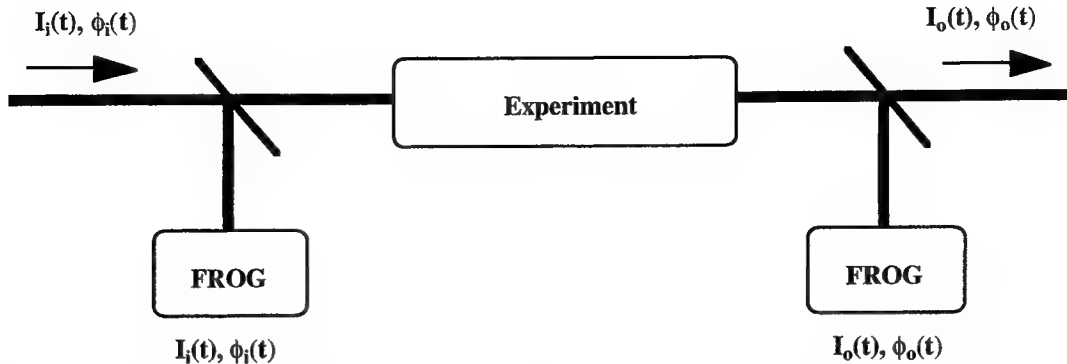


Figure 5 Generic experiment based on frequency-resolved optical gating (FROG). Instead of measuring only the spectrum and autocorrelation of the input pulse and the energy (or time-resolved energy) of the output pulse as in Figure 1, the experiment measures the full intensity and phase of both the input and output pulses. Thus essentially all information contained in the temporal or spectral behavior of the pulse is obtained.

image science.¹⁹ The measured trace and knowledge of the mathematical form of $E_{sig}(t, \Omega)$ are sufficient to retrieve the full intensity and phase of a pulse by using an iterative Fourier transform algorithm^{13,20}.

3.4. Generic Experiments using FROG

Rather than considering the FROG phase retrieval algorithm, which has been discussed in previous publications,^{13,20} consider the impact of knowing how to measure the full intensity and phase of a pulse on potential experiments in ultrafast science. Instead of relying on partial information such as that provided by an experiment of the form shown in Figure 1, now the full intensity and phase may be measured in a new generic experiment shown in Figure 5.

Using such an experiment, it is now possible to measure the full intensity and phase (or equivalently the electric field) of both the input and output pulses. Thus, for instance if the experiment were to simply replace the block labeled "Experiment" in Figure 5 with a length of some material, the complex transmission coefficient of the material could be obtained over the wavelength of the pulse by simply dividing the measured electric field of the input pulse by the measured electric field of the output pulse. Thus essentially all information contained in the temporal or spectral behavior of the pulse is obtained. Moreover, by using pulse shaping techniques²¹, it is also now possible to control the pulse shape of the input pulse. These pulse shaping techniques have already been applied to a variety of fields including nuclear magnetic resonance in dipolar broadened spin systems²² and quantum control of wavepackets²³, and greatly increase the number of possible experiments. Measurement techniques such as FROG make using pulse shaping techniques much more feasible.

4. SPECTRAL INTERFEROMETRY

4.1. Need to Measure Weak Pulses

Despite the great breakthrough in pulse measurement that FROG represents, one characteristic of FROG can make it less than ideal for some experiments. Specifically, FROG requires a nonlinear interaction, which limits its use to pulses strong enough to produce a measurable nonlinear signal. For SHG FROG, this limits the measurement to optical pulses with energies of about a picojoule. As shown by Walmsley and Wong²⁴, all techniques for measuring an isolated pulse must use a nonlinear interaction, not just FROG. Thus all techniques for measuring isolated pulses have similar energy requirements. Many ultrafast nonlinear-optical material-characterization experiments, however, yield signal pulse energies of femtojoules or less. In general, only the signal-pulse energy has been measured in such experiments. Many researchers, however, have realized that significantly more material information is available if the signal pulse is better characterized. Chemla and coworkers²⁵ and Patkar and coworkers²⁶ have used several pulse-characterization methods to characterize the signal pulses in four-wave-mixing experiments performed on semi-conductors. Consequently, they have significantly improved our understanding of the physics of multiple-quantum wells, for example. Measuring an isolated ultraweak pulse by itself is a daunting task, but by combining spectral interferometry and FROG it is now possible to completely characterize the intensity

and phase of pulses with energies in the zeptojoule range (1 zeptojoule = 10^{-21} joules). This combination makes possible experiments that rely on understanding the intensity and phase behavior of ultraweak pulses.

4.2. Spectral Interferometry

Spectral interferometry (SI), a technique for measuring the phase difference between two pulses—say a reference and an unknown pulse—was first introduced by Froehly and coworkers,^{27,28} and it has been used for several applications since then.²⁹⁻³¹ It involves simply combining at a beamsplitter the two pulses whose relative phase is desired and directing the two pulses collinearly into a spectrometer. The spectrum of the two pulses is simply given by:

$$I_{SI}(\omega) = I_{ref}(\omega) + I_{unk}(\omega) + 2\sqrt{I_{ref}(\omega)}\sqrt{I_{unk}(\omega)}\cos[\phi_{unk}(\omega) - \phi_{ref}(\omega) - \omega\tau] \quad (11)$$

where $I_{ref}(\omega)$ and $I_{unk}(\omega)$ are the spectra of the reference and unknown (weak) pulses, respectively, and τ is the delay between the two pulses. The delay (only one delay is necessary) is chosen to yield fringes in the sum spectrum. The two individual pulse spectra are measured by blocking one beam and measuring the spectrum of the other and vice versa. The only remaining unknown in Equation 11, the phase difference, $\phi_{unk}(\omega) - \phi_{ref}(\omega) - \omega\tau$, is then determined by the SI spectrum, $I_{SI}(\omega)$. It is easily extracted non-iteratively using one of several well-known fringe-inversion techniques.^{30,32} In fact, the relative delay also emerges from the analysis (it is the linear term) and hence does not need to be independently measured. An advantage of SI is that it is a type of heterodyne technique, which can act to amplify the weak pulse. For example, the reference pulse may be chosen to be, say, M times more intense than the unknown pulse, yielding fringes that are $4M^{1/2}$ times as intense as the spectrum of the unknown pulse. The only requirement of SI is that the spectrum of the unknown pulse lies within that of the reference pulse.

Note that SI is a linear technique (the reference pulse eliminates the need for a nonlinear interaction), so it is highly sensitive. Also, if the phase of the reference pulse is known, SI may be used to obtain both the spectrum and spectral phase of the pulse. Using Equation 3, this then gives the electric field of the pulse and completely characterizes the pulse. During the majority of the time that SI has existed, however, measuring the reference pulse was impossible. Thus the technique was limited to measuring only phase differences or pulses with phase distortions that were large compared to the phase distortions of the reference, and making the assumption that the reference pulse was spectrally limited.

4.3. Combining FROG and Spectral Interferometry

With the invention of techniques such a FROG, it is now a simple matter to measure ultraweak pulses because in most cases the ultraweak pulse is produced from a strong pulse directly from a laser. Thus in almost all cases a reference pulse is available. We first use FROG to characterize the reference pulse directly from the laser (although any method that yields the reference-pulse phase vs. frequency, $\phi_{ref}(\omega)$, will suffice). By characterizing the pulse using FROG, we avoid the necessity of assuming a spectrally limited pulse. We then use SI to measure the frequency-domain phase difference between the two

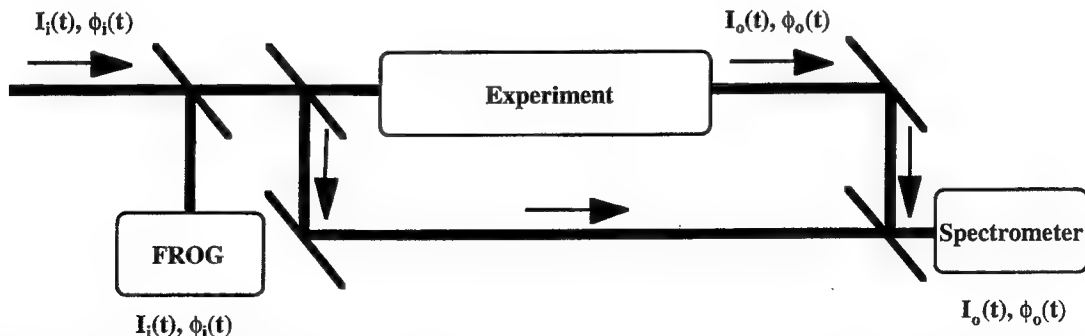


Figure 6 Generic experiment based on TADPOLE (the combination of FROG and spectral interferometry). The experiment measures the full intensity and phase of both the input and output pulses, even for extremely weak pulses. TADPOLE measurements have been performed on pulses with energies as low as 42 zeptojoules (42×10^{-21} joules). Moreover, by using the non-dispersed dimension in the spectrometer, it is possible to measure the intensity and phase as a function of position along the entrance slit of the spectrometer as well as time.

pulses. The FROG and SI measurements together yield the full intensity and phase of the unknown ultraweak ultrashort pulse in the frequency domain. Thus, the combination of FROG and SI, which is sometimes called temporal analysis by dispersing a pair of light e-fields (TADPOLE), provides a nearly general technique for measuring even the weakest ultrashort laser pulses. So far, this technique has been used to measure pulses with energies as low as 42 zeptojoles, or 42×10^{-21} joules.³² Moreover, since only one physical dimension of the detector is used for the spectral measurement, spatial information may be obtained by using the other dimension in an imaging spectrograph. Thus TADPOLE allows measurements of the intensity and phase as a function of position as well as time.

4.4. Polarization Measurement

In addition to measuring intensity and phase as a function of time (or frequency) and space, TADPOLE may also be used to measure the time-dependent polarization state of a pulse by using a dual-beam geometry to measure the time dependent phase of two orthogonal polarizations.^{33,34} Consider a pulse propagating in the z direction. If we define two components x and y of the electric field that are orthogonal to the z and each other, we may perform a spectral interferometry measurement on each component using a linearly polarized reference pulse at 45° with respect to the x -axis, so that it has equal x and y components. The experimental pulse x and y components may have arbitrarily varying intensities and phases as a function of time. One performs a spectral interferometric measurement on the x and y components of the pulse by introducing a fixed delay between the reference pulse and the signal, combining the reference and signal collinearly, separating the combined reference and signal into x and y components, and measuring the x and y components separately in a spectrometer.

The measured signals have the same form as for single channel spectral interferometry

$$I_{SI}^i(\omega) = I_{ref}^i(\omega) + I_{unk}^i(\omega) + 2\sqrt{I_{ref}^i(\omega)}\sqrt{I_{unk}^i(\omega)}\cos[\phi_{unk}^i(\omega) - \phi_{ref}^i(\omega) - \omega\tau] \quad (12)$$

Here i indicates the x or y component. Since the same pulse is used as a reference for the two polarizations, the relative phase of the two components is obtained as well as the full intensity and phase (electric field) of the two components individually. Thus having measured two orthogonal electric fields of the pulse and the phase relationship between those fields, the full time dependent field may be obtained including the polarization state. This method has already been used to study coherent processes in quantum confined structures by measuring the intensity, phase and polarization state of coherent four-wave-mixing signals from GaAs quantum wells.³⁴

5. CONCLUSION: THE NEW GENERIC EXPERIMENT

Until recently, experiments in ultrashort pulse science have involved measuring the spectrum and autocorrelation of the input pulse(s) and only measuring the integrated energy or perhaps time-resolved energy of the output signal. These experiments ignored the information contained in the input and output pulse phases and intensity profiles. New pulse measurement techniques, however, such as frequency-resolved optical gating (FROG) combined with older techniques such as spectral interferometry, now allow the complete characterization of the intensity, phase and polarization state of ultrashort pulses as functions of time and position. These techniques work for wavelengths from the UV to the IR and for extremely weak pulses and very high power pulses. They also allow entirely new classes of experiments for measuring ultrafast phenomena. Now the phases and temporal profiles of the input may be measured and controlled, and the intensity and phase of the output pulses can also be measured. These new measurement techniques have thus greatly increased the information that can be obtained in ultrafast experiments. This talk will review current pulse measurement methods including frequency-resolved optical gating and spectral interferometry and describe how they are changing the way that ultrashort pulse experiments are performed.

6. ACKNOWLEDGMENTS

The author acknowledges the enormous contributions that Rick Trebino, Ken DeLong, John Sweetser, Marco Krumbügel, Ian Walmsley, Art Smirl, Wojtek Walecki and many others have made to this work.

7. REFERENCES

1. M. Maier, W. Kaiser, and J. A. Giordmaine, "Intense light bursts in the stimulated Raman effect," *Phys. Rev. Lett.*, vol. 17, pp. 1275-1277, 1966.
2. J. A. Armstrong, "Measurement of picosecond laser pulse widths," *Appl. Phys. Lett.*, vol. 11, pp. 16-18, 1967.

3. J. Etchepare, G. Grillon, and A. Orszag, "Third Order Autocorrelation Study of Amplified Subpicosecond Laser Pulses," *IEEE J. Quant. Electron.*, vol. 19, pp. 775-778, 1983.
4. R. Fischer, J. Gauger, and J. Tilgner, "Fringe Resolved Third-Order Autocorrelation Functions," *Proceedings of American Institute of Physics Conference*, vol. 172, pp. 727-729, 1988.
5. D. M. Rayner, P. A. Hackett, and C. Willis, "Ultraviolet Laser, Short Pulse-Width Measurement by Multiphoton Ionization Autocorrelation," *Review of Scientific Instruments*, vol. 53, pp. 537-538, 1982.
6. R. Trebino, C. C. Hayden, A. M. Johnson, W. M. Simpson, and A. M. Levine, "Chirp and Self-Phase Modulation in Induced-Grating Autocorrelation Measurements of Ultrashort Pulses," *Opt. Lett.*, vol. 15, pp. 1079-1081, 1990.
7. P. Yeh, "Autocorrelation of Ultrashort Optical Pulses Using Polarization Interferometry," *Optics Letters*, vol. 8, pp. 330-332, 1983.
8. K. L. Sala, G. A. Kenney-Wallace, and G. E. Hall, "CW autocorrelation measurements of picosecond laser pulses," *IEEE J. Quant. Electron.*, vol. QE-16, pp. 990-996, 1980.
9. J. F. James and R. S. Sternberg, *The design of optical spectrometers*. London: Chapman & Hall, 1969.
10. K. Naganuma, K. Mogi, and H. Yamada, "General method for ultrashort light pulse chirp measurement," *IEEE J. Quant. Electron.*, vol. 25, pp. 1225-1233, 1989.
11. A. Rundquist and J. Peatross, "Pulse characterization with the use of temporal information via intensity," presented at OSA Annual Meeting, Long Beach, California, 1997.
12. I. A. Walmsley and R. P. Trebino, "Measuring fast pulse with slow detectors," *Opt. Photonics News*, vol. 7, pp. 23-28, 33, 1996.
13. R. Trebino, K. W. DeLong, D. N. Fittinghoff, J. N. Sweetser, M. A. Krumbiegel, B. A. Richman, and D. J. Kane, "Measuring ultrashort laser pulses in the time-frequency domain using frequency-resolved optical gating," *Rev. Sci. Instrum.*, vol. 68, pp. 3277-95, 1997.
14. K. W. DeLong, R. Trebino, J. R. Hunter, and W. E. White, "Frequency-resolved optical gating with the use of second-harmonic generation," *J. Opt. Soc. Am. B*, vol. 11, pp. 2206-2215, 1994.
15. R. Trebino and D. J. Kane, "Using Phase Retrieval to Measure the Intensity and Phase of Ultrashort Pulses: Frequency-Resolved Optical Gating," *J. Opt. Soc. Amer. A*, vol. 10, pp. 1101-1111, 1993.
16. D. J. Kane and R. Trebino, "Characterization of Arbitrary Femtosecond Pulses Using Frequency-Resolved Optical Gating," *IEEE Journal of Quantum Electronics*, vol. 29, pp. 571-579, 1993.
17. T. Tsang, M. A. Krumbügel, K. W. DeLong, D. N. Fittinghoff, and R. Trebino, "Frequency-resolved optical-gating measurements of ultrashort pulses using surface third-harmonic generation," *Opt. Lett.*, vol. 21, pp. 1381-1383, 1996.
18. D. J. Kane and R. Trebino, "Single-Shot Measurement of the Intensity and Phase of an Arbitrary Ultrashort Pulse By Using Frequency-Resolved Optical Gating," *Opt. Lett.*, vol. 18, pp. 823-825, 1993.
19. H. Stark, "Image Recovery: Theory and Application," Orlando: Academic Press, 1987.
20. K. W. DeLong, D. N. Fittinghoff, R. Trebino, B. Kohler, and K. Wilson, "Pulse retrieval in frequency-resolved optical gating based on the method of generalized projections," *Optics Letters*, vol. 19, pp. 2152-2154, 1994.
21. C. W. Hillegas, J. X. Tull, D. Goswami, D. Strickland, and W. S. Warren, "Femtosecond laser pulse shaping using microsecond radiofrequency pulses," *Opt. Lett.*, pp. submitted for publication, 1994.
22. C. J. Lee, N. Murali, and W. S. Warren, "Applications of Shaped Pulses to High-Resolution Nuclear Magnetic Resonance in Dipolar Broadened Spin Systems," *Advances in Magnetic Resonance*, vol. 14, pp. 241-268, 1990.
23. B. Kohler, V. V. Yakovlev, J. Che, J. L. Krause, M. Messina, K. R. Wilson, N. Schwentner, R. M. Whitnell, and Y. Yan, "Quantum control of wave packet evolution with tailored femtosecond pulses," *Phys. Rev. Lett.*, vol. 74, pp. 3360-3363, 1995.
24. I. A. Walmsley and V. Wong, "Characterization of the electric field of ultrashort optical pulses," *Journal of the Optical Society of America B (Optical Physics)*, vol. 13, pp. 2453-2463, 1996.
25. D. S. Chemla, J. Y. Bigot, M. A. Mycek, S. Weiss, and W. Shäfer, "Ultrafast phase dynamics of coherent emission from excitons in GaAs quantum wells," *Phys. Rev. B*, vol. 50, pp. 8439-8453, 1994.
26. S. Patkar, A. E. Paul, W. Sha, J. A. Bolger, and A. L. Smirl, "Degree and state of polarization of the time-integrated coherent four-wave mixing signal from semiconductor multiple quantum wells," *Phys. Rev. B*, vol. 51, pp. 10789-10794, 1995.
27. C. Froehly, A. Lacourt, and J. C. Vienot, "Time impulse response and time frequency response of optical pupils. Experimental confirmations and applications," *Nouvel Revue d'Optique*, vol. 4, pp. 183-196, 1973.
28. J. Piasecki, B. Colombeau, M. Vampouille, C. Froehly, and J. A. Arnaud, "A new technique for measuring the impulse response of optical fibres," *Appl. Opt.*, vol. 19, pp. 3749-55, 1980.
29. F. Reynaud, F. Salin, and A. Barthelemy, "Measurement of Phase Shifts Introduced By Nonlinear Optical Phenomena on Subpicosecond Pulses," *Optics Letters*, vol. 14, pp. 275-277, 1989.
30. L. Lepetit, G. Cheriaux, and M. Joffre, "Linear techniques of phase measurement by femtosecond spectral interferometry for applications in spectroscopy," *J. Opt. Soc. Am. B*, vol. 12, pp. 2467-2474, 1995.

31. L. Lepetit and M. Joffre, "Two-dimensional nonlinear optics using Fourier-transform spectral interferometry," *Opt. Lett.*, vol. 21, pp. 564-566, 1996.
32. D. N. Fittinghoff, J. L. Bowie, J. N. Sweetser, R. T. Jennings, M. A. Krumbügel, K. W. DeLong, R. Trebino, and I. A. Walmsley, "Measurement of the Intensity and Phase of Ultraweak, Ultrashort Laser Pulses," *Optics Letters*, vol. 21, pp. 884-886, 1996.
33. W. J. Walecki, D. N. Fittinghoff, A. L. Smirl, and R. Trebino, "Characterization of the polarization state of weak ultrashort coherent signals by dual-channel spectral interferometry," *Optics Letters*, vol. 22, pp. 81-83, 1997.
34. X. Chen, W. J. Walecki, O. Buccafusca, D. N. Fittinghoff, and A. L. Smirl, "Temporally and spectrally resolved amplitude and phase of coherent four-wave-mixing emission from GaAs quantum wells," *Phys. Rev. B*, vol. 56, pp. 9738-9743, 1997.

SESSION 3

Ophthalmic Applications of Ultrashort-Pulse Lasers

Laser-induced breakdown in the eye at pulse durations from 80 ns to 100 fs

Alfred Vogel¹, Joachim Noack¹, Kester Nahen¹, Dirk Theisen¹, Reginald Birngruber¹, Daniel X. Hammer², Gary D. Noojin², and Benjamin A. Rockwell²

1) Medical Laser Center Lübeck D-23562 Lübeck, Germany

2) Optical Radiation Division, Armstrong Laboratory, Brooks AFB, TX 78235, USA

ABSTRACT

Nonlinear absorption through laser-induced breakdown (LIB) offers the possibility of localized energy deposition in linearly transparent media and thus of non-invasive surgery inside the eye. The general sequence of events - plasma formation, stress wave emission, cavitation - is always the same, but the detailed characteristics of these processes depend strongly on the laser pulse duration. The various aspects of LIB are reviewed for pulse durations between 80 ns and 100 fs, and it is discussed, how their dependence on pulse duration can be used to control the efficacy of surgical procedures and the amount of collateral effects.

Key Words: Optical breakdown, intraocular microsurgery, ultrashort laser pulses, breakdown thresholds, plasma formation, moving breakdown, plasma transmission, shock waves, cavitation, self focusing.

1. INTRODUCTION

Nonlinear absorption through laser-induced breakdown (LIB)^{1,2} can occur at material surfaces as well as inside media which are transparent at low light intensities. Nevertheless, the characteristics of LIB are very different in both cases. At material surfaces LIB competes with material ablation based on linear absorption and has, besides some characteristic features, many aspects in common with the latter^{3,4}. LIB inside of linearly transparent media offers a possibility of localized energy deposition which can be achieved by no other optical means. This unique feature enables non-invasive surgery inside the eye^{1,5}, and it has been suggested to apply it for the design of 3-dimensional storage elements⁶. The results described in this review were obtained with distilled water used as a model substance for the transparent media of the eye. This simplification guaranteed reproducibility of the experimental results and is justified by the fact that the thresholds for optical breakdown in distilled water are very similar to the breakdown thresholds in the ocular media^{7,8}. The review focuses attention on the dependence of the breakdown events on laser pulse duration and discusses, how that dependence can be used to control the efficacy of surgical procedures and the amount of collateral effects.

2. OPTICAL BREAKDOWN

Optical breakdown consists of the generation of large amounts of free electrons ($\geq 10^{18} \text{ cm}^{-3}$ ^{9,10}) in the medium by multiphoton ionization (MPI) and cascade ionization via inverse bremsstrahlung absorption (CI). The rate of MPI has a very strong intensity dependence ($\propto I^K$ where K is the number of photons required for ionization), whereas the intensity

Correspondence: Alfred Vogel, PhD, Medical Laser Center Lübeck, Peter-Monnik-Weg 4, D-23562 Lübeck, Germany.
FAX: xx49-451-505 486; e-mail: vogel@mll.mu-luebeck.de

dependence of the rate of CI is much weaker ($\propto I$ when electron losses from the focal volume are neglected)¹¹. When the laser pulse duration is reduced, a higher intensity of the laser radiation is required for the breakdown to be completed within the pulse duration. Since the MPI rate increases more strongly with I than the CI rate, MPI gains ever more importance with shorter pulse durations. For pulses below ≈ 1 ps, CI is furthermore limited by time constraints, since one doubling sequence in the ionization cascade lasts at least 6 fs (for water and $\lambda = 1064$ nm)¹³, whereas MPI can occur "instantaneously"². The changing interplay between MPI and CI with decreasing pulse duration is one main reason for the changes in the breakdown characteristics as a whole.

Another major factor is the changing energy distribution between electrons and heavy particles which influences the energy density in the plasma and thus the radiant energy threshold for breakdown. Optical energy is deposited into the medium through generation of free electrons. With ns-pulses, a temperature equilibrium between electrons and heavy particles is achieved during the pulse through recombination processes, and therefore the average energy density is high¹². With ultrashort pulses, however, very little energy has been transferred to the heavy particles at the end of the laser pulse. An equilibrium temperature develops only after the laser pulse. The equilibrium temperature will thus be much lower than in the case of the ns-pulses, particularly because the specific heat of the electrons is much smaller than that of the ions and other heavy particles¹². Due to the smaller average energy density in plasmas produced with ultrashort laser pulses, the radiant energy threshold for breakdown is smaller than with ns-pulses, and the mechanical effects after breakdown (shock wave emission and cavitation) are less extensive.

A third reason for changes of the breakdown characteristics with decreasing pulse duration is the increasing role of self focusing effects which goes along with the higher laser powers required to complete breakdown in a shorter period of time. Self focusing changes the breakdown threshold, the plasma transmission, and, probably most importantly, the shape of the breakdown region as well as the energy distribution within that region (Fig. 1).

The statements made above about the three main factors influencing the pulse duration dependence of breakdown are in the following discussed in more detail and supported by experimental evidence.

3. BREAKDOWN THRESHOLDS

The evolution of the free electron density under the influence of a laser pulse can be described by the rate equation^{9,13,14}

$$\frac{d\rho}{dt} = \eta_{\text{mp}} + \eta_{\text{casc}} \rho - g \rho - \eta_{\text{rec}} \rho^2 \quad (1)$$

The first two terms describe the creation of free electrons through multiphoton and cascade ionization, whereas the losses by electron diffusion out of the focal volume and by recombination are represented by the last two terms. In order to predict LIB thresholds, several authors have solved this equation neglecting different terms and using different expressions for the individual terms^{9,13-15}. Recently Noack et al.¹⁶ presented an analysis based on all four terms including the recombination term, which was based on experimental data¹⁷. For the other terms, the expressions of Kennedy's first order model¹³ were used. When solving Eq. (1), it has to be considered that CI can only take place when free electrons are already present in

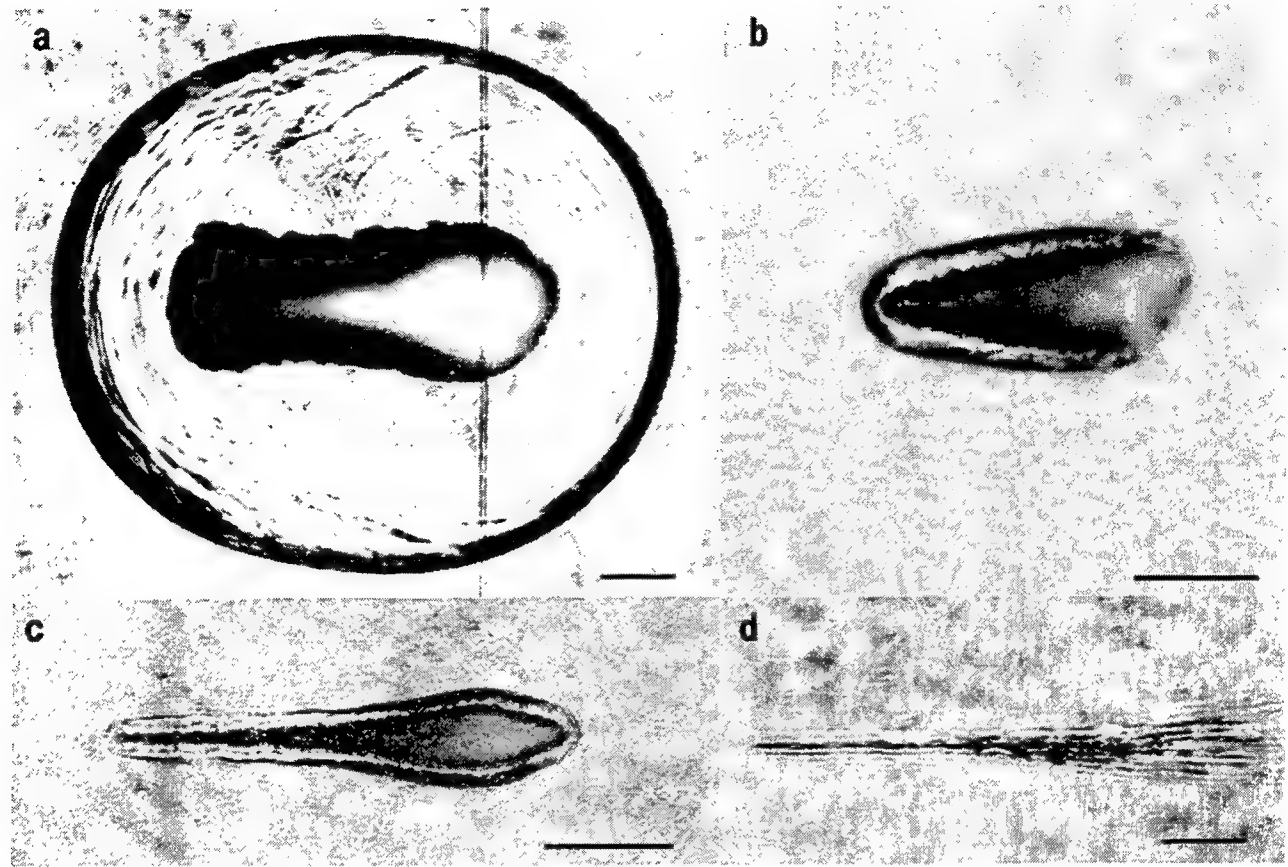


Figure 1: Optical breakdown at various pulse durations. (a) Pulse duration $\tau_L = 76$ ns, wavelength $\lambda = 750$ nm, focusing angle $\theta = 19^\circ$, $E = 50$ mJ, $E/E_{th} = 9$, picture taken 120 ns after breakdown (the line is a slit used for simultaneous streak photography, and has otherwise no physical meaning); (b) $\tau_L = 6$ ns, $\lambda = 1064$ nm, $\theta = 22^\circ$, $E = 8.2$ mJ, $E/E_{th} = 60$, $\Delta t = 10$ ns; (c) $\tau_L = 30$ ps, $\lambda = 1064$ nm, $\theta = 14^\circ$, $E = 740$ μ J, $E/E_{th} = 150$, $\Delta t = 8$ ns; (d) $\tau_L = 100$ fs, $\lambda = 580$ nm, $\theta = 16^\circ$, $E = 35$ μ J, $E/E_{th} = 200$, $\Delta t = 3$ ns. The light is always incident from the right, the bars represent a length of 100 μ m.

the interaction volume. In pure media like distilled water, MPI is required to provide the initial electrons. Therefore, CI was only included in the calculations after the probability of finding an electron in the interaction volume V had risen above 50% through MPI. The time constraint for CI given by the time Δt for an electron to gain enough energy through inverse bremsstrahlung absorption to ionize another electron was considered by evaluating the contribution of CI at a retarded time $(t - \Delta t)$. Following Kennedy^{13,31}, we chose $\Delta t = 30$ fs. The breakdown threshold was defined as the minimum irradiance where a critical electron density of $\rho_{cr} = 10^{20}$ cm⁻³ was exceeded during the laser pulse. This threshold was obtained by solving Eq. (1) iteratively for different intensities.

Table 1 summarizes various experimental threshold values I_{50} (50% breakdown probability) obtained at different laser wavelengths^{11,16,18}, together with the calculated threshold values I_{rate} for the same laser parameters¹⁶. For all pulse durations except 60 ps the calculated and experimental thresholds deviate by less than a factor of 1.4.

pulse duration	wavelength [nm]	measured spot diameter [μm]	E_{50} [μJ]	I_{50} [10^{11} Wcm^{-2}]	F_{50} [Jcm^{-2}]	I_{rate} [10^{11} Wcm^{-2}]
76 ns	750	20	5500	0.23	1750	0.27
6 ns	532	5.3	39	0.29	174	0.35
60 ps	532	5.6	4.1	2.8	16.8	0.62
3 ps	580	5.0	0.51	8.5	2.6	7.10
300 fs	580	5.0	0.29	47.6	1.4	41.0
100 fs	580	4.4	0.17	111.0	1.1	84.0

Table 1: Measured breakdown thresholds E_{50} , I_{50} and F_{50} , and calculated breakdown thresholds I_{rate} for various laser pulse durations.

The numerical solution of Eq. (1) does not only allow the calculation of breakdown thresholds, but also provides insight into the differences between the breakdown mechanisms at different pulse durations. To discuss these differences, Figure 2 presents the evolution of the free electron density for laser pulses of different duration, and Figure 3 shows the predicted threshold I_{rate} as a function of laser pulse duration for two different wavelengths.

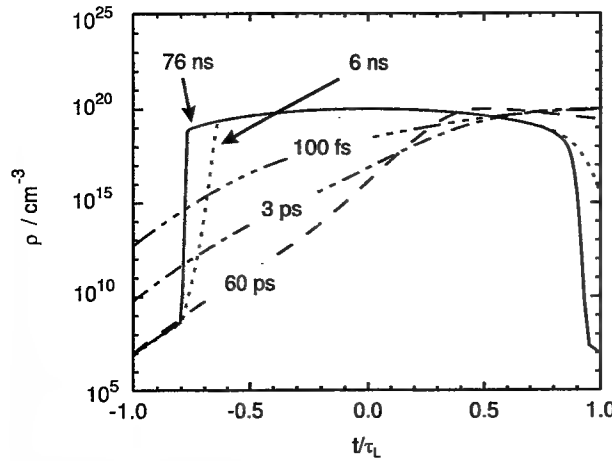


Figure 2: Evolution of the free electron density at threshold irradiance for laser pulses of different durations τ_L . All curves were calculated for $\lambda = 580 \text{ nm}$ and $6 \mu\text{m}$ focus diameter. The irradiance maximum of the Gaussian laser pulse is reached at $t = 0$.

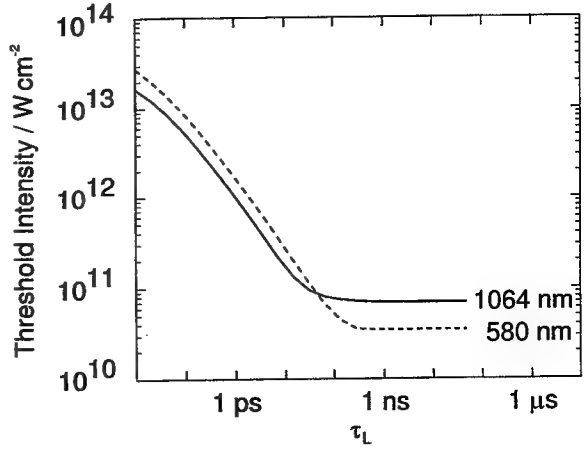


Figure 3: Irradiance threshold I_{rate} as a function of laser pulse duration calculated for $\lambda = 1064 \text{ nm}$ and $\lambda = 580 \text{ nm}$ ($6 \mu\text{m}$ focus diameter).

In pure media as distilled water, the initial electrons for the breakdown process must be generated by MPI, even at pulse durations where breakdown is otherwise dominated by CI. For nanosecond pulses, the electron density initially rises only slowly through multiphoton absorption, because η_{mp} is small at the threshold irradiance for breakdown. After the creation of the first electron in the interaction volume at $t \approx 0.8 \tau_L$, the beginning CI raises the electron density by almost

11 orders of magnitude within a small fraction of the laser pulse (≈ 1 ns) (Fig. 2: 76 ns, 6 ns). The high rate of CI is due to the relatively high irradiance required for MPI of the initial electron. The growth of the free electron density is slowed down at high electron concentrations by the rapidly increasing influence of recombination ($\propto \rho^2$). Because of the strong influence of recombination, ρ_{cr} is reached near the peak of the laser pulse. As long as this is the case, the threshold intensity required to overcome the recombination losses is nearly independent of the pulse duration (Fig. 3).

For shorter laser pulses, the ionization cascade becomes slower with respect to the pulse duration. Around 1 ns, the pulse duration becomes comparable to the rise time of the electron density through CI, and for shorter pulses a higher $\eta_{casc} \propto I$ is required to complete the cascade during the pulse. The rising threshold intensity implies that CI can compensate the recombination losses even during the second half of the laser pulse when the intensity has dropped below its maximum value. For 60 ps pulses, ρ_{cr} is therefore reached after the peak of the laser pulse (Fig. 2: 60 ps).

Whereas for nanosecond pulses MPI was only required to produce seed electrons for the cascade, it gains ever more importance with decreasing pulse duration (i.e. increasing threshold intensity) because of its strong intensity dependence ($\propto I^K$). For pulse durations around and below 1 ps, MPI provides a large number of seed electrons for the ionization cascade and contributes significantly to the generation of free electrons, particularly during the first half of the laser pulse (Fig. 2: 3 ps, 100 fs). For $\tau_L < 1$ ps, the critical electron density could not be reached by CI alone, regardless of irradiance, because one doubling sequence in the ionization cascade takes ≥ 6 fs. Nevertheless, CI is still the dominant mechanism at all pulse durations investigated in our study, only at pulse durations below ≈ 40 fs, the majority of the free electrons is produced by MPI^{15,50}.

The above discussion shows, how the interplay of MPI, CI and recombination changes with laser pulse duration. The influence of recombination has been underestimated in previous investigations^{11,13}. Its neglect does not lead to very different threshold values¹⁹, but it obscures the role played by recombination in the energy transfer between electrons and heavy particles. The recombination losses occurring during the ns pulses lead to a continuous heating of the heavy particles and thus to an increase of the average energy density in the interaction volume. Therefore, a much larger radiant exposure F_{50} is required for breakdown at long pulse durations, particularly at 76 ns, than with ps and fs pulses (Table 1). For pulse durations ≤ 3 ps, F_{50} varies only slightly, because recombination losses during the laser pulse are always minor and thus almost independent of pulse duration. Other factors which could also contribute to the dependence of F_{50} on pulse duration but were not considered in our calculations, are alterations of the plasma size at threshold and variations of ρ_{cr} . They will be discussed in the following sections.

4. PLASMA FORMATION AT SUPERTHRESHOLD ENERGIES

When pulses with superthreshold peak irradiance are applied, the plasma grows during the laser pulse. For ps- and ns-pulses, the plasma is first formed at the beam waist, and then grows "upstream" toward the incoming laser beam^{11,20} ("moving breakdown"). Hardly any plasma is formed beyond the laser focus, because most of the laser light is already absorbed upstream^{11,21,22} ("plasma shielding"). For picosecond pulses, the position of the plasma front at each time is

approximately defined by iso-intensity lines with $I = I_{th}$, and the plasma length at the end of the pulse is proportional to $\sqrt{\beta - 1}$ where $\beta = E/E_{th} = II_{th}$ denotes the normalized pulse energy or peak irradiance, respectively¹¹. For nanosecond pulses, the irradiance threshold is lowered to a value I'_{th} after the plasma formation has started, because UV-plasma radiation generates free electrons in the vicinity of the plasma which make the MPI-generation of seed electrons superfluous. The movement of the breakdown wave is approximately determined by iso-intensity lines with $I = I'_{th}$, and ns-plasmas are therefore considerably longer than ps-plasmas at the same value of β ¹¹. The relative deviation between the length of ns- and ps-plasmas at equal β is largest for large focusing angles and near the breakdown threshold (up to six-fold at $\theta = 22^\circ$). With ps-pulses, the UV plasma radiation does not modify the breakdown threshold, because there are always enough seed electrons produced by MPI.

With fs-pulses, the spatial extension of the laser pulse is shorter than the plasma length at superthreshold energies. Therefore, the breakdown starts in front of the laser focus, and the breakdown wave moves with the laser pulse, leaving free electrons in its wake²². Despite of the different direction of the breakdown wave, the length of the breakdown region scales in a similar way with β as in the case of ps-pulses¹⁸.

The plasma growth in upstream direction occurring during ns- and ps- laser pulse reduces the light absorption at each point of the plasma and thus limits the average energy density within the plasma to values which do not differ much from the energy density at threshold. With fs-pulses, the energy density in the plasma is limited by the fact that for increasing β the onset of MPI starts further and further upstream. This reduces the peak power and irradiance nearer to the laser focus, like in the case of the longer pulses.

5. ENERGY DEPOSITION

Only the energy absorbed in the sample is effective for plasma-mediated surgery (and for material processing in general); light transmission through the plasma as well as scattering and reflection by the plasma reduce the efficacy of the process. The plasma absorption cannot be measured directly, but can be deduced by measuring the transmission, scattering, and reflection: $A = 1 - T - S - R$. Nahen and Vogel²¹ found in a recent study performed with pulse durations of 6 ns and 30 ps that the back reflection from the plasmas into the focusing lens amounts to less than 1.7% for both pulse durations, and that the forward scattering into an angle of $\pm 30^\circ$ around the optical axis amounts to less than 0.5% for ns-pulses and to less than 7.6% for ps-pulses. Near threshold, considerably more light was transmitted through the plasma than reflected or scattered. Well above threshold ($\beta \approx 100$) the relative importance of transmission decreased, but transmission was still twice as large as scattering and reflection together. For all laser parameters, considerably less light was reflected or scattered by the plasma than absorbed. The plasma absorption is thus approximately given by $A \approx (1-T)$ and its assessment for a larger parameter range is possible through transmission measurements alone. This differs from plasma formation at surfaces, where reflection plays a large role²³. The difference is due to the fact that inside a homogeneous, linearly transparent medium the breakdown front moves during the laser pulse (see section 4). The moving breakdown limits the

electron density at each location within the plasma. The plasma frequency remains therefore smaller than the frequency of the laser light, and the laser-plasma-coupling is not impaired.

Figure 4 shows measured transmission values¹⁸ as a function of laser pulse duration for two different values of the dimensionless laser pulse energy β . The transmission is small in the nanosecond range, but considerably larger for ps-pulses. When the pulse duration is further reduced into the femtosecond range, the transmission decreases again. At first sight, the experimental data are not easily understood when the maximum electron density in the plasma is assumed to be independent of the laser pulse duration. This assumption ($\rho_{cr} = \text{const.}$) was made for the threshold calculations in section 3 and led to a very good agreement between predicted and measured threshold values.

To explain the $T(\tau_L)$ dependence, one has to consider that the measured transmission values represent a time average over the whole laser pulse duration. They must, hence, be compared with the complete time evolution of the electron density during the laser pulse, and not just with the maximum density. The time averaged absorption coefficient α_{LIB} near threshold can be estimated from the absorption cross section for inverse bremsstrahlung σ_a ²⁴ and the temporal evolution of the free electron density obtained by integration of Eq. (1) to be¹⁶

$$\alpha_{LIB} \approx \sigma_a \frac{\int I(t) \rho(t) dt}{\int I(t) dt}. \quad (2)$$

Figure 5 shows the calculated values for α_{LIB} as a function of pulse duration¹⁶. The absorption coefficient is largest for nanosecond pulses (800 cm^{-1}) because of the high electron density throughout the laser pulse (see Fig. 2). Since the evolution of the free electron density is very similar for pulse durations between 1 and 100 ns, the absorption coefficient is almost constant in this regime. With decreasing laser pulse duration, high electron densities are only encountered during the second half of the laser pulse (Fig. 2: 60 ps, 3 ps). Therefore the time averaged absorption drops and reaches a minimum value of 150 cm^{-1} for a pulse duration around 2-3 ps. For even shorter pulses, the increasing role of multiphoton

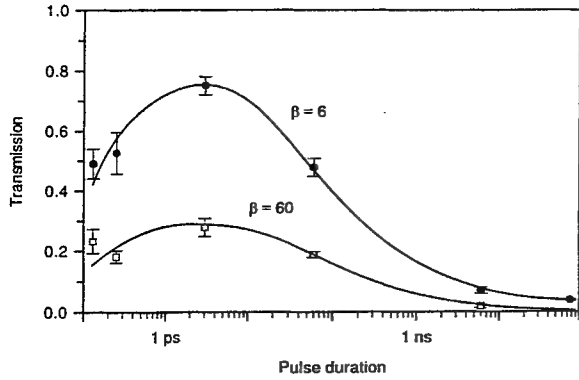


Figure 4: Plasma transmission as a function of laser pulse duration for $\beta = 6$ and $\beta = 60$. The measured data points¹⁸ are connected with lines to facilitate orientation.

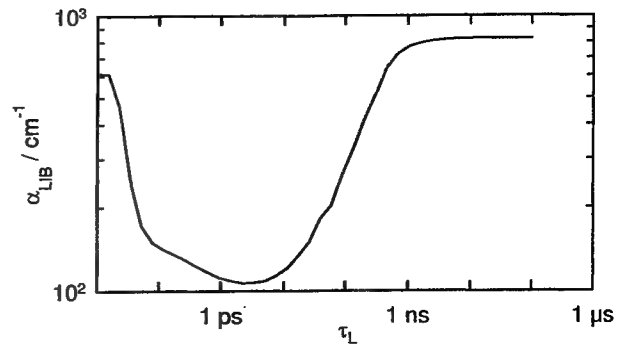


Figure 5: Calculated time averaged absorption coefficient α_{LIB} as a function of laser pulse duration τ_L ($\lambda = 580 \text{ nm}$, $2\omega_0 = 6 \mu\text{m}$).

absorption leads to an increasing electron density in the first half of the pulse (Fig. 2: 100 fs), so that again a larger fraction of the laser pulse energy is absorbed.

The qualitative behavior of the calculated absorption coefficient near threshold (Fig. 5) agrees well with the trends observed in the measured transmission data (Fig. 4): The transmitted energy shows only a weak dependence on pulse duration in the nanosecond range. With decreasing pulse duration experiments and calculations show an increase in transmission (a decrease in absorption). The measured transmission coincides with the predicted minimum of α_{LIB} at 2-3 ps, and the decreasing transmission for femtosecond pulses can be explained by the enhanced generation of free electrons during the first half of the laser pulse.

The absolute amount of the calculated absorption coefficients was found to be in good agreement with experimental data obtained from the measured transmission data T and plasma length l assuming the validity of Beers law ($\alpha = -\ln T / l$). It is interesting to note that the average absorption coefficient of laser-produced plasmas in water is for all pulse durations considerably smaller than the linear absorption coefficient of water at $\lambda = 3 \mu\text{m}$ ($\approx 17700 \text{ cm}^{-1}$)²⁵, or the linear absorption coefficient of corneal tissue at 193 nm ($\approx 40000 \text{ cm}^{-1}$)²⁶. This means that energy deposition based on linear absorption can, under certain conditions, be more localized than plasma-mediated energy deposition.

The pulse duration dependence of the absorption coefficient explains the trends in the $T(\tau_L)$ dependence, but alone it does not suffice to explain the large difference between the transmission of ns- and ps-plasmas (at $\beta = 6$ ns-plasmas transmit only $\approx 1/10$ of the light which passes through ps-plasmas, see Fig. 4). The second factor contributing to the low transmission of ns-plasmas is that they are longer than ps- and fs- plasmas at equal β and focusing angle (section 4). The difference in length is particularly pronounced near threshold. This is the reason why the transmission immediately drops to 50% once a ns- plasma is formed, but it only drops to 90-95% for ps- and fs-plasmas at threshold energies²¹.

6. MECHANICAL EFFECTS

6.1 Shock wave emission and cavitation

Table 2 gives an overview of how the mechanical effects created by LIB depend on the laser pulse duration. It summarizes the values of the shock wave pressure at the plasma rim and at 12 mm distance from the plasma, and presents the conversion efficiency of absorbed light energy into cavitation bubble energy. The shock wave emission in the vicinity of the plasma was investigated by streak photography with high spatial and temporal resolution (3 μm and <200 ps, respectively)^{18,27}. The pressure in the far-field was determined by hydrophone measurements¹⁸, and the cavitation bubble energy was obtained through a determination of the bubble size by acoustic means^{18,28}.

The data of Table 2 show that the mechanical effects accompanying breakdown decrease with decreasing pulse duration. This is true not only in absolute terms (due to the lower radiant energy threshold for breakdown), but also in relative terms: a smaller percentage of the incident light energy is converted into mechanical energy. This becomes most obvious by looking at the reduction of the conversion efficiency of light energy into cavitation bubble energy. It is,

pulse duration	$\beta = E/E_{th}$	pressure at plasma rim [GPa]	pressure at 12 mm distance [MPa]	conversion efficiency of absorbed light energy into cavitation bubble energy [%]
76 ns	6	10	4.0	22.0
6 ns	60	30	2.5	22.5
60 ps	60	10	0.65	13.5
3 ps	60	1.7	0.23	11.0
100 fs	60	1.0	0.06	3.0

Table 2: Dependence of shock wave pressure and cavitation on laser pulse duration¹⁸. The data for 76 ns pulses are given at $\beta = 6$ instead of $\beta = 60$ because of the limited laser pulse energy available.

furthermore, reflected in the decrease of the pressure at the plasma rim for shorter pulse durations. The smaller peak pressure indicates a smaller energy density deposited in the breakdown volume. The pulse duration dependence of the far-field pressure supports the above observations. It should be noted however, that the far-field pressure depends both on the pressure at the plasma rim and on the plasma size. The similarity law states that the shock pressure at a distance r from a source with radius r_0 depends only on the ratio r/r_0 , if the pressure inside the source is constant²⁹. Since, at equal β , the plasma radius r_0 decreases with decreasing laser pulse duration, the relative distance r/r_0 increases for $r = \text{constant}$. Thus a decreasing shock pressure at a fixed distance r would be expected for shorter laser pulses, even if the energy density in the plasma was independent of the pulse duration.

6.2 Energy density in the breakdown region

We estimated the average energy density in the breakdown region by comparing the absorbed energy with the breakdown volume deduced from photographs. With 6-ns-pulses at 1064 nm, energy densities of 30-40 kJcm⁻³ were reached which are far beyond the evaporation enthalpy of water and more than 6 times higher than the energy density in TNT³⁰. The high energy density in ns-plasmas explains the high conversion efficiency into cavitation bubble energy as well as the high shock wave pressures observed (Table 2). For 76-ns pulses, the maximum pressure in the plasma is limited by the fact that the plasma and bubble expansion start already during the laser pulse (see Fig 1a: the bubble is already quite large near the beam waist whereas its formation has just started further upstream), therefore the peak pressure is lower than after 6-ns pulses. With fs-pulses, the energy deposition is isochoric, but the average energy density in the breakdown region is only about 1 kJ cm⁻³¹⁸, i.e. lower than the evaporation enthalpy at constant pressure. The stress wave generation features therefore a stronger contribution of thermoelastic effects, and the peak pressure of the stress transients is much lower than with ns-pulses. Correspondingly, the conversion efficiency into bubble energy also drops to only 3%.

The high energy density in the ns- plasmas is associated with an easily visible plasma radiation, whereas the lower energy density in the fs-plasmas goes along with a lack of a visible plasma radiation: the occurrence of breakdown manifests itself merely by bubble formation at the laser focus. It should be noted, however, that the plasma radiation reflects mainly the electron temperatures and that there is little correlation to the average energy density in the sample

when the temperatures of the electrons and heavy particles are different, i. e. with ps- and fs-pulses. The different visibility of the plasma radiation is probably largely due to the change of its duration and size with different laser pulse durations, and not so much a consequence of a different intensity or of changes in its spectral characteristics.

The reduction of energy density in the plasma with decreasing pulse duration leads to a change of energy partition: whereas a smaller percentage of the incident light energy is converted into mechanical energy, a larger percentage is used for evaporation of the liquid within the breakdown volume²⁸. We found that the ratio $(E_{\text{mech}}/E_{\nu})$ at $\beta = 60$ is about 12.5:1 for 6-ns pulses and 0.25:1 for 100-fs pulses^{18,28}. Besides the reduction of the radiant energy threshold with decreasing pulse duration, this change of energy partition contributes largely to a less disruptive character of fs-breakdown.

6.3. Possible explanations for the pulse duration dependence of energy density

While most physical mechanisms involved in optical breakdown are linked to the irradiance of the laser light, the radiant energy required for breakdown and the resulting energy density in the interaction volume are of more practical interest. The change of the radiant energy threshold with decreasing pulse duration and the change of the average energy density in the plasma are closely linked, but not exactly the same: they are equivalent only, if the size of the interaction volume and the plasma absorption are equal. In the following, we shall discuss possible factors influencing the pulse duration dependence of the energy density.

Maximum electron density. The energy density in the plasma volume will decrease with pulse duration, if the maximum concentration of free electrons reached during the laser pulse is smaller for shorter pulse durations. This possibility has been suggested by Kennedy et al.³¹, who assume that ρ_{cr} is 10^{20} cm^{-3} for ns- and 60-ps plasmas, but 10^{18} cm^{-3} for 3-ps and fs-plasmas. It has, however, not yet been further investigated to date; measurement data of the free electron concentration after optical breakdown in water are only available for 30-ns plasmas, where Barnes and Rieckhoff¹⁹ found $\rho \approx 10^{20} \text{ cm}^{-3}$ at pulse energies well above threshold. Our threshold calculations presented in section 3 yielded good agreement with experimental values under the assumption of a constant value $\rho_{\text{cr}} = 10^{20} \text{ cm}^{-3}$ for all pulse durations. It is unlikely that ρ_{cr} largely exceeds 10^{21} cm^{-3} at any pulse duration because this is, for $\lambda = 1064 \text{ nm}$, the critical plasma density above which a major part of the incident laser light will be reflected. At ultrashort pulse durations, where the whole energy at the end of the laser pulse is stored in the form of free electrons and hardly any energy has been transferred to the heavy particles, it is also unlikely that ρ_{cr} is much less than 10^{21} cm^{-3} . The energy of 6.5 eV required to produce a quasi-free electron in water³² corresponds to $E = 1.04 \cdot 10^{-18} \text{ J}$. An electron density of $\rho = 2.5 \times 10^{21} \text{ cm}^{-3}$ therefore corresponds to an energy density of 2.5 kJ cm^{-3} , (if the free electrons do not have very much kinetic energy), equal to the evaporation enthalpy of water at room temperature. This means that ρ_{cr} must be $2.5 \times 10^{21} \text{ cm}^{-3}$ to produce a pure vapor bubble. If thermoelastic effects take part in the generation of the bubbles produced by ultrashort laser pulses, ρ_{cr} may be smaller, but certainly not by several orders of magnitude³³. For ns-pulses, the evaporation enthalpy can be exceeded with maximum electron concentrations below 10^{21} cm^{-3} because of the energy transfer from electrons to heavy particles during the pulse through recombination.

Energy distribution between electrons and heavy particles. The energy density in the plasma changes, even if the maximum concentration of free electrons is the same for all pulse durations: with long pulses, a temperature equilibrium between electrons and heavy particles is achieved during the pulse through recombination processes, and therefore the energy density is high. With ultrashort pulses, however, very little energy has at the end of the laser pulse been transferred to the heavy particles. An equilibrium temperature develops only after the laser pulse, and the equilibrium temperature will thus be much lower than in the case of the ns-pulses¹².

Average temperature of electrons and heavy particles. With ns- and ps-pulses at superthreshold energies, the plasma grows towards the incoming laser beam during the first part of the laser pulse and is heated during the second half of the pulse, particularly at the upstream side of the plasma^{11,34,35}. This heating results in an increase of the average temperature of the electrons and heavy particles. It is evidently most pronounced with long pulse durations where the amount of surplus energy deposited in the plasma is largest. At 76 ns, however, the increase of the energy density is counteracted by the expansion of the plasma during the laser pulse.

Plasma size. With ns-pulses, the breakdown threshold decreases during the laser pulse due to the UV-radiation emitted by recombining free electrons and bremsstrahlung (see section 4). This leads to an increase of the plasma size and thus to a reduction of the average energy density within the plasma.

Sharpness of plasma boundaries. After fs-breakdown, heating of the liquid is observed in front of the actual breakdown zone where a bubble is produced, particularly for large β -values (Figure 6). Similar observations have not been made for ns- or ps-pulses. This means that in fs-breakdown a larger part of the absorbed energy cannot be converted into bubble energy than with the longer pulse durations. The reason for this phenomenon is probably that a large number of free electrons is produced by MPI even in regions where ρ_{cr} is not completely reached (in Figure 2 the corresponding feature is that a large number of free electrons is already present at the beginning of the 100 fs laser pulse).

We can conclude that there are several factors influencing the pulse duration dependence of energy density within the breakdown volume which are partly opposing each other. The most important factor setting the general trend seems to be the energy distribution between electrons and heavy particles at the end of the laser pulse.

7. SELF FOCUSING

In the previous sections we have, for the sake of simplicity, neglected that all aspects of the breakdown process with ultrashort laser pulses are actually modified by self focusing. For self focusing leading to beam collapse to occur with a Gaussian beam, a critical power³⁶

$$P_{cr} = 3.77 \frac{c \lambda^2}{32 \pi^2 n_2} \quad (3)$$

has to be surpassed, where n_2 is the value of the nonlinear refractive index. Since the irradiance and power thresholds for optical breakdown increase when the pulse duration is reduced, the role of self-focusing becomes ever more important.

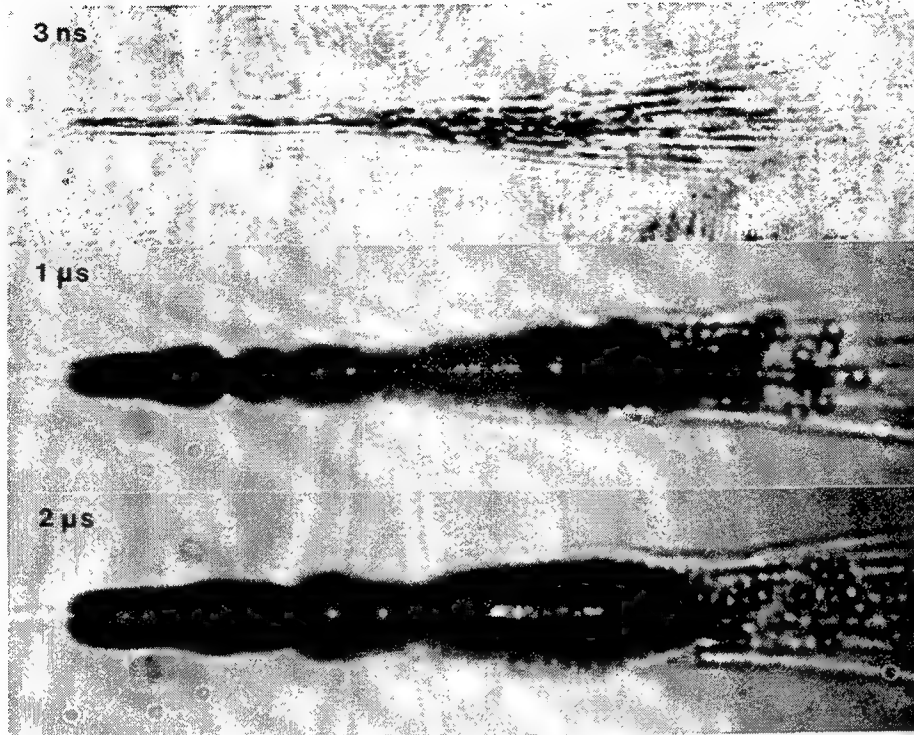


Figure 6: Optical breakdown region after a 100 fs pulse with 35 μ J pulse energy ($\beta = 200$), photographed at different times after breakdown. The photographs taken 1 and 2 μ s after breakdown are slightly defocused to visualize the zones of elevated temperature outside the cavitation bubble. The laser light was incident from the right, the bar represents a length of 100 μ m.

Self-focusing will

- diminish the energy threshold E_{50} for breakdown, because it reduces the cross section of the laser beam,
- produce an elongated breakdown region, because it causes the location of the focus to move during the laser pulse leaving a trace which looks like a filament^{37,38},
- change the energy distribution in the breakdown region, because the region splits into the part of the "filament" and a "shoulder" ^{11,36,38}. In the shoulder, the energy density in the plasma is reduced, or the irradiance may even stay below the breakdown threshold, and
- increase the light transmission through the breakdown region²¹, because the absorption coefficient is smaller in the shoulder region, which contains a fairly large part of the laser light energy^{36,38}.

Theoretical predictions of the self-focusing thresholds for ultrashort laser pulses face some difficulties: The n_2 -values are probably smaller than those measured for longer pulses, because the laser pulses are now shorter than the time constant of the molecular Kerr effect which is the predominant mechanism responsible for the refractive index change with ns-and ps pulses^{39,40}. With fs-pulses, the electronic Kerr effect should gain relative importance. This change and the n_2 -values for fs-pulses have, however, not yet been investigated in detail. Furthermore, self focusing is modified by group velocity dispersion which can be neglected at longer pulse durations^{15,41}.

Experimental evidence indicates that with 6-ns-pulses, self focusing plays a role at threshold energies only for very small focusing angles $< 2^\circ$ and at infrared wavelengths where, due to the lower rate of MPI, the required breakdown power

is higher than at visible wavelengths¹¹. With 30-ps pulses of 1064 nm wavelength, self focusing is also observed at larger focusing angles as used in ocular surgery, but only at energies far above the breakdown threshold¹¹. With fs-pulses, self focusing plays a role for all focusing angles even at threshold and in the visible wavelength range¹⁵. We could identify the occurrence of self-focusing effects with fs pulses through

- the change of the shape of the breakdown region observed in Figs. 6 and 1d in comparison to Figs. 1a - c, and by
- the observation of continuum generation at all energies $E \geq E_{50}$. Continuum generation is like self-focusing a self-phase modulation effect³⁹, and in water it is known to occur always at powers above the threshold for self-focusing⁴².

8. CLINICAL CONSIDERATIONS

The radiant exposure threshold F_{50} for fs-breakdown at tissue surfaces and the ablation rate at threshold^{3,4} are similar to the characteristic parameters of ablation using excimer laser pulses at 193 nm wavelength⁴³, and not very different from those of Q-switched IR-laser ablation with wavelengths near 3 μm ⁴⁴. This means that plasma-mediated surface ablation - even with ultrashort laser pulses - has no fundamental advantage as compared to ablation based on linear absorption. Apparently, it has also little advantage as compared to plasma-mediated ablation with ps-pulses: Stern et al.⁴⁵ who investigated plasma-mediated corneal ablation with pulse durations between 8 ns and 65 fs found that the amount of tissue damage produced by 30-ps pulses at 50 μJ was so slight that no additional improvements in excision ultrastructure resulted when shorter pulses at even lower pulse energies were used (at a tissue surface, the plasma is not confined, and its expansion produces therefore little disruptive effects). The situation is completely different, when the application site is located *within* a tissue as, for example, the eye. A noninvasive, localized energy deposition inside the eye can only be achieved through nonlinear absorption of light which at low intensities penetrates the tissue. The reduced ablation threshold of ultrashort laser pulses can also be of advantage, because the plasma confinement leads to much stronger mechanical effects than at surfaces.

Evaporation of the tissue within the plasma volume is the primary tissue effect at all pulse durations⁴⁶, but the degree of collateral mechanical effects varies with pulse duration. Nanosecond breakdown features a very high efficacy of energy deposition (Fig. 4), and a very high conversion rate of light energy into mechanical energy (up to 90%²⁸). It is, hence, well suited where disruptive effects are desired. Ultrashort laser pulses have a lower energy threshold for breakdown than ns-pulses (F_{50} drops by a factor of ≈ 160 when the pulse duration is reduced from 6 ns-to 100 fs, see Table 1), a lower efficacy of energy deposition (Fig. 4), and a lower conversion rate into mechanical effects (Table 2, and Ref. 28). As a consequence, evaporation is more important, and the tissue effects are much less disruptive. Ultrashort pulses allow therefore the generation of much finer effects than can be achieved with ns-pulses.

Ultrashort laser pulses are advantageous where precise cuts with little collateral damage are desired, as in laser-keratomileusis, or in the preparation of a flap for LASIK^{47,48}. For many tasks in intraocular microsurgery, however, the laser effects need not be so fine as possible with femtosecond laser pulses. In these cases, the use of ns-pulses may even be advantageous as, for example, in posterior capsulotomy. Capsulotomy with ps- or fs- pulses requires the application of

pulse series with a large number of pulses to produce several long cuts of different directions in the lens capsule. This technique requires a fairly large amount of laser energy and is relatively time consuming. The cuts imply, furthermore, a larger risk of producing damage at the curved surface of the intraocular lens than the application ns pulses, because in the latter case a few individually aimed pulses suffice to achieve the surgical aim. The ns-pulses are, hence advantageous for capsulotomies just *because* of their disruptive character⁴⁷.

The intraocular application of fs-pulses is complicated by self-focusing, particularly when the application site is located deeply inside the eye. In this case, the localizability the laser effects will suffer from an elongation of the breakdown region (Liu et al.⁶ report, for example, that threshold effects in silica with a diameter of only 1 μm had a length of 10-15 μm , and Figs. 1d and 6 show a strongly elongated breakdown region at energies well above threshold). Laser applications in the cornea as in laser keratomileusis will, in contrast, hardly be influenced by self-focusing, because the propagation distance through the nonlinear medium is very short.

9. ACKNOWLEDGEMENTS

We appreciate stimulating discussions of LIB thresholds with Dr. Paul Kennedy. The work was supported by the German Research Foundation (#Bi321/2-4), the United States Air Force Office of Scientific Research (#2312AA92AL014), and TASC (#J06829S95135).

10. REFERENCES

1. A. Vogel, "Nonlinear absorption: intraocular microsurgery and laser lithotripsy", *Phys. Med. Biol.* **42**, pp. 895-912, 1997.
2. P.K. Kennedy, D. X. Hammer, B. A. Rockwell, "Laser-induced breakdown in aqueous media", *Progr. Quant. Electron.* **21**, pp. 155-248, 1997.
3. A. A. Oraevsky, L. B. DaSilva, A. M. Rubenchik, M. D. Feit, M. E. Glinsky, M. D. Perry, B. M. Mammini, W. Small IV, and B. C. Stuart, "Plasma-mediated ablation of biological tissues with nanosecond-to-femtosecond laser pulses: Relative role of linear and nonlinear absorption", *IEEE J. Selected Topics Quantum Electron.* **2**(4), pp. 801-809, 1996.
4. J. Neev, L.B Da Silva, M. D. Feit, M. D. Perry, A. M. Rubenchik, and B. C. Stuart, "Ultrashort pulse lasers for hard tissue ablation", *IEEE J. Selected Topics Quantum Electron.* **2**(4), pp. 790-800, 1996.
5. R. F. Steinert and C. A. Puliafito, "The Nd:YAG Laser in Ophthalmology", Saunders, Philadelphia, PA, 1985.
6. X. Liu, D. Du, and G. Mourou, "Laser ablation and micromachining with ultrashort laser pulses", *IEEE J. Quantum Electron.* **33**, pp. 1706-1716, 1997.
7. F. Docchio, L. Dossi, C. A. Sacchi "Q-switched Nd:YAG laser irradiation of the eye and related phenomena: An experimental study I - Optical breakdown determination for liquids and membranes", *Lasers Life Sci.* **1**, pp. 87-103, 1986.
8. A. Vogel, M.R.C. Capon, M. N. Asiy-Vogel, R. Birngruber, "Intraocular photodisruption with picosecond and nanosecond laser pulses: Tissue effects in cornea, lens and retina", *Invest. Ophthalmol. Vis. Sci.* **35**, pp. 3033-3044, 1994
9. N. Bloembergen, "Laser-induced breakdown in solids", *IEEE J. Quantum Electron.* **10**, pp. 375-386, 1974.
10. P. A. Barnes and K. E. Rieckhoff, "Laser induced underwater sparks", *Appl. Phys. Lett.* **13**, pp. 282-284.
11. A. Vogel, K. Nahen, D. Theisen, J. Noack, "Plasma formation in water by picosecond and nanosecond Nd:YAG laser pulses- part I: optical breakdown at threshold and superthreshold irradiance", *IEEE J. Selected Topics Quantum Electron.* **2**(4), pp. 847-860, 1996
12. B. N. Chichkov, C. Momma, S. Nolte, F. von Alvensleben, and A. Tünnermann, "Femtosecond, picosecond and nanosecond ablation of solids", *Appl. Phys. A* **63**, pp. 109-115, 1996.

13. P. K. Kennedy, "A first-order model for computation of laser-induced breakdown thresholds in ocular and aqueous media: Part I-Theory", *IEEE J. Quantum Electron.* **31**, pp. 2241-2249, 1995.

14. M. H. Niemz, "Threshold dependence of laser-induced optical breakdown on pulse duration", *Appl. Phys. Lett.* **66**, pp. 1181-1183.

15. Q. Feng, J. V. Moloney, A. C. Newell, E. M. Wright, K. Cook, P. K. Kennedy, D. X. Hammer, B. A. Rockwell, C. R. Thomson, "Theory and simulation on the threshold of water breakdown induced by ultrashort laser pulses", *IEEE J. Quantum Electron.* **33**, pp. 127-137, 1997.

16. J. Noack, A. Vogel, D. X. Hammer, G. D. Noojin, B. A. Rockwell, "Thresholds and transmission of laser-induced breakdown in water for pulse durations between 100 fs and 100 ns", *submitted to Appl. Phys. Lett.* 1998.

17. F. Docchio, "Lifetimes of plasmas induced in liquids and ocular media by single Nd:YAG pulses of different duration", *Europhys. Lett.* **6**, pp. 407-412, 1988.

18. J. Noack, "Optical breakdown in water with laser pulses between 100 ns and 100 fs", *PhD Dissertation*, Medical University of Lübeck, Lübeck, Germany 1998 (in German).

19. This is surprising at first sight, because Fig. 3 shows that $\rho(t)$ is strongly influenced by recombination. However, when recombination is neglected, the breakdown threshold in the ns-range is determined by the threshold for MPI generation of the initial electrons. Due to the strong intensity dependence of η_{mp} , slight variations of I are already sufficient to compensate for a reduction of the pulse duration. This also leads to a similar shape of the $I_{50}(\tau_L)$ curve as in Fig. 3 (see Ref. 2).

20. F. Docchio, P. Regondi, M.R.C. Capon, J. Mellerio, "Study of the temporal and spatial dynamics of plasmas induced in liquids by nanosecond Nd:YAG laser pulses. 1: Analysis of the plasma starting times", *Appl. Opt.* **27**, pp. 3661-3668, 1988.

21. K. Nahen and A. Vogel, "Plasma formation in water by picosecond and nanosecond Nd:YAG laser pulses - Part II: Plasma transmission, scattering and reflection", *IEEE J. Selected Topics Quantum Electron.* **2**(4), pp. 861-871, 1996.

22. D. X. Hammer, E. D. Jansen, M. Frenz, G. D. Noojin, R. J. Thomas, J. Noack, A. Vogel, B. A. Rockwell, A. J. Welch, "Shielding properties of laser-induced breakdown in water for pulse durations from 5 ns to 125 fs", *Appl. Opt.* **36**, pp. 5630-5640, 1997.

23. R. P. Godwin, C. G. M. van Kessel, J. N. Olsen, P. Sachsenmaier, R. Sigel, "Reflection losses from laser-produced plasmas", *Z. Naturforsch.* **32a**, pp. 1100-1107, 1977.

24. M. D. Feit, J. A. Fleck, "Effect of refraction on spot size dependence of laser-induced breakdown", *Appl. Phys. Lett.* **24**, pp. 169-172, 1974.

25. E. F. Maher, "Transmission and absorption coefficients for ocular media of the rhesus monkey. Report SAM-TR-78-32, USAF School of Aerospace Medicine, Brooks Airforce Base, Texas, USA, 1978.

26. G. H. Pettit, M. N. Ediger, "Corneal absorption coefficients for 193 nm and 213-nm ultraviolet radiation", *Appl. Opt.* **35**, pp. 3386-3391, 1996.

27. J. Noack, A. Vogel, "Single-shot spatially resolved characterization of laser-induced shock waves in water", *submitted to Appl. Opt.*, 1997

28. A. Vogel, J. Noack, K. Nahen, D. Theisen, S. Busch, U. Parlitz, D. X. Hammer, G. D. Noojin, B. A. Rockwell, R. Birngruber, "Energy balance of optical breakdown in water", *SPIE Proc.* **3254A**, 1998 (in print).

29. R. H. Cole, "Underwater Explosions", Princeton University Press, Princeton, NJ, 1948.

30. A. Vogel, S. Busch, U. Parlitz, "Shock wave emission and cavitation bubble generation by picosecond and nanosecond optical breakdown in water", *J. Acoust. Soc. Am.* **100**, pp. 148-165, 1996.

31. P. K. Kennedy, S. A. Boppart, D. X. Hammer, B. A. Rockwell, G. D. Noojin, W. P. Roach, "A first order model of laser-induced breakdown thresholds in ocular and aqueous media: Part II- comparison to experiments", *IEEE J. Quantum Electron.* **31**, pp.2250-2257, 1995.

32. F. Williams S. P. Varama, S. Hillenius, "Liquid water as a lone-pair amorphous semiconductor", *J. Chem Phys.* **64**, pp. 1549-1554, 1976.

33. Kennedy et al.^{2,13} obtained similarly high irradiance thresholds for ultrashort laser pulses as in the present study although they used $\rho_{cr} = 10^{18} \text{ cm}^{-3}$ for $\tau_L \leq 3 \text{ p}$ in their calculations instead of $\rho_{cr} = 10^{20} \text{ cm}^{-3}$. The similarity of the results is probably due to the fact that they assumed MPI to act only during 1/10 of the laser pulse duration, whereas in the present study the effect of MPI throughout the whole laser pulse duration was considered.

34. F. Docchio, P. Regondi, M.R.C. Capon, J. Mellerio, "Study of the temporal and spatial dynamics of plasmas induced in liquids by nanosecond Nd:YAG laser pulses. 2: Plasma luminescence and shielding", *Appl. Opt.* **27**, pp. 3669-3674, 1988.

35. J. Noack, D. X. Hammer, G. D. Noojin, B. A. Rockwell, A. Vogel, "Influence of pulse duration on mechanical effects after laser-induced breakdown in water", *submitted to J. Appl. Phys.* 1997.

36. J. H. Marburger, "Self-focusing: Theory", *Progr. Quantum Electron.* 4:35-110, 1975.

37. M. T. Loy, Y. R. Shen, "Study of self-focusing and small-scale filaments of light", *IEEE J. Quantum Electron.* 9, pp. 409-422, 1973.

38. A. Brodeur, C. Y. Chien, F. A. Ilkov, S. L. Chin, O. G. Kosareva, V. P. Kandidov, "Moving focus in the propagation of ultrashort laser pulses in air", *Opt. Lett.* 22, pp. 304-306, 1997.

39. Y. R. Shen, G. Z. Yang, "Theory of self-phase modulation and spectral broadening, in: R. R. Alfano, Ed., *The Supercontinuum Laser Source* (Springer, New York), pp. 1-32, 1989.

40. Q. Z. Wang, P. P. Ho, R. R. Alfano, "Supercontinuum generation in condensed matter, in: R. R. Alfano, Ed., *The Supercontinuum Laser Source* (Springer, New York), pp. 33-90, 1989.

41. G. Fibich, "Femtosecond laser tissue interactions", *SPIE Proc.* 2673, pp. 93-101, 1996.

42. W. L. Smith, P. Liu, N. Bloembergen, "Superbroadening in H₂O and D₂O by self-focused picosecond pulses from a YAlG:Nd laser", *Phys. Rev. A* 15, pp. 2396-2403, 1977.

43. G. H. Pettit, M. N. Ediger, R. P. Weiblanger, "Excimer laser ablation of the cornea", *Opt. Eng.* 34, pp. 661-667, 1995.

44. D. Stern, C. A. Puliafito, E. T. Tobi, W. T. Reidy, "Infrared laser surgery of the cornea. Studies with a Raman-shifted Neodymium:YAG laser at 2.80 and 2.92 μm ", *Ophthalmology* 95, pp. 1434-1441, 1988.

45. D. Stern, R. W. Schoenlein, C. A. Puliafito, E. T. Dobi, R. Birngruber, J. G. Fujimoto, "Corneal ablation by nanosecond, picosecond, and femtosecond lasers at 532 and 625 nm", *Arch. Ophthalmol.* 107, pp. 587-592, 1989.

46. A. Vogel, P. Schweiger, A. Frieser, M. N. Asayo, R. Birngruber, "Intraocular laser surgery: Light-tissue interaction, damage range, and reduction of collateral effects", *IEEE J. Quantum Electron.* 26, pp. 2240-2260, 1990.

47. T. Juhasz, personal communication. See also X. Liu, G. Mourou, "Ultrashort laser pulses tackle precision machining", *Laser Focus World*, August 1997, p. 118.

48. A. Vogel, T. Günther, M. N. Asayo-Vogel, R. Birngruber, "Factors determining the refractive effects of intrastromal photorefractive keratectomy with the picosecond laser", *J. Cataract Refract. Surg.* 23, pp. 1301-1310, 1997.

49. G. Geerling, J. Roider, U. Schmidt-Erfurth, K. Nahen, E.-S. El-Hifnawi, H. Laqua, A. Vogel, "Initial clinical experience with the picosecond Nd:YLF laser for intraocular therapeutic applications", *Brit. J. Ophthalmol.* 1998 (in print).

50. B. C. Stuart, M. D. Feit, S. Hermann, A. M. Rubenchik, B. W. Shore, M. D. Perry, "Nanosecond to femtosecond laser-induced breakdown in dielectrics", *Phys. Rev. B* 53, pp. 1749-1761, 1996.

Retinal damage mechanisms from ultrashort laser exposure

B.A. Rockwell, D.J. Payne, R.A. Hopkins, D.X. Hammer, P.K. Kennedy,
R.E. Amnote, B. Eilert, J.J. Druessel, C.A. Toth*, W.P. Roach*,
S.L. Phillips†, D.J. Stolarski*, G.D. Noojin*, R.J. Thomas*, and C.P. Cain*

Air Force Research Laboratory, Human Effectiveness Directorate, Directed Energy Bioeffects Division,
Optical Radiation Branch, 8111 18th Street, Brooks AFB, TX, 78235-5215

*Duke University Eye Center, P.O. Box 3802, Durham, NC 27710

†Air Force Office of Scientific Research, AFOSR/NL, 110 Duncan Ave, Bolling AFB, DC 20332

‡Air Force Armstrong Laboratory, AL/OEV, 2509 Kennedy Circle, Brooks AFB, TX, 78235-5118

§TASC, 4241 Woodcock Dr., Suite B-100, San Antonio, TX, 78228-1330

ABSTRACT

Extensive research of ultrashort ocular damage mechanisms has shown that less energy is required for retinal damage for pulses shorter than one nanosecond. Laser minimum visible lesion (MVL) thresholds for retinal damage from ultrashort (i.e. < 1 ns) laser pulses occur at lower energies than in the nanosecond (ns) to microsecond (μs) laser pulse regime. We review the progress made in determining the trends in retinal damage from laser pulses of one nanosecond to one hundred femtoseconds in the visible and near-infrared wavelength regimes. We discuss the most likely damage mechanism(s) operative in this pulse width regime and discuss implications on laser safety standards.

Keywords: eye, safety, laser, nonlinear optics, retinal damage

1. INTRODUCTION

Several enabling laser technologies are allowing the proliferation of ultrashort laser systems in the visible (VIS) and near infrared (NIR) spectral regions (i.e. the retinal hazard regime). These wavelengths easily propagate through the eye and can result in retinal damage and functional vision loss if proper laser protective measures are not employed. Unfortunately, there exists no current maximum permissible exposure limit based on biological data for pulses shorter than 1 ns in duration. In recent works by Cain, et al.^{1,2,3} MVL threshold data for ultrashort single laser pulses show a decrease in the amount of pulse energy needed to cause observable retinal damage below 1 ns. Also, laser induced breakdown (LIB), self-focusing (SF), supercontinuum generation (SC) and stimulated Brillouin scattering (SBS) have been studied⁴ to determine their influence on retinal damage thresholds.

In this paper we review the measured thresholds for minimum visible lesion (MVL) and for nonlinear optical phenomena considered in previous studies and the recent studies of melanin mediated damage. We will consider visible and near infrared MVL studies and their impact on determining new damage mechanisms. A review of all the MVL literature from the past couple of decades indicates that the single-pulse MVL data exhibits three broad trends (see Figure 1). For exposures longer than 20 μs there is a region where near constant irradiance

(W/cm²) is required for retinal damage. For pulses from 1 ns to 20 μ s, diffusion of heat is negligible during the exposure and the fluence (J/cm²) required for retinal damage is nearly constant. The third regime occurs for pulse durations shorter than one nanosecond where the data shows that it takes less energy to create retinal damage than for longer pulses. We will discuss the region of retinal damage for pulse durations below one nanosecond.

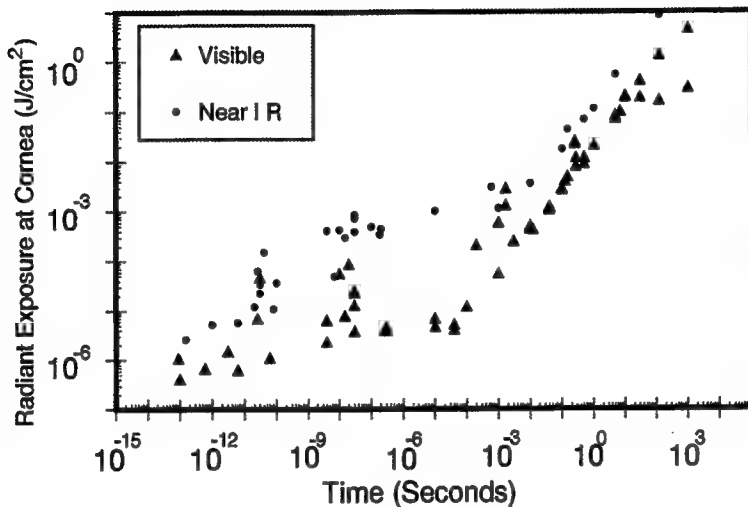


Figure 1. MVL data collected during the previous thirty years. The data shows three trends as discussed in the text.

2. ULTRASHORT LASER PULSE RETINAL DAMAGE

We have published several studies on measurements of the MVL threshold for both the visible⁵ and near-infrared⁶ spectral regimes. Figure 1 shows our measured thresholds, which are included with data from many other groups over the past thirty years. Our experiments provide the majority of data for pulsewidths below one nanosecond, and concur with most of the sub-nanosecond data points taken by other researchers.

When considering ultrashort retinal damage several phenomena should be considered that might influence the threshold or type of damage seen for these short pulses (see Figure 2). Because ultrashort laser pulses can possess significant peak powers and irradiance, nonlinear propagation effects need to be considered⁴. For all pulse durations above one nanosecond, the propagation of laser light to the retina can be considered linear and the spot size can be calculated from the wavelength, aberrations and laser divergence. For ultrashort laser pulses, the retinal fluence and wavelength can be different than that resulting from linear propagation. We have reported the thresholds measured for several nonlinear optical phenomena⁷, which are shown in Figure 3.

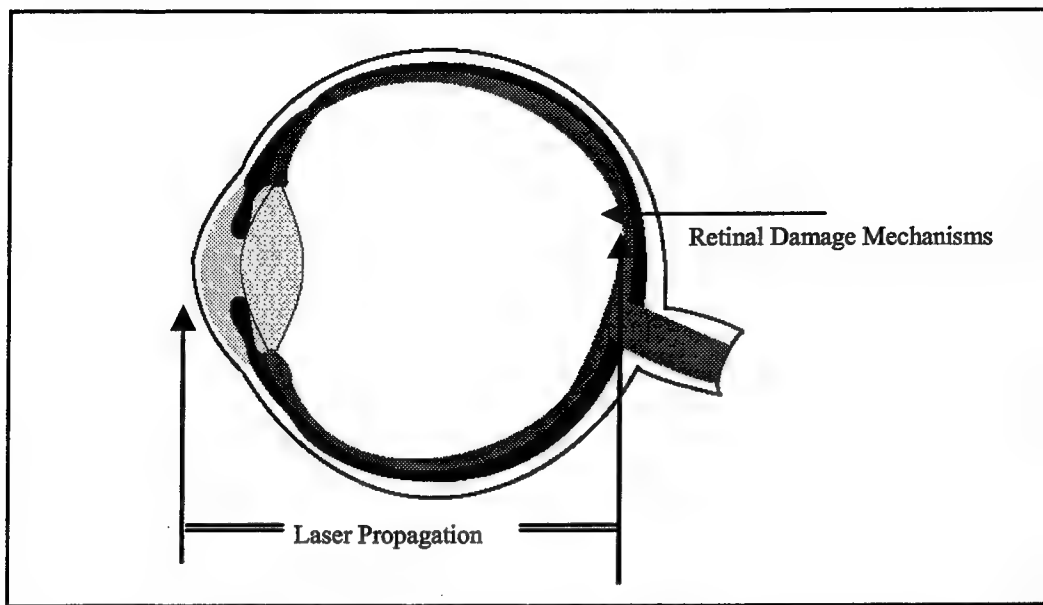


Figure 2. This figure highlights the need to consider both propagation and laser tissue interaction phenomena for ultrashort laser retinal damage. For pulses with significant peak irradiance, laser propagation effects should be considered to determine the retinal spot characteristics.

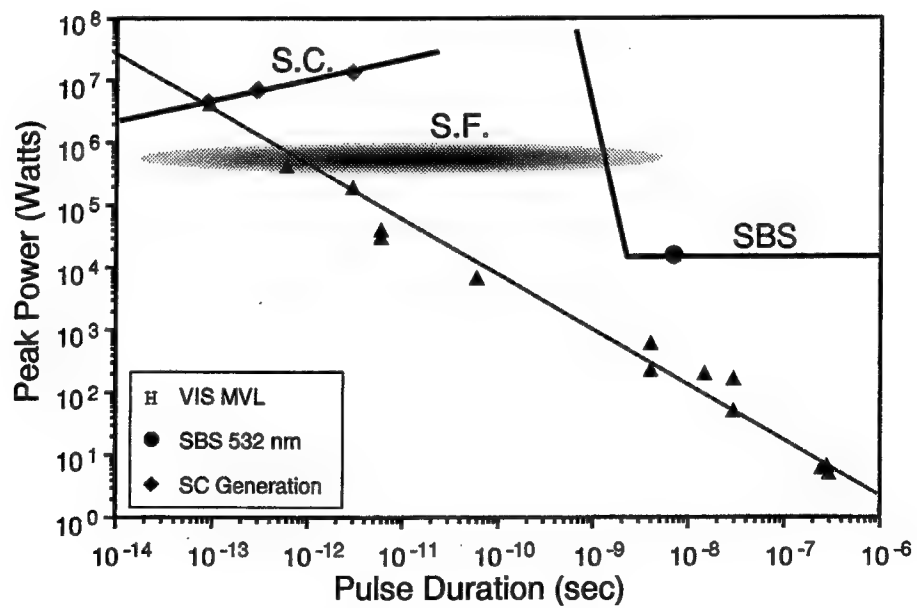


Figure 3. Plotted is the peak power for MVL data (triangles) with an outline of the peak power measured for various nonlinear optical effects in the geometry of the eye (circle and diamond).

We have developed an artificial eye¹⁰ to measure nonlinear phenomena. In Figure 3 the measured thresholds for SBS¹⁰, SF¹¹ and SC¹⁰ are shown as measured in our artificial eye. Because the threshold is well above the MVL threshold SBS is not expected to play a role in changing the MVL threshold. Self-focusing is known to change the spot size in certain geometries. Irradiance enhancement was shown to occur above 0.5 MW of peak power in the geometry of the artificial eye¹¹. As a result of the measured MVL thresholds, self-focusing is not expected to significantly affect the MVL threshold above several (tens of) picoseconds. Below this, self-focusing could affect the retinal spot size. Well below several hundred femtoseconds in pulse duration additional phenomena like wavelength dispersion would also influence the eventual beam characteristics. Supercontinuum generation is seen to occur nominally near the MVL level for visible wavelengths at the shortest pulselengths. At threshold, SC shows a bandwidth of ten nanometers or so, and probably would not affect the MVL level. At higher energy levels, SC can produce wavelengths from UV to IR light as the pulse broadens spectrally. This deposition of UV on the retina could cause interesting retinal effects, but the effect of these short wavelengths on the retina have not been studied.

The thresholds for laser induced breakdown in the artificial eye have been measured^{9,10} and compared for several different focusing geometries. We have also measured the threshold for LIB creation in-vivo^{2,3,8} through the use of video imaging. Through these investigations, we have found that LIB is a MVL-threshold-level damage mechanism for 100 fs visible pulses, but occurs at superthreshold levels for longer pulse durations.

As displayed in Figure 2, laser interaction with the retina plays an important role in determining the threshold for damage. For ultrashort pulses, stress confinement in retinal melanin⁸ has been hypothesized to account for the dropping MVL threshold. This view is different than the trend seen in skin melanin, where the threshold for immediate dermal whitening was shown to be nearly independent of pulse width¹¹ for pulse durations between 65 fs and 40 ns. In collaboration with Charles Lin and his team at Wellman Laboratories, we are presently doing experiments to determine the effect of smaller spot sizes on retinal melanin disruption and the ultimate damage response of retinal tissues. We are reporting in this year's Laser-Tissue Interaction IX the thresholds for damaging an artificial retina in an artificial eye using both visible and near-infrared femtosecond to nanosecond pulses¹⁴. It is expected that the interplay between the propagation and tissue interaction issues will be critical in explaining the drop in MVL threshold for ultrashort pulses.

3. SUMMARY

Self-focusing, LIB and melanin-mediated effects are proposed as possible factors affecting sub-nanosecond MVL thresholds. Most of the previous research has not considered the chromatic aberration in the eye where NIR light is focused behind the absorbing layer of the eye (i.e. the retinal pigmented epithelial layer). To extend these arguments into the NIR, one needs to consider that light at NIR wavelengths focus behind the retina¹⁵. As reported by Cain et al.⁵, the NIR MVL data follow a more dramatic trend than that seen in the visible MVL's. The relevant mechanism(s) responsible for lowering the MVL threshold will also need to explain the enhanced drop for the NIR wavelength regime.

There are numerous implications for laser safety from this work. The drop in MVL's below one nanosecond suggests that the current constant-fluence laser safety standard¹⁶ (from one nanosecond to more than ten microseconds) is not appropriate for shorter pulselengths. There exists guidance in the current ANSI standard¹⁶ that recommends using a constant power below one nanosecond. Our data suggests that this is prohibitively conservative. We have suggested a more lenient standard for ultrashort laser pulses and expect that in the next

ANSI rewrite the maximum permissible exposure limits for ultrashort laser pulses will be changed to reflect our data and analysis.

The use of ultrashort laser pulses offers the possibility of unique solutions to industrial problems such as remote sensing, high precision LIDAR and laser welding. The increased interest in using ultrashort laser pulses highlights the current deficiencies in the national laser safety standard. Our work is intended to define the interplay between the nonlinear-optical and melanin-mediated effects that determine the eventual MVL threshold.

4. ACKNOWLEDGMENTS

This work was supported by the Air Force Office of Scientific Research (2312A103) and Armstrong Laboratory. This research was conducted while Dale Payne held an NRC-Armstrong Laboratory Postdoctoral Research Associateship.

5. REFERENCES

- 1 The animals involved in this study were procured, maintained, and used in accordance with the Federal Animal Welfare Act and the "Guide for the Care and Use of Laboratory Animals," prepared by the Institute of Laboratory Animal Resources - National Research Council.
- 2 C. P. Cain, C. D. DiCarlo, B. A. Rockwell, P. K. Kennedy, G. D. Noojin, D. J. Stolarski, D. X. Hammer, C. A. Toth, and W. P. Roach, *Retinal Damage and Laser-Induced Breakdown Produced by Ultrashort-Pulse Lasers*, Graefe's Archive for Clinical and Experimental Ophthalmology 234: suppl. 1, S28-S37 (1996).
- 3 C. P. Cain, C. D. DiCarlo, G. D. Noojin, R. E. Amnote, B. A. Rockwell and W. P. Roach, *In-Vivo Laser-induced Bubbles in the Primate Eye with Femtosecond Pulses*, in *Laser-Tissue Interaction VII*, Steven L. Jacques, Ed., Proc. SPIE 2681A, 382-388 (1996).
- 4 B.A. Rockwell, P.K. Kennedy, R.J. Thomas, W.P. Roach and M.E. Rogers, *The Effect of Nonlinear Optical Phenomena on Retinal Damage*, in *Laser-Tissue Interaction VI*, Steven L. Jacques, Editor, Proc. SPIE 2391, 89-99 (1995).
- 5 C. P. Cain, C. A. Toth, C. D. DiCarlo, C. D. Stein, G. D. Noojin, D. J. Stolarski, W. P. Roach. *Visible Retinal Lesions from Ultrashort Laser Pulses in the Primate Eye*, Investigative Ophthalmology and Visual Science 36, 879-888 (1995).
- 6 C. P. Cain, C. A. Toth, C. D. DiCarlo, G .D. Noojin, R. E. Amnote, V. Caruthers, and B .A. Rockwell, *Visible Lesion Thresholds from Near-Infrared Pico and Nanosecond Laser Pulses in the Primate Eye*, in *Laser-Tissue Interaction VIII*, Steven L. Jacques, Ed., Proc. SPIE Vol. 2975, 133-137, (1997).
- 7 Benjamin A. Rockwell, D.X. Hammer, R.A. Hopkins, D.J. Payne, C.A. Toth, W.P. Roach, J.J. Druessel, P.K. Kennedy, R.E. Amnote, B. Eilert, S. Phillips, G.D. Noojin, D.J. Stolarski and C. Cain, *Ultrashort Laser Pulse Bioeffects and Safety*, Proceedings of the International Laser Safety Conference 3, 159-165 (1997).
- 8 C.P. Cain, C.A. Toth, C.D. Stein, G.D. Noojin, D.J. Stolarski, B.A. Rockwell, S.A. Boppart and W.P. Roach, *Femtosecond laser threshold: retinal damage versus induced breakdown mechanisms*, in Laser-Tissue Interaction V, Steven L. Jacques, Ed., Proc. SPIE 2134A, 22-27 (1994).
- 9 D. X. Hammer, R. J. Thomas, G. D. Noojin, B. A. Rockwell, P. K. Kennedy, and W. P., Roach, *Experimental Investigation of Ultrashort Pulse Laser-Induced Breakdown Thresholds in Aqueous Media*, IEEE Jour. Quant. Electronr. 32, 670-678 (1996).

10 C.P. Cain, G.D. Noojin, D.X. Hammer, R.J. Thomas and B.A. Rockwell, *Artificial Eye for In-vitro Experiments of Laser Light Interaction with Aqueous Media*, Jour. Biomedical Optics 2, 88-94 (1997).

11 Hammer, D.X., G.D. Noojin, R.J. Thomas, R.A. Hopkins, P.K. Kennedy, J.J. Druessel, B.A. Rockwell, A.J. Welch, and C.P. Cain, Measurement Of The Self-Focusing Threshold In Aqueous Media By Ultrashort Laser Pulses, in Laser-Tissue Interaction VIII, Steven L. Jacques, Ed., Proc. SPIE Vol. 2975, 163-172, (1997).

12 S. Jacques, A.A. Oraevsky, R. Thompson and B.S. Gerstman, *A working theory and experiments on photomechanical disruption of melanosomes to explain the threshold for minimal visible retinal lesions for sub-ns laser pulses*, in Laser-Tissue Interaction V, Steven L. Jacques, Ed., Proc. SPIE 2134A, 54-65 (1994).

13 S. Watanabe, R.R. Anderson, S. Brorson, G. Dalickas, J.G. Fujimoto and T.J. Flotte, *Comparative studies of femtosecond to microsecond laser pulses on selective pigmented cell injury in skin*, Photochem. and Photobiol. 55, 757-762 (1991).

14 D. J. Payne, R. A. Hopkins, Jr., *Effect of laser pulse width on artificial retina damage*, Laser-Tissue Interaction IX, talk 3254-19 (1998).

15 B.A. Rockwell, D.X. Hammer, P.K. Kennedy, R. Amnote, B. Eilert, J.J. Druessel, D. Payne, S. Phillips, D.J. Stolarski, G.D. Noojin, R.J. Thomas, and C.P. Cain, *Retinal Spot Size with Wavelength*, in Laser-Tissue Interaction VIII, Stephen L. Jacques, Editor, Proc. SPIE 2975, 148-154 (1997).

16 ANSI Standard Z136.1. American national standard for the safe use of lasers. American National Standards Institute, Inc., New York. 1993.

Optimal Laser Parameters for Intrastromal Corneal Surgery

Ron M. Kurtz ^{a,b}, Christopher Horvath ^{a,c}, Hsiao-Hua Liu ^a, Tibor Juhasz ^{a,b}

Center for Ultrafast Optical Science ^a and
Kellogg Eye Center, Department of Ophthalmology ^b,
University of Michigan, Ann Arbor, MI 48105
Institute of Applied Physics ^c
University of Heidelberg, Federal Republic of Germany

ABSTRACT

We characterized the effects of pulse duration, pulse energy, and spot separation on intrastromal corneal photodisruption to determine parameters that achieve optimal surface quality and tissue plane separation. Experiments utilized two laser systems, a 60 picosecond Nd:YLF laser and a 450 femtosecond Nd:Glass laser, both operating at 1.06 μm wavelength. Photodisruption was performed by tightly focusing the laser beam 150 microns below the tissue surface and scanning it in a spiral pattern to create a plane. A cut to the surface was made with the laser and the two surfaces separated to form a flap. Tissue plane separation was graded according to the additional mechanical dissection required. Internal surfaces were analyzed with standard histologic methods and scanning electron microscopy. We found that the Nd:YLF laser required approximately three times the pulse energy to achieve intrastromal cuts. Picosecond parameters also required more mechanical dissection and produced lower surface quality than optimal femtosecond parameters. We conclude that femtosecond laser pulses offer significant advantages that make them ideal candidate tools for high precision intrastromal corneal surgery. The flexibility in laser pulse delivery opens up a number of potential surgical applications not possible with current mechanical or laser devices.

Keywords: cornea, photodisruption, ultrafast laser, femtosecond, surgery

2. INTRODUCTION

In contrast to direct photoablation with ultraviolet light, such as in excimer laser photorefractive keratectomy (PRK),¹ corneal photodisruption with transparent wavelengths is based on laser-induced optical breakdown (LIOB). LIOB occurs when the fluence (energy/area) at the laser focus reaches a threshold that transforms matter of normal state to one of a high density of free electrons and ions, called a plasma. Absorption of laser pulse energy by the opaque plasma leads to rapid temperature and pressure increases in the focal spot. The expansion of the hot plasma causes a shock wave and development of a cavitation bubble. As a result of this process, termed photodisruption, tissue in the focal volume is destroyed.²

Pulsed lasers attain the high field intensities required for LIOB and photodisruption by concentrating light energy into a short time duration (since field intensity is inversely proportional to the pulse duration). Historically, ophthalmic surgical procedures which utilize photodisruption have relied on the Nd:YAG laser, which produces pulses of approximately 10 nanosecond and 1.06 μm wavelength. At this pulse duration, the energy required for beginning LIOB is relatively high, which then is transmitted to the surrounding tissue in the form of acoustic (shock) effects. The relatively large secondary shock waves associated with the Nd:YAG laser limit its ophthalmic applications to procedures such as capsulotomy and iridotomy.³

Previous studies have shown that lasers operating at shorter pulse durations require less energy and produce smaller shock waves and cavitation bubbles than the nanosecond Nd:YAG laser⁴⁻¹⁶ The Nd:YLF laser, which produces pulses in the 30-60 picosecond (picosecond) range, also operates in the near-infrared wavelength (1.06 microns). Due to its more localized collateral effects, the Nd:YLF pulses can be focused within the cornea to create intrastromal photodisruption. By scanning the laser focus at a high repetition rate, adjacent photodisruptions can perform near-contiguous cutting.

The Nd:YLF laser has been evaluated clinically for a variety of refractive and therapeutic corneal applications.¹⁸⁻²² Despite attempts at optimizing laser and delivery system parameters, including the pulse energy, spot size, and spot separation, picosecond laser intrastromal procedures have had limited clinical success due to an inability to produce fully contiguous intrastromal photodisruption.²¹⁻²³

Femtosecond laser pulses, which have a pulse duration approximately 100 times shorter than Nd:YLF picosecond pulses, may offer improvements that could make intrastromal photodisruption clinically practical. Compared to picosecond pulses, LIOB energy thresholds, shock waves and cavitation bubbles for femtosecond pulses are significantly reduced. At these pulse durations, the volume of tissue affected by the secondary shock wave and cavitation bubble are on the order of the spot size, possibly allowing the contiguous photodisruption required in clinical procedures¹⁴

To evaluate femtosecond laser corneal lamellar dissections and surface quality, we performed patterns of intrastromal corneal photodisruption in animal cadaver eyes, using a range of laser energies and spot separations. Results from a prototype solid-state femtosecond laser were compared with similar procedures performed with a Nd:YLF picosecond laser.

3. METHODS

3.1 Cadaver eyes

Intrastromal photodisruption was performed on porcine and primate cadaver eyes. Porcine eyes were obtained from a local slaughterhouse and used within four hours of death. They were kept on ice to maintain corneal clarity and thickness, which varied between 750 and 850 μm (Ophthascan, Teknar Inc). Primate eyes were enucleated after euthanasia, performed as part of an unrelated experimental protocol. They were also kept on ice and used within four hours of death. Corneal thickness varied between 400 and 500 μm .

3.2 Lasers

Femtosecond pulses were produced by a solid-state, Nd:Glass laser, operating at 1.06 mm wavelength and 450 femtosecond pulse duration. The system consists of a laser oscillator, a pulse stretcher, a regenerative amplifier, and a pulse compressor. The oscillator is mode-locked by a solid-state saturable absorber and produces a train of 250 femtosecond pulses at a repetition rate of 120 MHz. Pulses from the output of the oscillator are selected at a few KHz repetition rate and stretched to a 60 picosecond pulse duration. The pulse is then amplified in a diode-pumped regenerative amplifier and then recompressed to 450 femtosecond pulse duration. Laser energy could be varied from 1-25 μj . The beam produced from the regenerative amplifier had fundamental Gaussian (TEM_00) spatial profile. For comparisons with picosecond pulses, a 60 picosecond Nd:YLF laser (Model 5000, Escalon Medical Corp, Skillman, NJ) was passed through the same delivery system. Pulse energy for this system could be varied from 5-50 μj .

3.3 Corneal delivery system

The beam is passed through a computer-controlled corneal delivery system, which can focus to a spot size less than 10 μm within the corneal stroma. The focal spot can be scanned within a disc of 6 mm and a height of 1 mm. The eye-laser interface is a plano contact lens appplanation system, with globe stabilization provided by a suction ring. The depth of the scanned pattern is measured relative to the lower surface of the contact lens to maintain accuracy.

3.4 Surgical procedure

Globes were placed in a custom-built suction holder which maintained an intraocular pressure of approximately 30 mm Hg. The modified contact lens and laser delivery system was then applied to the corneal surface. A spiral pattern of laser pulses, focused to a spot size of 8 μm , 150-200 μm below the corneal surface, was performed at diameters ranging from 3-6 mm (Figure 1). Spot separation varied from 10-40 μm . After creating a subsurface plane, a cut to the surface was made by advancing a circle pattern from the plane through the epithelium to create a corneal flap (Figure 2).



Figure 1: A schematic of an intrastromal femtosecond laser cut. **(a)** The front view of the intrastromal spiral disk pattern. **(b)** The side view of the spiral pattern within the cornea. Note that the size of the bubbles is about 120 times smaller than the thickness of the cornea.

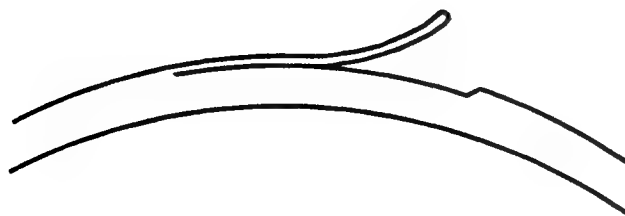


Figure 2: A schematic of the partially lifted corneal flap.

3.5 Analysis

Lamellar dissections were graded using a one to four scale, as follows;

Grade 1: Lamellar dissection requires extensive free blade cutting

Grade 2: Free blade cutting required at leading edge only to separate surfaces

Grade 3: Significant counter-traction needed to break residual adhesions, but no blade required to cut adhesions between surfaces

Grade 4: Surfaces separate with gentle traction on anterior surface using forceps only.

Following the procedure, globes were fixed in 2% glutaraldehyde with the photodisrupted surfaces exposed. Internal surfaces were analyzed by scanning electron microscopy using standard techniques.

4. RESULTS

4.1 Porcine lamellar dissections

We first investigated the ability of the femtosecond laser pulses to create lamellar dissections that did not require mechanical assistance. Based on our previous studies evaluating femtosecond cavitation bubble size as a function of laser pulse energy, values from 2-8 μj were tested at spot separations ranging from 10-30 microns (spot size was constant at approximately 8 μm). Dissection quality was graded on one to four scale as described in the methods.

As shown in Figure 3A, the ease with which the lamellar dissection could be accomplished was related both to the pulse energy and spot separation. For low pulse energies (2 μj & 4 μj), best dissection was accomplished at small spot separations (10 μm), while for the larger pulse energy (8 μj) wider spot separation (up to 20 μm) still permitted excellent separation.

These trends were also identified with 60 picosecond laser pulses at energies from 10-25 μj and spot separations from 10-30 μm . As seen in Figure 3B, blade-free dissection (Grades 3 &4) was possible with fewer parameter combinations than with the 450 femtosecond pulses. Grade 4 dissection was accomplished only at 25 μj and 10-20 μm spot separations.

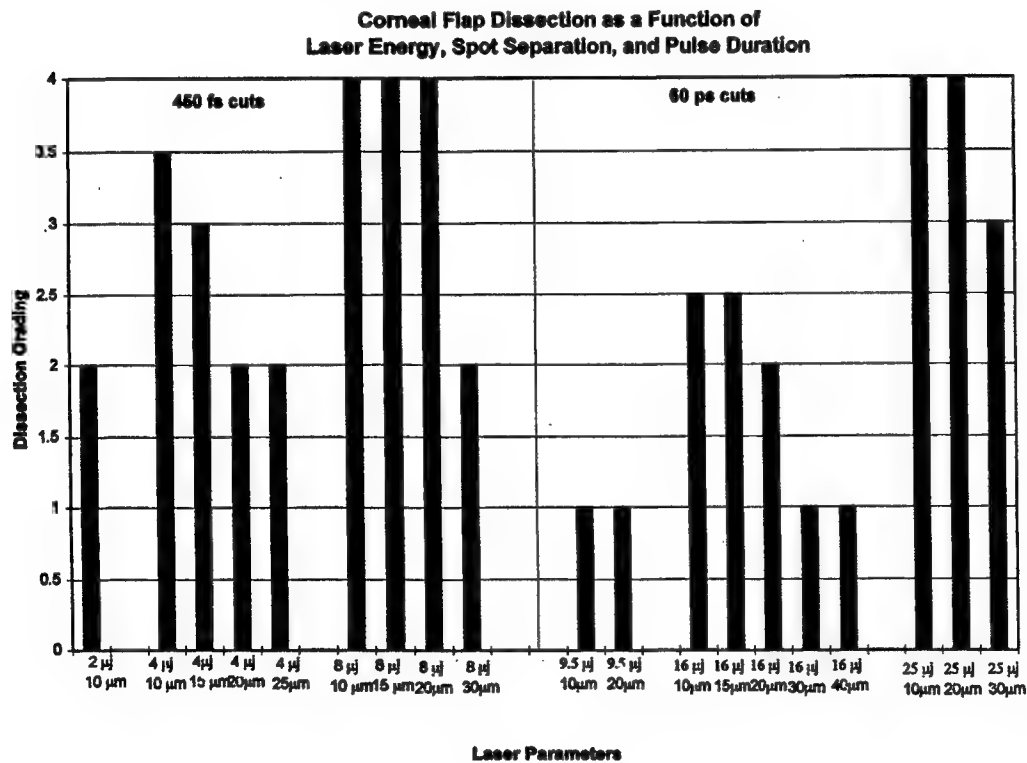


Figure 3: Dissection of corneal flaps as a function of pulse energy and spot separation for 450 femtosecond (a) and 60 picosecond laser (b) pulses. Both 4 and 8 μj femtosecond pulses produced high quality dissection, while 25 μj pulse energies were required for picosecond pulses.

4.2 SEM analysis of porcine lamellar dissections

Electron micrographs comparing the surfaces characterized by different laser parameter combinations revealed qualitative differences, which corresponded to the dissection scale grades. Surfaces created during grade 4 dissections generally showed a homogenous, dimpled pattern (Figure 4). Such surfaces

could be created with femtosecond pulses at both 4 μj and 8 μj , with wider spot separations (up to 15 μm) possible at the higher energy. Although a dissection grade of 4 was obtained at 8 μj and 20 μm spot separation, the surface quality was less homogenous than at the smaller spot separations.

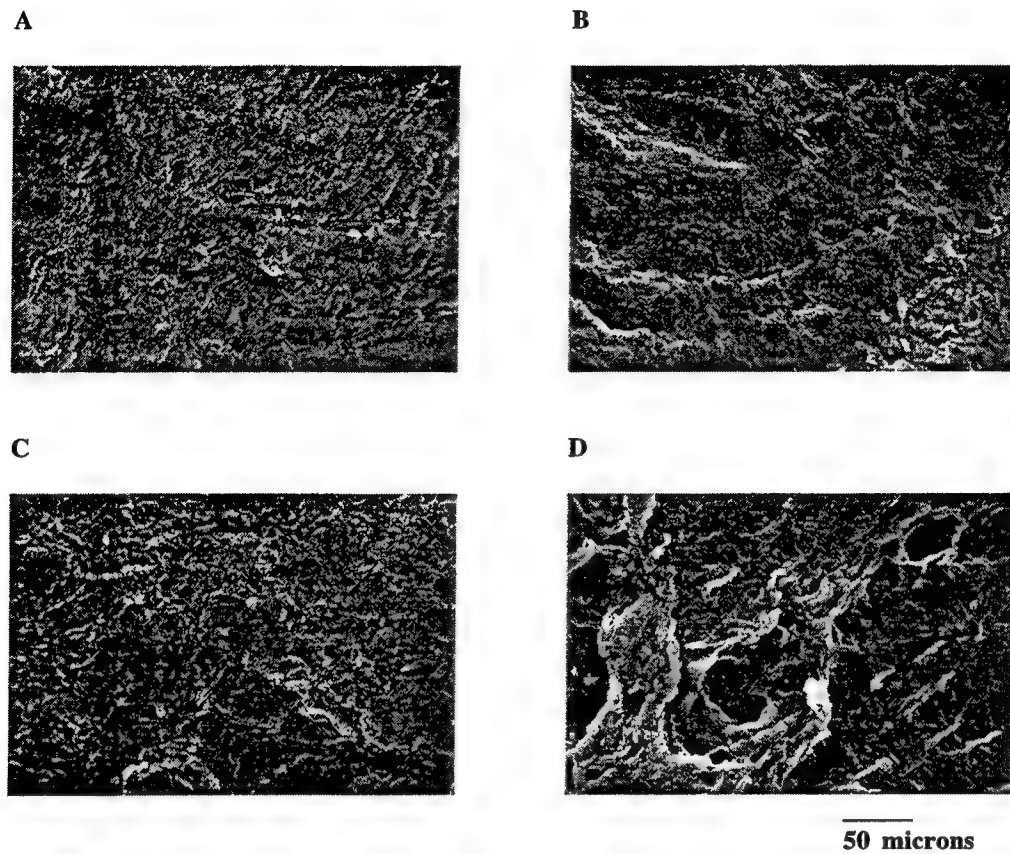


Figure 4: SEMs of 450 femtosecond high grade (Grade 4) porcine cornea lamellar dissections made with 4 μj pulse energy, 10 μm spot separation (A), 8 μj pulse energy, 10 μm spot separation (B), 8 μj pulse energy, 15 μm spot separation (C), and 8 μj pulse energy, 20 μm spot separation (D). A more irregular surface was seen with the wider spot separation (D), suggesting tissue tearing during dissection. Magnification 200 X.

Similar observations were found for 60 picosecond pulses at the 25 μj energy. For the 10 μm spot separation, a surface pattern comparable to the best femtosecond dissections was obtained. However, for the 20 μm spot separation, which also produced a grade 4 dissection, a more irregular SEM surface was seen (Figure 5), similar to the same spot separation for 450 femtoseconds at 8 μj energy (Figure 4b).

Surfaces created by femtosecond and picosecond pulses during low (1-2) grade dissections displayed irregular surface patterns suggestive of tissue tearing and use of the knife blade to complete the cuts (Figure 6). All femtosecond dissections were at least grade 2, while several picosecond parameter combinations required extensive mechanical assistance (grade 1). The blade cuts are more easily seen on these grade 1 surfaces, although they are still apparent on grade 2 dissections.

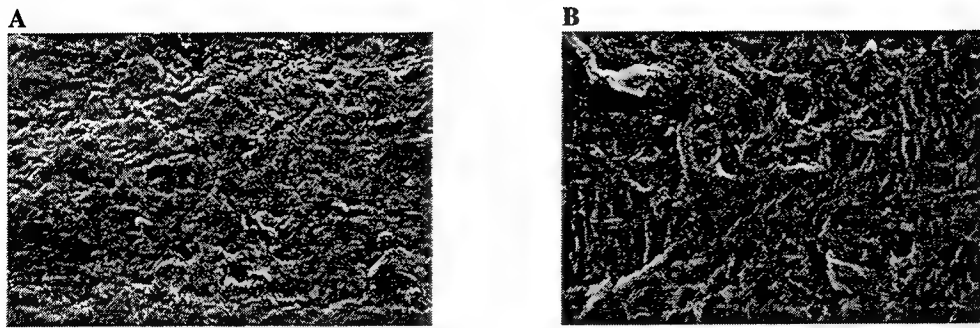


Figure 5: SEMs of 60 picosecond high grade (Grade 4) porcine cornea lamellar dissections made with 25 μ J pulse energy, 10 μ m spot separation (A), 25 μ J pulse energy, 20 μ m spot separation (B). A more irregular surface was seen with the wider spot separation (B), suggesting tissue tearing during dissection. Magnification 200 X.

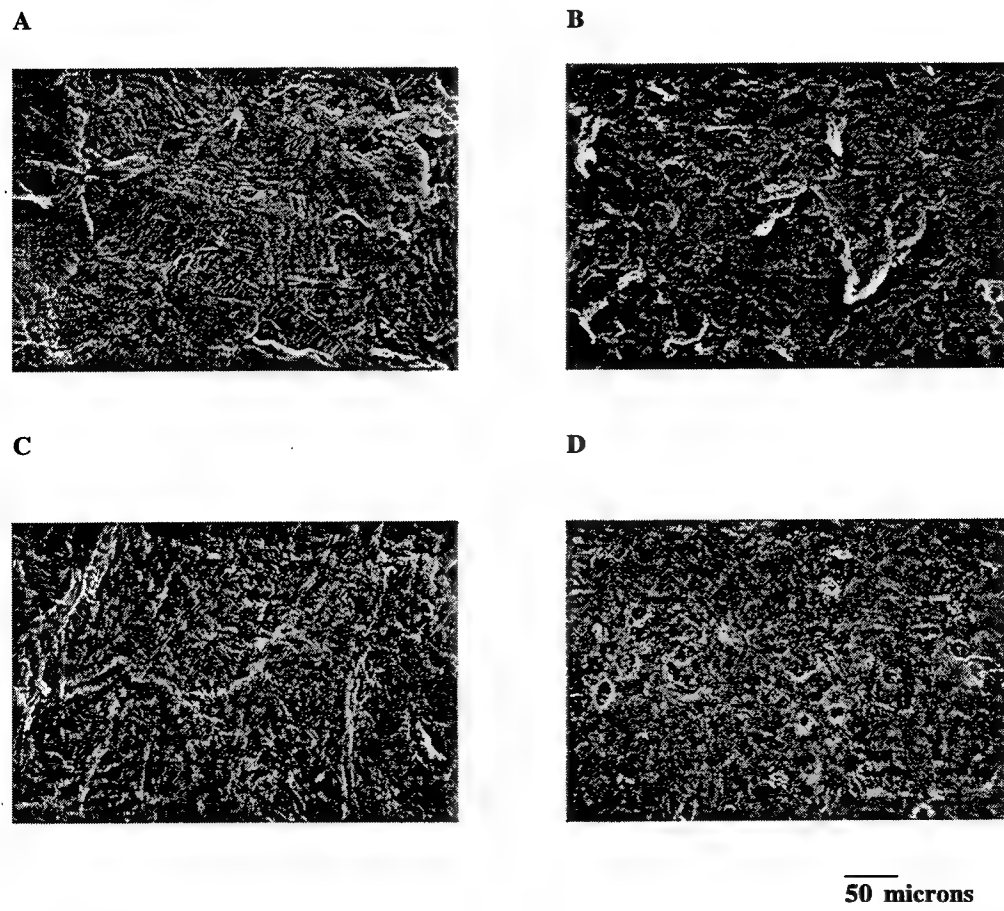


Figure 6: SEMs of 60 picosecond porcine cornea lamellar dissections made with 9.5 μ J pulse energy, 10 μ m spot separation (A, grade 1), 16 μ J pulse energy, 10 μ m spot separation (B, grade 2), and 450 femtosecond porcine cornea lamellar dissections made with 4 μ J pulse energy, 20 μ m spot separation (C, grade 2), and 8 μ J pulse energy, 30 μ m spot separation (D, grade 2). Magnification 200 X.

4.3 Lenticule cutting in porcine and primate cadaver eyes

To evaluate a prototype refractive procedure *ex vivo*, we utilized optimized femtosecond and picosecond parameters to perform laser keratomileusis,²² in which a block of corneal tissue is removed after photodisrupting its perimeter with scanned laser pulses (Figure 7).

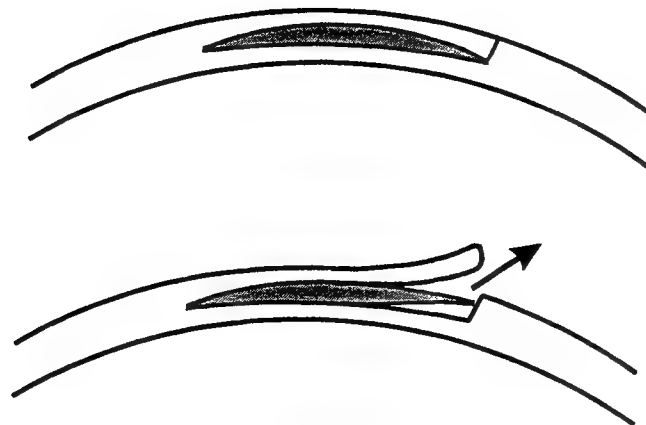


Figure 7: A schematic of laser keratomileusis. (a) A femtosecond laser cuts a lenticule within the stroma of the cornea. The laser is then used to cut a hinged flap along the perimeter of the lenticule and up the surface of the cornea. (b) The flap is lifted and the lenticule is removed. Afterward, the flap is replaced and allowed to heal.

We first performed this procedure in fresh porcine cadaver eyes using femtosecond pulses at $10\text{ }\mu\text{m}$ spot separation and $7.5\text{ }\mu\text{J}$ energy. Lenticules as thin as $50\text{ }\mu\text{m}$ could be created and removed with forceps alone (Figure 8). Because similar results using picosecond pulses have not translated to procedures in humans,²¹ we next evaluated the procedure in a model more closely resembling the human cornea. Eyes from euthanized rhesus monkeys were harvested within 2 hours of death and subjected to laser keratomileusis. Utilizing similar parameters ($15\text{ }\mu\text{m}$ spot separation and $7.5\text{ }\mu\text{J}$ energy), successful procedures could be performed using 450 femtosecond pulses (Figure 9), with excellent dissection and surface qualities. In contrast, we could not perform laser *in situ* keratomileusis in enucleated primate eyes with picosecond pulses without extensive mechanical dissection, even when parameters which had produced excellent results in porcine eyes (Figure 10).

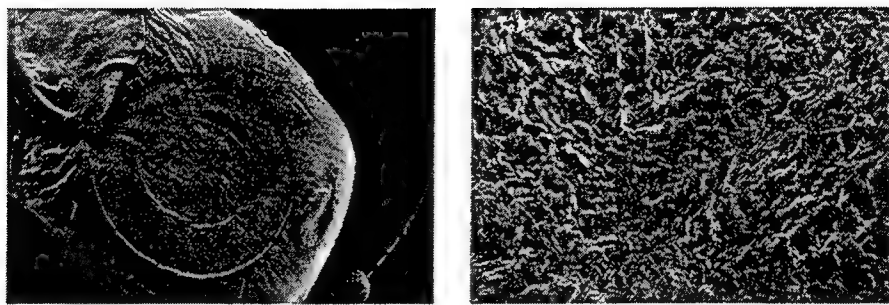


Figure 8: SEM of femtosecond laser keratomileusis in enucleated porcine eye at 10X (A) and 200 X (B) magnification. Note smooth surface made with 7.5 μ J pulse energy, 10 μ m spot separation. A 70 μ m lenticule is shown to right of corneal bed, with flap to left.

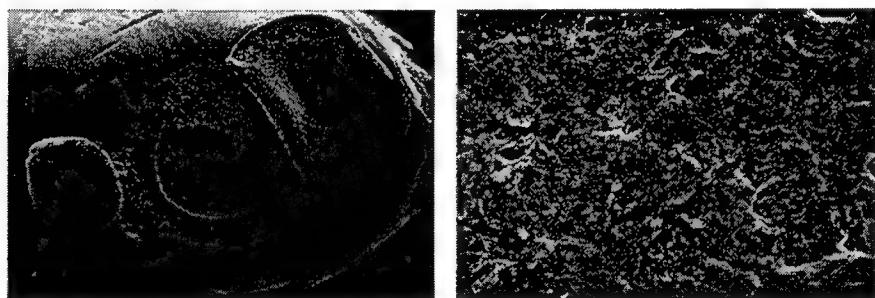


Figure 9: SEM of femtosecond laser keratomileusis in enucleated primate eye at 10X (A) and 200 X (B) magnification. Note smooth surface made with 7.5 μ J pulse energy, 15 μ m spot separation. A 100 μ m lenticule is shown to left of corneal bed, with flap to right.

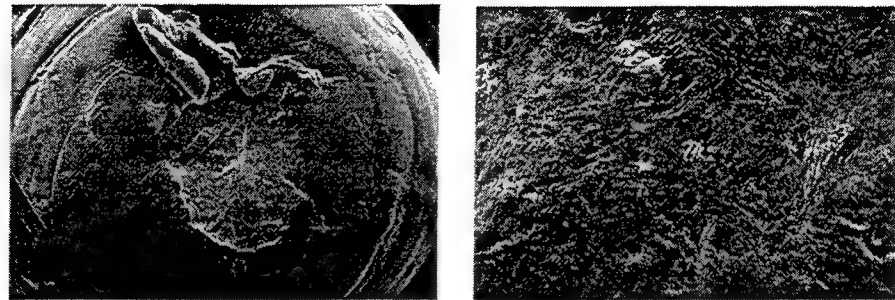


Figure 10: SEM of 60 picosecond laser keratomileusis in enucleated primate eye at 10X (A) and 200 X (B) magnification. Note irregular surface made with 25 μ J pulse energy, 15 μ m spot separation. A lenticule could not be dissected free due to interconnections between the anterior lenticule surface and the flap.

5. DISCUSSION

Lamellar corneal dissection (using scanned patterns of ultrashort laser intrastromal photodisruption) has been advocated as a potential adjunct and alternative to current refractive surgery techniques.^{18, 20-22} While picosecond lasers were first advanced for this purpose, clinical results in humans have been disappointing.²¹ Our findings indicate that many of the shortcomings of picosecond technology (including incomplete tissue cutting, poor dissection and surface quality) are significantly improved when the pulse duration is further reduced into the femtosecond regime.

The clinical improvements obtained with femtosecond pulses can be understood by considering the pulse duration dependency of the photodisruptive process itself. Complete intrastromal lamellar dissection requires contiguous photodisruption, in turn necessitating a match between the plasma volume, cavitation bubble size, and the pattern spot separation. If the spot separation in a particular scanning pattern is too large for the chosen laser parameters, tissue islands are left behind that must be broken mechanically. If spot separations are too small, the cavitation bubble interferes with the next photodisruption, thereby also preventing contiguous cutting.²³

Photodisruption begins with formation of a plasma, the size of which is largely dependent on the focal spot diameter of the optical delivery system. Generally, the smallest spot diameter is desired, since this requires the lowest pulse energy to exceed the intensity threshold for plasma generation. In most delivery systems, there is a practical optical limitation on spot diameter of 8-10 μ m, which is constant over a wide range of pulse durations and energies. Procedure time and mechanical limitations also impose constraints on how small a focus size can be used and how fast it can be scanned.

At these 8-10 μ m focal spot sizes, nanosecond pulses from the Nd:YAG laser require millijoule level energies to generate a plasma.³ The secondary acoustic effects spread over several hundred microns, making contiguous corneal photodisruption impossible.¹⁵ For picosecond pulses operating at threshold energies, focal spots of approximately 8-10 μ m predict final cavitation bubble sizes of approximately 25 μ m, a 1:3 ratio which results in near-contiguous photodisruption.²³ In contrast, for femtosecond plasma volumes of approximately 8-10 μ m at threshold energies, cavitation sizes are predicted at approximately half picosecond values, at approximately 12 μ m.¹⁴ This ratio of 1:1.5, translates into closer placement of femtosecond

thresholds associated with femtosecond pulses, which translate into highly controlled and reproducible photodisruption.⁹

While the current results in porcine eyes are encouraging, the differences in picosecond laser behavior in this model (as reported previously) and human clinical studies must be kept in mind.^{21,22} Our findings also reveal that picosecond parameters that work in enucleated porcine corneas do not translate well into (freshly enucleated) primate eyes. While femtosecond parameters did cross over well to the ex vivo primate model, in vivo systems that closely reproduce the clinical situation must ultimately be used.

The laser parameters outlined here provide attainable requirements for any potential clinical devices. Advances in ultrafast laser design and the development of powerful laser diodes has made low cost, reliable, diode-pumped, femtosecond laser systems possible for the first time.²³ Combined with sophisticated scanning delivery systems now available, a number of potential laser corneal procedures are possible, including corneal flap cutting, laser keratomileusis and possibly intrastromal keratectomy.

6. ACKNOWLEDGMENTS

This research received grant support from Research to Prevent Blindness (RMK), the Midwest Eye Banks & Transplantation Centers, National Science Foundation (through the Center for Ultrafast Optical Science under STC PHY 8920108), and the National Eye Institute (Core Grant EY-00703)

7. REFERENCES

1. Trokel S, Srinivasan R, Braren B. Excimer laser surgery of the cornea. *Am J Ophthalmol*, 1983;94:125.
2. Bloembergen N. Laser-induced electric breakdown in solids. *IEEE J Quantum Electron* 1974;375:192-202.
3. Steinert RF, Puliafito CA. *The Nd YAG Laser in Ophthalmology*. Philadelphia: W.B. Saunders; 1985;11-21.
4. Bettis JR, House RA, and Guenther AH. Spot size and pulse duration dependence of laser-induced damage. In: Glass AJ, Guenther AH, eds. *Laser Induced Damage in Optical Materials*: 1976. Washington: U.S. Dept. of Commerce, 1976; 338-45 (National Bureau of Standards Special Publication 462; Proc Symposium on Optical Materials for High Power Lasers, 8th, Boulder, CO, 1976).
5. Stern D, Schoenlein RW, Puliafito CA, Dobi ET, Birngruber R, Fujimoto JG. Corneal ablation by nanosecond, picosecond, and femtosecond lasers at 532 and 625 nm. *Arch Ophthalmol*. 1989;107:587-92.
6. Niemz MH, Hoppeler TP, Juhasz T, Bille JF. Intrastromal ablations for refractive corneal surgery using picosecond infrared laser pulses: tissue effects in cornea, lens, and retina. *Lasers Light Ophthalmol*. 1993;5:149-55.
7. Vogel A, Capon MRC, Asigo-Vogel MN, Birngruber R. Intraocular photodisruption with picosecond and nanosecond laser pulses. *Invest Ophthalmol Vis Sci*. 1994;35:3032-44.
8. Du D, Liu X, Korn G, Squier J, Mourou G. Laser-induced breakdown by impact ionization in SiO₂ with pulse durations from 7 ns to 150 femtosecond: *Appl Phys Lett*. 1994;64:3071-3.
9. Kurtz RM, Liu X, Elner VM, Squier JA, Due D, and Mourou GA. Plasma-mediated ablation in human cornea as a function of laser pulsedwidth. *Journal of Refractive Surgery*, 1997;13:
10. Loesel FH, Niemz MH, Bille JF, and Juhasz T. Laser induced optical breakdown on hard and soft tissues and its dependence on the pulse duration: experiment and model. *IEEE Journal of Quantum Electronics* 32:1717-1722 1996.
11. Du D, Squier J, Kurtz R, Elner V, Liu X, Gutmann G, and Mourou G. Damage threshold as a function of pulse duration in biological tissue, In Ultrafast Phenomena IX, ed by P. F. Barbara et al. New York, Springer, pp 254-256, 1995.
12. Zysset B, Fujimoto JG, Puliafito CA, Birngruber R, and Deutsch TF. Picosecond optical breakdown: Tissue effects and reduction of collateral damage. *Lasers Surg Med* 9: 193-204, 1989.
13. Zysset B, Fujimoto JG, and Deutsch TF. Time-resolved measurements of picosecond optical breakdown. *Appl Phys B* 48: 139-147, 1989.

14. Juhasz T, Kastis GA, Suarez C, Bor Z, Bron WE. Time-resolved observations of shock waves and cavitation bubbles generated by femtosecond laser pulses in corneal tissue and water. *Lasers Surg Med* 1996;19:23-29.
15. Vogel A, Busch S, Jungnickel K, Bringruber R. Mechanisms of intraocular photodisruption with picosecond and nanosecond laser pulses. *Lasers Surg Med*. 1994; 15:32-43.
16. Loesel FH, Niemz MH, Bille JF, Juhasz T. Laser-induced optical breakdown on hard and soft tissue and its dependence of the pulse duration: Experiment and Model. *IEEE J Quant Elect*. 1996;32:1717-22.
17. Juhasz T, Hu XH, Turi L, and Bor Z. Dynamics of shock waves and cavitations generated by picosecond laser pulses in corneal tissue and water. *Lasers Surg Med* 15: 91-96, 1994.
18. Krueger R, Quantock A, Juhasz T, Ito M, Assil K, Schanzlin DJ. Ultrastructure of picosecond laser intrastromal photodisruption, 1996;12:607-12.
19. Freuh B, Bille J, Brown S. Intrastromal relaxing excisions in rabbits using a picosecond infrared laser. *Lasers and Light in Ophthalmol*, 1992;4:165-8.
20. Habib M, Speaker M, McCormick S, Kaiser R. Wound healing following intrastromal photorefractive keratectomy with the Nd:YLF picosecond laser in the cat. *Journal of Refractive Surg*, 1995;11:442-7.
21. Gimbel H, Coupland S, Ferensowisc M. Review of intrastromal photorefractive keratectomy with the Nd:YLF laser. *Int Ophthalmol Clin*, 1997; 37: 95-102.
22. Ito M, Quantock A, Malhan S, Schanzlin DJ, and Krueger RR. Picosecond laser in situ keratomileusis with a 1053-nm Nd:YLF laser. *Journal of Refractive Surgery* 12:721-728, 1996.
23. Vogel
24. Braun A, Liu H, Horvath C, Liu X, Juhasz T, Mourou G. All solid-state, directly diode-pumped chirped-pulse amplification laser system. *OSA Technical Digest*, 1997;11:323-324.

Laser Spot Size as a Function of Tissue Depth and Laser Wavelength in Human Sclera

Zachary S. Sacks^a, Ron M. Kurtz^{a,b} Ralph Fenn^b, Frieder Loesel^c,
Gerard Mourou^a, Tibor Juhasz^{a,b}

Center for Ultrafast Optical Science^a and
Kellogg Eye Center, Department of Ophthalmology^b,
University of Michigan, Ann Arbor, MI 48105
Institute of Applied Physics, University of Heidelberg^c,
Federal Republic of Germany

ABSTRACT

We determined the wavelength dependence of the minimum spot size of a laser beam focused through human sclera to evaluate the potential for transscleral glaucoma surgical techniques using ultrashort-pulsed lasers. The spectrum of the forward scattered light was measured by collimating the incident and transmitted beam in a spectrophotometer. This spectrum shows that sclera is highly scattering until 1100 nm, after which, the transmission spectrum is similar to water. To measure the minimal spot size, a laser beam was focused on the back surface of sclera of differing thickness. The minimum spot at 800 nm, 1060 nm, 1301 nm, and 1557 nm was imaged. At 800 nm, the spot size was invariant upon focal lens position, being a thousand fold larger than the incident beam spot size. As the wavelength increased, the area of the spot decreased, so that at 1557 nm, the minimal spot size was on the order of the incident beam spot size.

Keywords: sclera, scattering, spot size, wavelength dependence, surgery, glaucoma

2. INTRODUCTION

Glaucoma affects approximately two million Americans while another ten million are at risk due to statistically significant elevated intraocular pressure (IOP). Medications can lower IOP, although they are only partially effective, with an approximately 40% failure rate over 3 years.¹ Laser and incisional surgical procedures, which increase fluid drainage from the eye, are generally reserved for medication failures. Argon laser trabeculoplasty, the most common laser glaucoma procedure, may stretch the normal channels in the trabecular meshwork, thereby increasing outflow of aqueous humor. The effectiveness of this procedure is short lived however, averaging about two years, after which incisional surgery is often tried.^{2,3}

Filtering surgery, the cutting of a drainage channel (fistula) directly into the sclera, is the most common incisional surgery for the treatment of glaucoma. The various techniques all share a host of complications, including very low intraocular pressure (hypotony), cataract formation, and infection.^{4,5,6} In addition, surgical failure often occurs over the course of months to years due to scarring and closure of the fistula. Despite these problems, glaucoma specialists are moving towards earlier surgical intervention due to its better IOP control in most patients, increasing the need for a safer and more effective surgical alternative.

The majority of post-operative scarring responsible for fistula closure occurs due to wound healing in the tissues overlying the sclera, the conjunctiva and episclera, which are damaged during incisional procedures.⁷ A number of laser surgical procedures to improve surgical outcomes have been proposed and tested.⁸ These generally fall into two approaches:

1. **Ab interno** procedures, which ablate tissue from the internal surface of the sclera, either by directing the light through the cornea with a contact lens or directly via a probe introduced into the anterior chamber of the eye.
2. **Ab externo** procedures, which ablate tissue from the external surface of the sclera, either by directing the light through the conjunctiva or directly via a probe introduced under the conjunctiva.

Despite these attempts, no laser-based method has delivered enough clinical or economic advantages to displace traditional surgical methods. Ultrashort-pulsed lasers, operating at appropriate wavelengths, may permit unique transcleral procedures that could offer advantages of each of these methods.

Femtosecond laser pulses used for cornea surgery have been demonstrated to cause little collateral damage, both due to the low average power -- no burning -- and to their low pulse energy -- small shock waves and bubble oscillations.⁹ In addition, subsurface tissue photodisruption is possible and has been demonstrated in transparent corneal tissue using near-infrared and infrared wavelengths.^{10,11} By using a wavelength that is transmitted by the sclera, and is able to be focused at its back surface, it may be possible to create an **ab interno** fistula without the technical problems associated with contact lens or probe delivery methods. Such a method would avoid disruption of the overlying conjunctiva and episclera, something current **ab externo** techniques cannot offer.

As a first step, this paper examines the minimum spot size attainable as a function of wavelength when the laser is focussed through the sclera itself to its back surface. Our first experiment yielded forward transmission for the wavelengths between 500 nm and 2500 nm using a spectrophotometer to obtain an initial indicator of scattering and minimum spot size. For the second experiment, we imaged the spot on the back surface of the sclera using a vidicon camera with a microscope objective, comparing wavelengths from 800 nm to 1557 nm.

3. METHODS

3.1 Tissue Samples

Human scleral sections (not suitable for transplantation) from regions adjacent to the cornea were cut to a thickness ranging from 0.30 mm to 0.77 mm using a vibratome. Four different thickness sections from each of three globes were cut for a total of twelve samples. The sample thickness was measured before each experiment using a calipers and all measurements were made within two weeks of globe donation.

3.2 Experiment 1: Spectrophotometer Measurements

The forward scattered light as a function of wavelength was measured using a spectrophotometer (Perkin-Elmer Lambda 9 UV/VIS/NIR Spectrophotometer) by placing the apparatus shown in Fig. 1 inside the sample chamber.^{12,13} The apparatus collimates the incident incoherent broadband light using two irises with a 2.16 mm diameter opening separated by approximately 3.0 cm. The tissue was mounted to a slide (1mm thick) using a drop of saline solution. The forward scattered light was collected using two irises separated by 3 cm with 2.16 mm opening. The tissue was centered between the two sets of irises separated by approximately 2.3 cm.

For each of the twelve samples, three measurements of the absorption spectrum, 500-2500 nm, were taken, then converted to total transmission. This measurement was taken to identify trends in forward scattering to narrow the search for optimal wavelengths to penetrate the sclera.

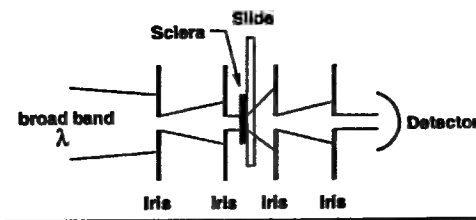


Figure 1: The tissue holder for the spectrophotometer only allows collimated light to strike the sclera and only collects the forward transmitted light. The incident beam is a converging incoherent broadband source.

3.3 Experiment 2: Spot Size Measurements

Figure 2 shows the experimental setup used to measure the minimum spot size. The laser light is incident from the left onto a variable attenuator to prevent camera saturation. The beam then passes through a soft aperture (about 2 m of Corning Flexcor 1060 or Newport F-SV 620 for 800 nm optical fiber) to insure that the beam from each source is fundamental Gaussian mode. The emergent beam was collimated (Newport 1015LD, $f = 7.4$ mm), then focused using a 6.24 mm focal length lens with a NA of 0.40 (Thor Labs 350110-C). The front surface of a 0.15 mm thick microscope cover slip was placed at the focal spot. This surface corresponds to the back surface of the sclera. The vidicon camera (Electrophysics Model 7290A) was positioned such that the object plane corresponded to the back surface of the tissue while using a 20X 0.40 NA microscope objective. The minimum spot size was recorded as a 640 X 480 24 Bit RGB bitmap.

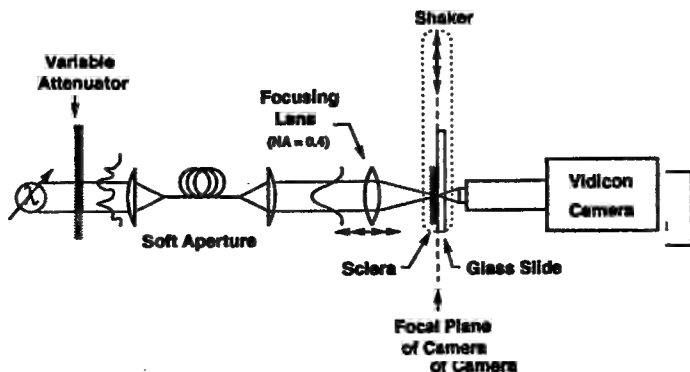


Figure 2: The minimum spot size was determined by placing the back surface of the sclera in the focal plane of a microscope camera. The focusing lens was moved until the minimum spot size was obtained.

The tissue was placed on the cover with a drop of saline. The lens position that produced the minimum spot size at the back surface of the sclera was determined by shaking the tissue horizontally in the focal plane and moving the lens until the smallest spot occurred. The Electrophysics Model 7290A camera has a slow response time so that shaking the sample allowed us to average over a portion of the tissue.

The shaker was DC motor with an off center circular cam that provided about 1 mm of motion. This image was recorded, then the shaker was stopped and several stationary images of the speckle were taken. The above procedure was preformed using four different lasers: a 800 nm Ti:Sapphire oscillator operating at 100 MHz and 50 fs pulses, a 1060 nm Nd:Glass oscillator at 100 MHz and 300 fs pulses, a 1301 nm continuous wave laser diode, and a Er:Glass fiber laser operating with 100 fs pulses at 100 MHz.

3.4 Image Analysis

The camera images collected were corrected for the nonlinear camera response and normalized such that the peak intensity was the same for all images. The full-area half-maximum (FAHM) sizes, as defined as the area of the spot that is greater than or equal to the maximum pixel intensity, were calculated for each image as a comparison between the different wavelengths. The FAHM is the relevant measure since the area of the spot is directly proportional to the energy for photodisruption.

4. RESULTS

4.1 Forward Scattering of Sclera

Twelve absorption spectra of half thickness sclera (average 0.34 mm) were averaged and are shown in Fig. 3. Very little forward transmission occurs below 1100 nm. The graph shows transmission dips that follow the water dips at 1450 nm and 1900 nm. Several wavelengths of interest are listed in Table 1.

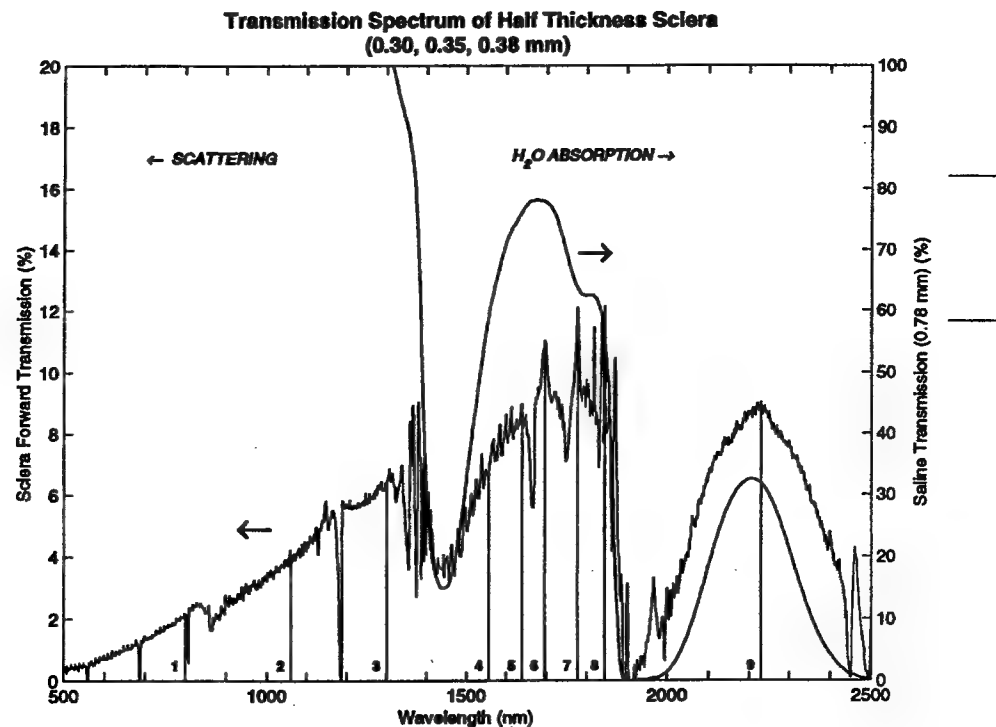


Figure 3: The forward transmission of sclera is the jagged curve. The smooth curve is the percent transmission through 0.78 mm of saline solution. See Table 1 for the numbers noted in the graph.

Table 1: Forward transmission of half thickness of sclera.

Number	Wavelength (nm)	Laser	Forward Transmission (%)	Saline Transmission (%)
1	800	Ti:Sapphire	2.15	100
2	1060	Nd:Glass	4.02	100
3	1301	Laser Diode	6.22	100
4	1557	Er:Glass	6.77	59.5
5	1639	NA	8.96	76.3
6	1695	NA	11.02	77.9
7	1777	NA	12.11	63.5
8	1845	NA	12.14	55.3
9	2229	NA	9.01	31.8

The trends in spectrophotometer measurements were consistent between samples. Sclera displayed the same transmission minima as saline at 1450 nm and 1900 nm (as can be expected since sclera is 80% water). However, at wavelengths below 1100 nm, where water is transparent at this thickness, the forward transmission of sclera increased linearly, in contrast to expected results and implying that significant scattering occurs for these shorter wavelengths.¹³ At longer wavelengths, the forward transmission increased except for the absorption peaks of water at 1450nm and 1900 nm. Local maxima occur at 1695 nm, 1777 nm, 1845 nm, and 2229 nm. The first and last of these peaks correspond to the water transmission peaks as shown in Fig. 3.

4.2 Minimum Spot Size Measurements

The minimum size (defined as the spot size without the tissue) are shown in Figure 4. The difference in sizes is most likely due to slightly different beam divergences and the wavelength. The size of the speckle image at 800 nm was invariant with translation of the lens. Figure 5 shows the minimum spot size obtainable at different wavelengths through full thickness of sclera. As expected in highly scattering tissue, the pattern is dominated by speckle. At 800 nm, the average spot size is roughly 1000 times the size of the minimum spot. The average sizes appear to decrease for 1301 nm and 1557 nm, respectively. Figures 6 display the moving averaged images of the spot size through the full thickness of the sclera.

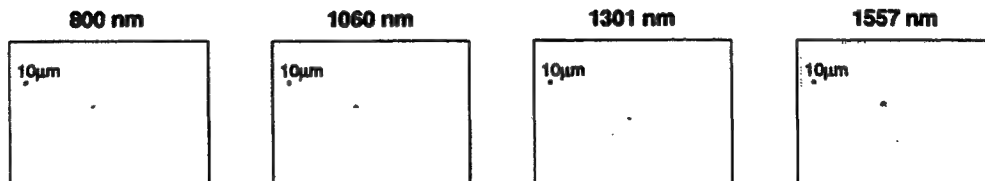


Figure 4: The minimum spot size at the tested wavelengths are shown. The minimum spot size is the size of the beam when focused on to the front surface of the cover slip.

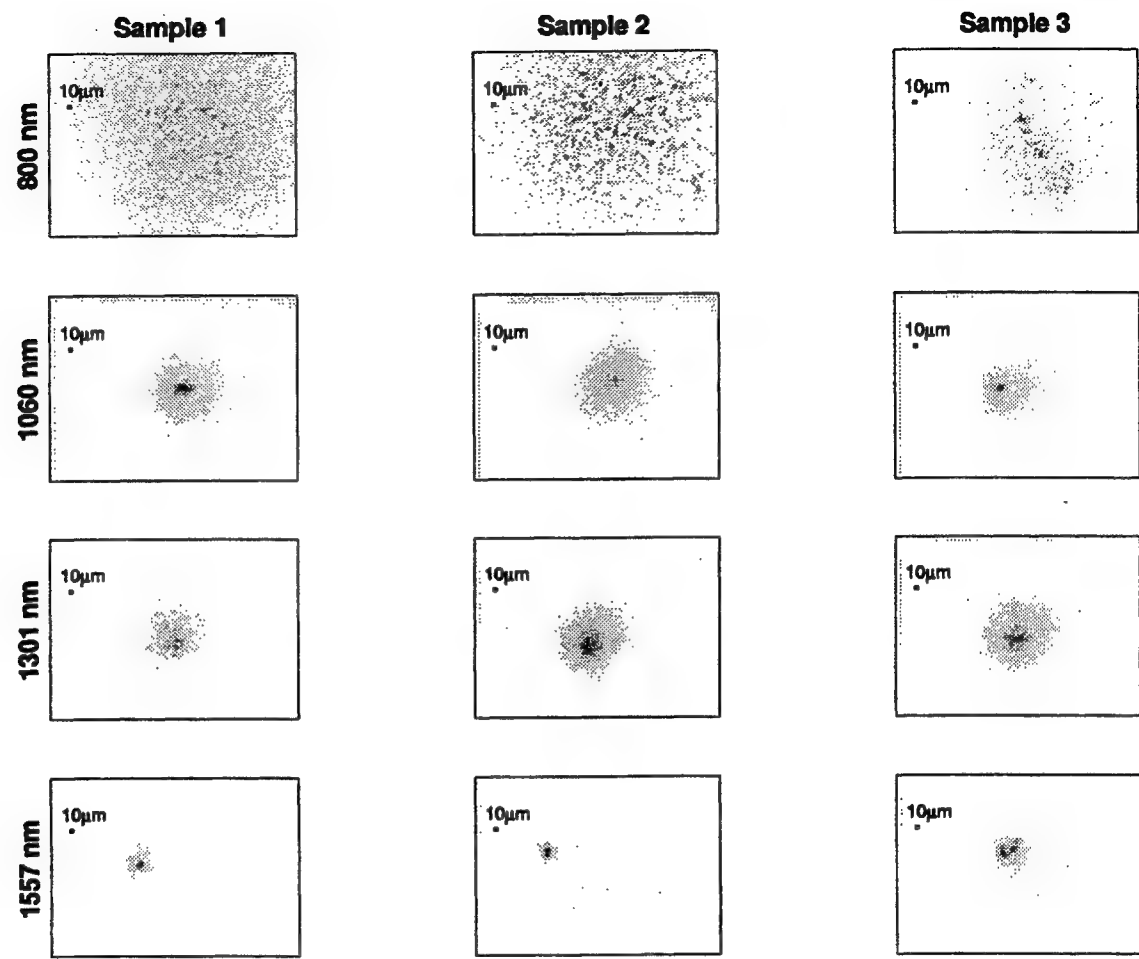


Figure 5: Typical speckle patterns through full thickness of sclera.

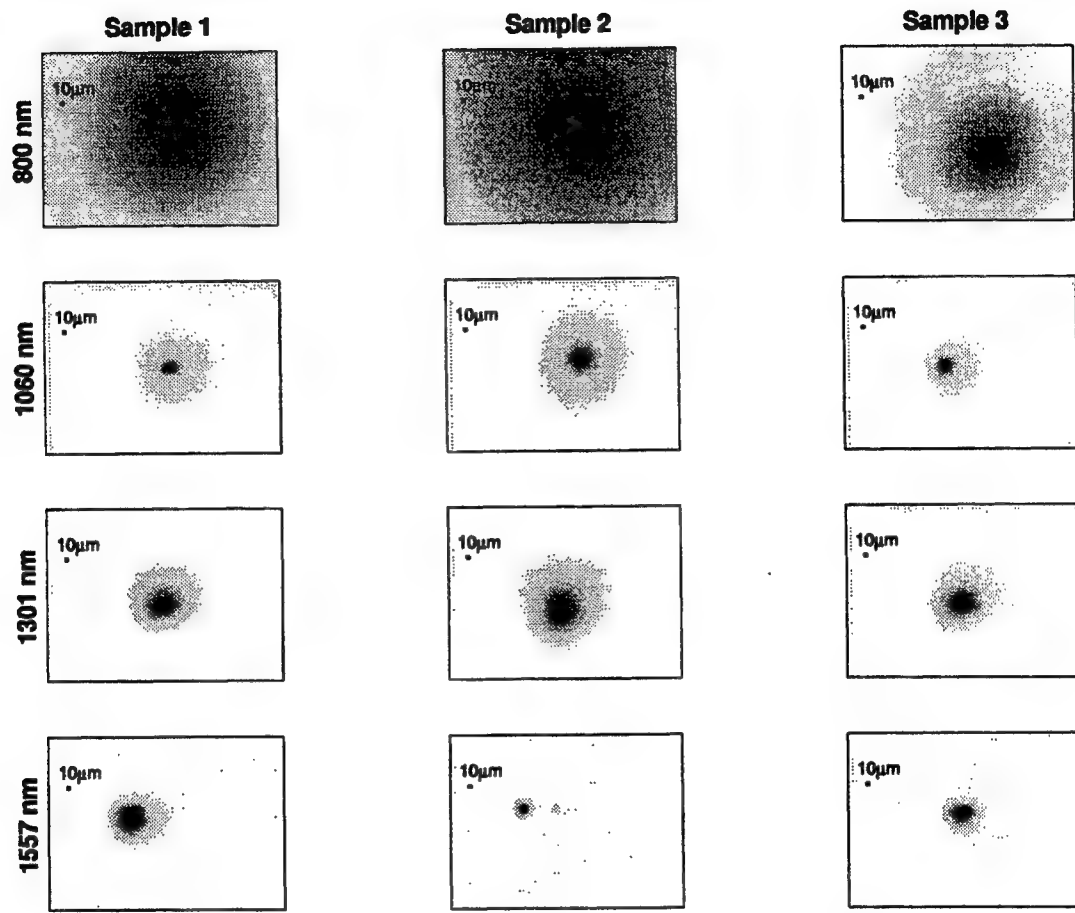


Figure 6: The image obtained when the tissue was shaken over 1 mm.

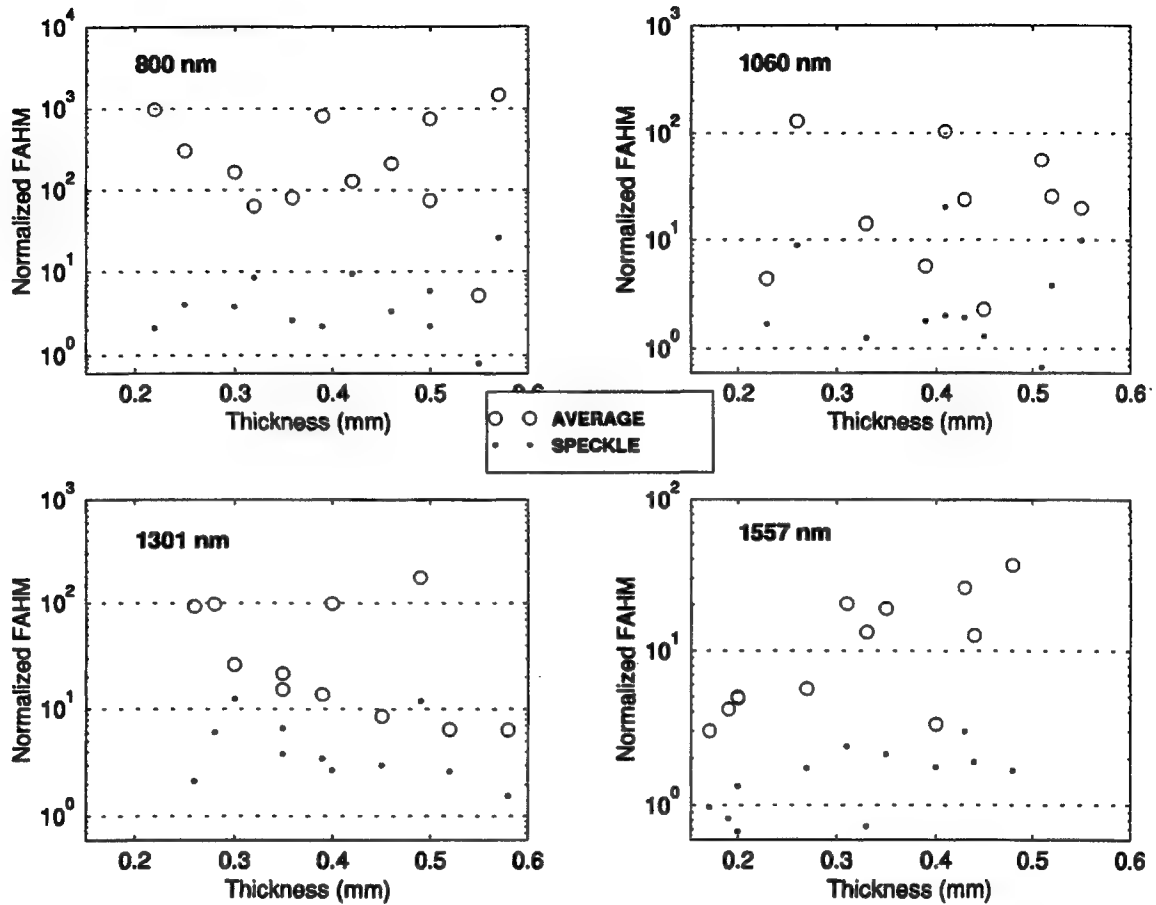


Figure 7: The FAHM for the averaged measurements (shaken) and the speckle (stationary) patterns are shown. The FAHM were normalized to the FAHM of the minimum spot size without the tissue.

Figure 7 shows the FAHM of the shaken tissue. The FAHM of the speckle can be less than the minimum spot size. The data at 800 nm suggests severely peaked and separated speckle since the FAHM of the speckle is up to two orders of magnitude less than the average (Figure 5). As the wavelength increases, the average FAHM becomes more predictable, *i.e.* increases with increasing tissue thickness, and the average FAHM and speckle FAHM begin to converge.

4.3 Prototype Trans-tissue Procedure

To demonstrate how a transcleral channel might be created using subsurface photodisruption, we next performed a transcorneal fistula using a 1060 nm 450 fs laser. The method is schematized in Figure 8a. In this study, we left the channel partial thickness to show that no damage to the external surface was created.

A similar experiment in sclera using the same laser was able to obtain consistent photodisruption at depths of 250 μm or less. This corresponds with the average FAHM of Figure 7.

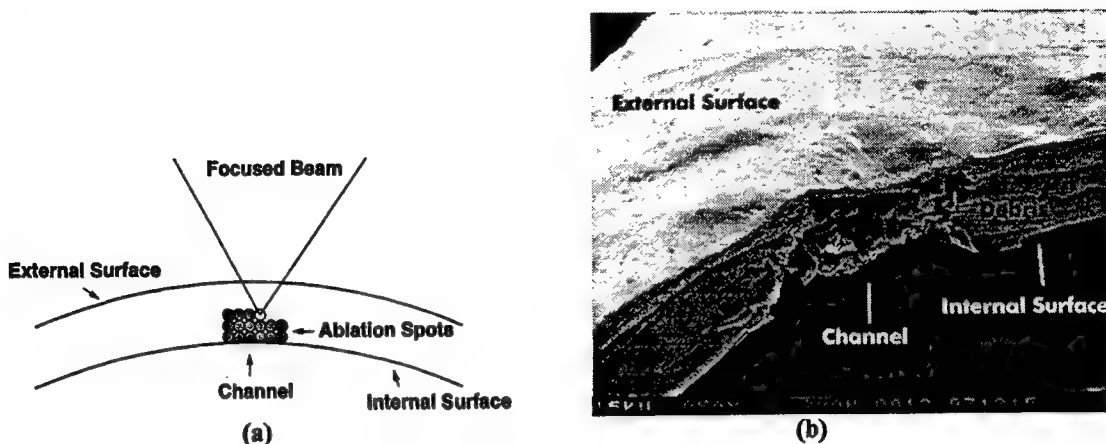


Figure 8: (a) Procedure used to cut the cornea fistula. (b) A hole cut in cornea from the back surface to the front surface using 1060 nm femtosecond pulses. Note that the top (external surface) layer is intact.

5. DISCUSSION

Analogous to recent work using ultrashort-pulsed lasers for subsurface corneal photodisruption, we have begun to characterize laser parameters for transcleral surgical procedures. Beginning with laser wavelength, we first defined the scattering properties of the scleral tissue. In contrast to the cornea, which transmits up to 90% of visible wavelengths, the white sclera is an excellent scatterer of visible light. Surprisingly, the cornea and sclera are similar in structure. Both are composed of collagen fibers (optical index $n = 1.47$) embedded in a mucopolysaccharide ground substance ($n = 1.345$). The main differences are the average center to center fibril spacing and the regularity of the structure. Fourier analysis reveals that the center-to-center spacing in cornea and sclera are 59 nm and 285 nm, respectively, with the variations being greater in sclera.^{14,15} Bragg diffraction theory predicts that scattering begins once the half wavelength of light in the tissue is on the order of the index variations in the medium.¹⁶ For cornea and sclera, scattering is expected to be significant for wavelengths shorter than 166 nm and 800 nm, respectively, using this theory. Since the peaks of the spatial frequency spectrum of sclera are quite broad,¹⁵ significant scattering at longer wavelengths may also occur.

Since the average spot size decreases by about two orders of magnitude from 800 nm to 1557 nm, longer wavelengths may be preferable for transcleral applications. Considering only scattering, subsurface photodisruption at 800 nm would require at least energies 1000 times greater than surface photodisruption. Pulses of such high energy may reach threshold above the focal spot, resulting in photodisruption near the surface of the tissue. At 1557 nm, the pulse energy needs to be only about four times greater than at the surface. These results require expansion in ex vivo and in vivo models to determine laser energy, repetition rate and pulse width parameter specifications. The preliminary data in this paper suggests that transcleral glaucoma surgery may be possible at longer wavelengths and ultrashort pulse widths.

6. ACKNOWLEDGMENTS

This research received grant support from Research to Prevent Blindness (RMK), the Midwest Eye Banks & Transplantation Centers, National Science Foundation (through the Center for Ultrafast Optical Science under STC PHY 8920108), and the National Eye Institute (Core Grant EY-00703). Special thanks to Michelle Intiso of Electrophysics Corp. for providing the camera; George Nowak, Robin Bruener, Junji Urayama, Dr. Ted Norris, Doug Craig, Dr. John Whitaker, Christopher Horvath, and John Nees for providing the lasers; Dr. Sterling Backus, Dr. Charles Durfee, Dr. Henry Kapteyn, and Dr. Margaret Murnane for providing additional equipment; and Dr. Emmet Leith and Brian Hoover for many enlightening discussions. We also thank Bruce Donahoe at the University of Michigan Cell Biology Laboratory for assistance with electron microscopy.

7. REFERENCES

1. Diggory P, Franks W. Medical treatment of glaucoma - a reappraisal of the risks. *Br J Ophthalmol* 80:85-89, 1996.
2. Glaucoma Laser Trial Research Group. The Glaucoma Laser Trial (GLT): Results of argon laser trabeculoplasty versus topical medicines. *Ophthalmology* 97:1404-1413, 1990.
3. Migdal C, Hitchings R. Control of chronic simple glaucoma with primary medical, surgical, and laser treatment. *Trans Ophthalmol Soc UK* 105:653-656, 1986.
4. Shirato S, Kitazawa Y, Mishima S. A critical analysis of the trabeculectomy results by a prospective follow-up design. *Japan J Ophthalmol* 26:468-480, 1982.
5. Tornqvist G, Drolsum LK. Trabeculectomies - a long-term study. *Acta Ophthalmologica* 69:450-454, 1991.
6. Clarke MP, Vernon SA, Sheldrick JH. The development of cataract following trabeculectomy. *Eye* 4:577-583, 1990.
7. Frankhauser F. Wound Healing in Glaucoma Filtering Surgery. Amsterdam/New York: Kugler Publications, 1992.
8. Berlin M, Ahn R. A review of laser applications in glaucoma filtering surgery. *SPIE Vol. 2100 Cell and Biotissue Optics* 1994; 304:310.
9. Juhasz T, Kastis GA, Suarez C, Bor Z, Bron WE. Time-resolved observations of shock waves and cavitation bubbles generated by femtosecond laser pulses in corneal tissue and water. *Lasers Surg Med* 1996;19:23-29.
10. Kurtz RM, Liu X, Elner V, Squier J, Du D, Mourou G. Photodisruption as a function of Laser Pulsewidth. *J Refract Surg* 1997;13:653-658.
11. Liu X, Kurtz R, Braun A, Liu H, Sacks Z, Juhasz T. Intrastromal corneal surgery with femtosecond laser pulses. *OSA Technical Digest Series* 1997;11:1687.
12. Maitland D. J., Walsh J. T. Jr., Prystowsky J. B. Optical properties of human gallbladder tissue and bile. *Applied Optics* 1993; 32,4:586-591.
13. Parsa P, Jacques S. L., Nishioka N. S. Optical properties of rat liver between 350 and 2200 nm. *Applied Optics* 1989; 28,12:2325-2330.
14. Vaezy S, Clark J. I. A quantitative analysis of transparency in human sclera and cornea using Fourier Methods. *Journal of Microscopy* 1991. 163 Pt. 1: 85-94.
15. Vaezy S, Clark JI. Quantitative analysis of the microstructure of the human cornea and sclera using 2-D Fourier methods. *Journal of Microscopy* 1994; 175 Pt 2:93-99.
16. Essenpreis M., Elwell C. E., Cope M., van der Zee P., Arridge S. R., Delpy D. T. Spectral dependence of temporal point spread functions in human tissue," *Applied Optics* 1993; 32, 4:418-425.

Damage Mechanisms of Pico- and Femtosecond Laser Retinal Lesions as Viewed by Electron Microscopy

Cynthia A. Toth^a, Eric K. Chiu^a, J. Michael Jumper^a, Benjamin A. Rockwell^b

^aDuke University Medical Center, Durham, NC 27710

^bArmstrong Laboratory, Brooks AFB, TX 78235-5215

ABSTRACT

Retinal lesions produced by ultrashort laser pulses in the pico- and femtosecond range were examined by electron microscopy. Retinal pigment epithelial (RPE) cells that contained fractured and striated melanosomes typically exhibited severe damage to the other components of the cell. However, having observed RPE cell damage without coincident fractured melanosomes, it is thought that melanosome fracture itself is not responsible for the damage that occurs within the RPE cell. Nevertheless, the percentage of melanosomes fractured per lesion seems to parallel the severity of damage within that lesion site. No trend existed between percentage of melanosomes fractured and the peak power of laser delivery. However, with decreasing laser pulselength, there was a decrease in the percentage of melanosomes showing fracture.

Keywords: retinal pigment epithelium, laser, picosecond, femtosecond, laser induced breakdown, electron microscopy, Bruch's membrane

1. INTRODUCTION

As the prevalence of ultrashort laser systems increases in research and industry, safety standards must be established based upon a clear understanding of their potential for harmful interaction with human tissue. Furthermore, by clarifying the mechanisms of damage through with these technologically advanced laser systems act, one may discover potentially therapeutic applications.

2. PREVIOUS STUDIES

In 1987, Birngruber et al.¹ concluded that, in a manner similar to previous longer wavelength systems, the energy of ultrashort laser pulses was absorbed in large part by the melanin pigment contained within the retinal pigment epithelium. After producing visible lesions in grey chinchilla rabbits, they found that no lesions could be detected ophthalmoscopically or with fluorescein angiography when applying ultrashort pulses to the eyes of nonpigmented albino rabbits. Goldman et al.² conducted studies of 30 ps pulses and theorized that damage was due in large part to acoustic (elastic) and shock (inelastic) waves generated by a very sharp temperature gradient between the absorbing melanin granule and its surroundings. They felt that these shock waves caused mechanical damage to membranes, and could thus lead to cell death. Roider et al.³ theorized that a single pulse in the femtosecond range has such short time for energy deposition (i.e. the pulse duration is well below the thermal relaxation time) that there is a small window of opportunity for thermal spread. Consequently, the site of the lesion remains confined. Cain et al.⁴ reported that self-focusing and laser induced breakdown (LIB) were possible factors in the damage mechanism by concluding that ultrashort laser pulses would reach a "flash" endpoint at which LIB would occur and a plasma would be formed. With expansion of the plasma, a supersonic shock wave and cavitation bubble would be generated and could lead to damage of the surrounding retina. They also stated that during such an event, this cavitation bubble could collapse and re-expand a number of times. Using strobe illumination and a high speed camera, Kelly and Lin⁵ were able to capture images of this transient bubble formation inside RPE cells. Below LIB threshold however, it is thought that the mechanism of damage results from thermal deposition of energy into melanosomes with subsequent steam bubble formation within the RPE cell. Gerstman et al.⁶ proposed that the temperature rise at the melanosome causes vaporization of the immediate surrounding medium, thus creating a bubble that expands outward. In a light microscopy study, Toth et al.⁷ further explored these issues by examining ultrashort laser lesions with the light microscope. They found that with the use of femtosecond pulses, a narrow column of damage was formed within the retina at lower energies than with picosecond pulses. This supported the concept proposed by Cain et al.⁴ that LIB occurred within a narrow site of plasma formation when ultrashort pulses are utilized.

3. PURPOSE

This report is focused upon establishing the relationships between laser energy/pulsewidth and the electron microscopic appearance of the lesion at the level of retinal pigment epithelial (RPE) cells, Bruch's membrane, and choroidal vessels; paying particular attention to the effects on melanosomes and the RPE/Bruch's membrane interface.

4. METHODS

The treatment and procedures used in this study conformed to the Use of Animals in Ophthalmic and Vision Research and Federal Guidelines. Animals involved in this study were procured, maintained, and used in accordance with the recommendations of the NIH "Guide for the Care and Use of Laboratory Animals" (National Institute of Health Publication No. 85-23, revised 1985) the Office of Protection from Research Risk "Public Health Service Policy on Humane Care and Use of Laboratory Animals" (revised 1986), and the Animal Welfare Act.

Two mature *Macaca mulatta* weighing 3-4 kg were maintained under standard laboratory conditions with monitoring and care during laser lesion placement, enucleation, and euthanasia as previously described. (Cain et al.⁸) Single laser pulses with a range of energies from 0.58-9.50 uJ were delivered in a 3X3 grid to the macular area of each of three eyes at one of the three laser pulsewidths: 90 fs, 3ps, or 60 ps pulses as previously described by Cain et al.⁸ All laser energies reported in this study were the energies delivered to the cornea and measured as a percentage of beam delivered to a beam splitter. Of the 27 retinal laser lesions contained within the three macular grids, twelve sites were processed for TEM evaluation. Of these twelve, four sites were produced by 60ps laser pulses, five sites from 3ps pulses, and three sites from 90 fs pulses.

The eyes were incised anterior to the equator and immersed in a 3% gluteraldehyde and 0.1M sodium cocodylate buffer immediately following enucleation. The posterior eye cup was cut away from the anterior segment after 10 minutes and replaced in the fixative. The macular area was later dissected and embedded in Spurr's resin. Sections of approximately 60 nm thickness were obtained from the region of laser delivery. Each section was stained with 2% uranyl acetate and Sato Lead Stain.

Each laser lesion was examined using an electron microscope (JEM-1200EX, JEOL, Peabody, MA) at 800 - 6000X magnification. Photographs of these high magnification images were taken with the microscope's camera and arranged in a montage for each lesion site.

Upon examination, particular notice was paid to the general appearance of the RPE cells, the occurrence of fractured or striated melanosomes, the integrity of Bruch's membrane, and whether or not hemorrhage or coagulation had occurred within the choriocapillaris. A fractured melanosome was defined as any melanosome with clear evidence of rupture. (see figure, black arrow) The number of fractured melanosomes per lesion site was counted and expressed as a ratio over the total number of melanosomes per lesion site. A melanosome was designated as striated if it had a striped appearance and lacked the homogenous electron density that normally appears on TEM. (see figure, white arrow) Melanosomes without obvious fracture but alterations in their normally uniform contour were also noted and deemed irregular.

5. RESULTS

Severe damage to retinal pigment epithelial cells was observed in 9 of 12 lesions. At 1 hour after laser delivery, these included the disappearance of apical microvilli (7/12), condensation of nuclear material (9/12), "smudged" appearance of cytoplasm (likely resulting from denaturation of cellular protein material) (9/12), and the formation of vacuoles in the basal region of the RPE cells(9/12). (see figure) At 24 hours after laser delivery, these same findings were observed along with an apparent "stacking" of RPE cells. The swelling and vacuolization of mitochondria at the base of all RPE cells may not have been the direct result of laser exposure but rather was likely due to expected cell degeneration during time of experimentation prior to fixation.

RPE cells show a characteristic "lifting off" of Bruch's membrane in all of the 90fs lesions. This separation is characterized by the RPE cell becoming detached with the basal lamina of the RPE and zonula occludens remaining intact. It appears that it is the basal infolding that is disrupted because remnants of the basal infolding are visible atop the intact basal lamina. The 3ps and 60ps lesions did not show this same separation but did demonstrate mild elevation of the RPE cell,

perhaps from due to basal vacuole formation. With 3ps lesions, only the highest energy lesion was clearly elevated (1/5). Conversely, with 60ps lesions, all but the highest energy lesion were elevated above Bruch's membrane (3/4).

Fractured melanosomes were found in 9 of the 12 lesions. It should be noted that these were not the same aforementioned 9 lesions in which RPE cell damage was observed. Fractured melanosomes appeared in the apical region more frequently while none were found basally. Striated melanosomes, which were visible in 9 of 12 lesions, were typically found centrally, with a few seen apical and basal. Irregular melanosomes were seen in 7 of 12 lesions.

No apparent relationship was found between melansome fracture and peak power. The highest percentage of fractured melanosomes (36.4%) was seen in a lesion created with the lowest peak power (3.77×10^4 W), while no fractures were seen in select lesions produced with higher peak powers (1.93×10^5 - 1.05×10^6 W). The lesion produced with the highest peak power (2.71×10^7 W) contained a midrange percentage of fractures (6.3%).

A trend did exist between melansome fracture ratio and decreasing laser pulselength. As the pulselength decreased, the percentage of melanosomes showing fracture also decreased. The highest percentage of fractures were found in 60ps lesions (12.0%), then in 3ps lesions (6.2%), and the least in 90fs lesions (4.6%). A similar trend was seen with the mean percentages of striated melanosomes.

There was no evidence of disruption of Bruch's membrane in any of the 12 lesions. Furthermore, no hemorrhage from the choroidal circulation was seen. The clumping of erythrocytes within choroidal capillaries seen in segments of 3ps lesions was thought to be artifact introduced during specimen handling.

6. DISCUSSION

Fractured melanosomes were seen in 9 of 12 lesions, but as noted, not the same 9 lesions in which severe RPE cell injury was found. Glickman et al.⁹ theorized that melansome fracture resulted in a release of melanin radicals which could cause oxidative damage to cell proteins and act as a prerequisite event to cell death. The appearance of cell injury without corresponding melansome fracture, as well as the observation of a fractured melansome within an RPE cell that showed almost no signs of damage, dispute this hypothesis that fracture must occur. Nevertheless, our results support the relationship between melansome fracture and the extent of damage within the RPE cell itself. In other words, the percentage of fractured melanosomes parallels the severity of the lesion and laser pulses that are likely to produce a high percentage of fractured melanosomes also induce severe damage to the rest of the RPE cell.

Striated melanomes were found within 9 of 12 lesions. Breathnach et al.¹¹ previously described striated melanosomes as those still undergoing progressive melanization; whereas mature melanin granules were "practically uniformly electron opaque". In 1975, Goldman et al.² described melanosomes with similar features resulting from ultrashort laser damage. They theorized that "the energy not involved in the temperature rise at the surface of the melanin would be available to break the cross linkages between the fibers upon which the melanin was deposited in the developing melansome. The breakage of these bonds would separate and expose the fibers, and produce a striated appearance...". In our study, a few striated melanosomes were observed in the control micrograph of normal RPE, taken a distance away from laser delivery. One possible explanation for this observation is a species variation between humans and other primates. However, no electron micrographs from previous publications regarding monkey RPE were found to show striated melanosomes such as these. It is also possible that the tissue removed as "normal control" was not adequately distant from the sites of laser lesions and therefore cannot be thought of as a pure control.

Irregular melanosomes with apparent shape alterations were seen in 7 of 12 lesions. Lacking any systematic pattern of appearance, melanosomes with irregular contour alterations do not seem to represent a specific type of ultrastructural melansome. Rather, they are merely the consequence of the level of resolution and the two dimensional restrictions of histological sectioning and imaging and are therefore of little significance. It is also possible that these irregularly shaped melanosomes represent artifact that is introduced in the processing of the tissue specimens.

Finding no breaks in Bruch's membrane was expected since the previous light microscope study (Toth et al.⁷) had not seen any bleeding from the choroidal circulation. Several previous studies of laser effects found extensive retinal and RPE

damage and yet observed no damage to Bruch's membrane. (Birngruber et al.¹; Courant et al.¹⁰; Roider et al.¹¹; Wallow et al.¹²; Marshall et al.¹³)

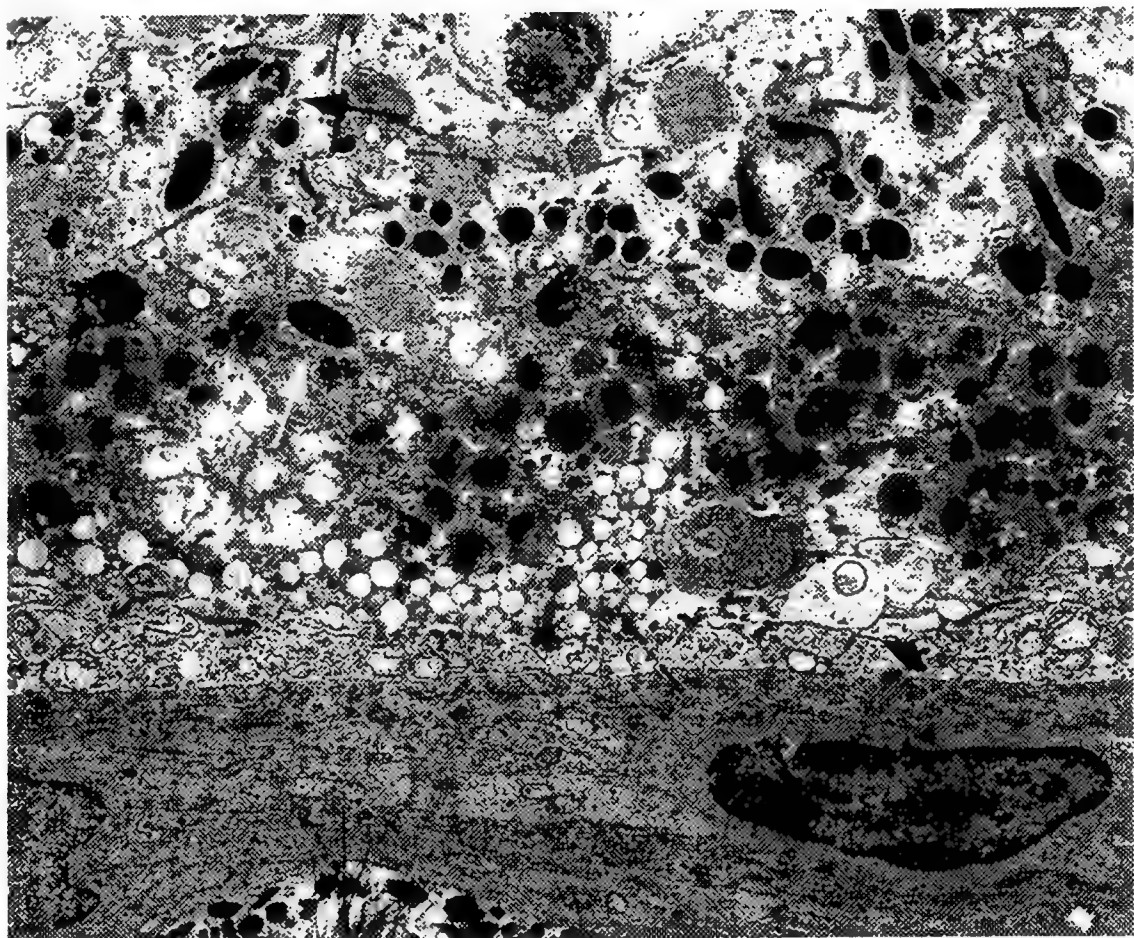
The appearance of a characteristic detachment of RPE cells above Bruch's membrane in 90fs lesions supports the concept of a cavitation bubble forming and receding immediately after laser irradiation at energies above LIB threshold. Such phenomena could generate physical forces that would lead to this "lifting off" of RPE cells. Goldbaum et al.¹⁴ reported that adhesion between basal lamina and basal infolding was stronger than the integrity of the RPE cell itself. Thus, in order to produce the observed detachment, some force must have acted within or above the RPE cells. This is again consistent with the concept of a rapidly forming and degenerating cavitation bubble forming within the RPE cell upon laser irradiation.

7. ACKNOWLEDGEMENTS

This work was supported by AFOSR Grants: 2312AA-92AL014 and F49620-95-1-0226 and Contract F33615-92-C-0017.

8. REFERENCES

1. Birngruber R, Puliafito CA, Gawande A. Femtosecond Laser-Tissue Interactions: Retinal Injury Studies. *IEEE J of Quantum Electron.* 1987;QE-23,10:1836-1844
2. Goldman AI, Ham WT, Mueller HA. Mechanisms of Retinal Damage Resulting from the Exposure of Rhesus Monkeys to Ultrashort Laser Pulses. *Exp Eye Res.* 1975;21:457-469
3. Roider J, Hillenkamp F, Flotte T, Birngruber R. Microphotocoagulation: Selective effects of repetitive short laser pulses. *Proc Natl Acad Sci USA* 1993;90:8643-8647
4. Cain CP, DiCarlo CD, Rockwell BA, et al. Retinal Damage and Laser-induced Breakdown Produced by Ultrashort-pulse Lasers. *Graefes Arch Clin Exp Ophthalmol.* 1996;234:S28-S37
5. Kelly MW, Lin CP. Microcavitation and Cell Injury in RPE Cells Following Short-Pulsed Laser Irradiation. *Proc Society Photo-Optical Instrumentation Engineers, Laser Tissue Interaction VII.* 1997;174-179
6. Gerstman BS, Thompson CR, Jacques SL, Rogers ME. Laser Induced Bubble Formation in the Retina. *Lasers Surg Med.* 1996;18:10-21
7. Toth CA, Narayan DG, Cain CP, et al. Pathology of Macular Lesions from Subnanosecond Pulses of Visible Laser Energy. *Invest Ophthalmol Vis Sci.* 1997;38:2204-2213
8. Cain CP, Toth CA, DiCarlo CD, et al. Visible Retinal Lesions From Ultrashort Laser Pulses in the Primate Eye. *Invest Ophthalmol Vis Sci.* 1995; 36:879-888
9. Glickman RD, Jacques SL, Schwartz JA. Photodisruption increases the free radical reactivity of melanosomes isolated from retinal pigment epithelium. *Proc Society Photo-Optical Instrumentation Engineers, Laser Tissue Interaction VII.* 1996;460-467
10. Courant D, Fritsch P, Naudy-Vives C, et al. Histological Study of Retinal Damages Induced by Multiple Picosecond Pulses. *Proc Internat Laser Safety Conf.* 1997;132-137
11. Roider J, Michaud NA, Flotte TJ, Birngruber R. Response of the Retinal Pigment Epithelium to Selective Photocoagulation. *Arch Ophthalmol.* 1992;110:1786-1792
12. Wallow IHL, Lund OE, Gabel VP, Birngruber R, Hillenkamp F. A Comparison of Retinal Argon Laser Lesions in Man and in Cynomolgus Monkey. *Albrecht Von Graefes Arch Klin Exp Ophthalmol* 1974;189:159-164
13. Marshall J, Hamilton AM, Bird AC. Histopathology of ruby and argon laser lesions in monkey and human retina. *Br J Ophthalmol.* 1975;59:610-630
14. Goldbaum MH, Madden K. A New Perspective on Bruch's Membrane and the Retinal Pigment Epithelium. *Br J Ophthalmol.* 1982;66:17-25



Transmission electron micrograph of laser lesion in retinal pigment epithelium

SESSION 4

Ablation with Ultrashort-Pulse Lasers: Surgical Applications

Ultrashort laser pulses in dentistry: advantages and limitations

Markolf H. Niemz

Universität Heidelberg, Institut für Angewandte Physik
Albert-Ueberle-Str. 3-5, 69120 Heidelberg, Germany

Invited paper

ABSTRACT

Several laser systems are currently under investigation for the purpose of removing hard dental tissues. However, either undesired thermal side effects or the lack of efficiency have already been demonstrated in most cases. In this paper, advantages and limitations of using ultrashort laser pulses with either picosecond or femtosecond durations are discussed. The major advantages associated with these pulse durations is the ability to produce very precise cavities without significant thermal side effects. Even disruptive effects due to shock wave generation seem to be negligible at moderate pulse energies close to the ablation threshold. The quality of these cavities is found to be superior to the quality achievable with other laser systems. Moreover, a spectroscopical analysis of the laser-induced plasma sparks enables an on-line health diagnosis of the irradiated volume. Limitations arise from the development of a suitable delivery system and from the cost of generating ultrashort laser pulses.

1. INTRODUCTION

Since the early stage of laser development several attempts have been made to apply this tool for certain procedures in dentistry, as well. However, no satisfying solution has yet been provided for one of its most demanding applications: the usage of lasers in the therapy of dental decay. Replacing or supporting conventional drilling machines by lasers in order to achieve a more accurate and painless treatment of dental decay has been a challenge for the past decades. Since pain is usually caused by vibration and heat due to friction, it can be avoided by using a contactless operating laser that is working in the "cold" ablation range. Usually continuous wave (cw) lasers and pulsed lasers with pulse durations down to the microsecond range generate a lot of heat in the region of the pulp chamber during the ablation process. This is due to the fact that in this time frame of pulse duration heat diffusion plays a very important role in the interaction mechanism.¹ The first lasers used in dentistry are representatives of this group: these are the ruby lasers introduced by Stern and Sognnaes², and Goldman et al.³, as well as the CO₂ lasers investigated by Stern et al.⁴ and Frame.⁵ They show very strong thermal side effects, since the temperature increase in the inner tooth reaches values higher than 10⁰ C, thereby injuring the pulp.

Meanwhile several experiments have been performed using alternative laser systems. Among these are the Er:YAG laser and excimer lasers, especially the ArF excimer laser. The Er:YAG laser was first used in dentistry by Hibst and Keller.⁶ The wavelength of the Er:YAG laser at 2.94 μm matches the resonance frequency of the vibrational oscillations of water molecules contained in the teeth, thereby strongly enhancing the absorption of Er:YAG radiation. The absorption leads to small microexplosions breaking the hydroxyapatite structure. The coincidence of thermal and mechanical ablation effects has led to the term "thermomechanical" interaction.⁷ However, as reported by Niemz et al.⁸ and Frentzen et al.,⁹ cracks up to 300 μm deep may be induced by this type of interaction that can potentially be the origin for new caries development. Liesenhoff et al.¹⁰ found that the ArF laser at a wavelength of 193 nm shows only very little thermal side effects. Heat induced ruptures are reduced due to the shorter pulse duration of typically 15 ns. However, the ablation rate, i.e. the ablated volume per pulse, is very low according to Rechmann et al.¹¹ This ineffectiveness and the general risks of UV radiation are the major disadvantages concerning its use in dentistry, although it may be of importance for other medical applications.

A new approach was made by Niemz et al.⁸ when first applying picosecond laser pulses to dental applications. In this so-called plasma-induced ablation,¹² a localized microplasma is induced at the laser focus. With pulse durations of a few picoseconds, pulse energies up to 1 mJ and a focal spot size of about 30 μm the power density at the focus reaches values $> 10^{11} \text{ W/cm}^2$. Hence, the amplitude of the electric field exceeds 10^7 V/cm and optical breakdown occurs. The ionized material is ablated, and thermal as well as mechanical damage is negligible when using pulse energies close to the threshold of plasma ignition. Recently, a further step forward was made when using femtosecond lasers to ablate hard dental tissues.¹³⁻¹⁶ In general, the results of these studies show great promise that the initial difficulties of "laser dentistry" can finally be overcome when choosing the correct laser parameters, since femtosecond pulses as well as picosecond pulses produce ablations superior in quality to those achievable by longer pulse durations. The question remains whether these highly sophisticated ultra-short pulse laser systems – usually consisting of an oscillator laser and a regenerative amplifier – will be able to form a marketable alternative to conventional drilling machines.

2. MATERIALS AND METHODS

The picosecond laser system.

The Nd:YLF laser system is designed as a two stage combination (Fig. 1), consisting of a laser oscillator and a regenerative amplifier, to provide laser pulses with durations down to 30 ps and energies up to 1 mJ at a wavelength of 1053 nm. The oscillator Nd:YLF rod is pumped by a temperature tuned 1 Watt diode laser (DL) using beam shaping and collimating optics (CO). The Nd:YLF crystal itself is coated with a high reflecting mirror on the surface pointing to the diode laser. An acousto-optic mode locker (AOM) is placed near the flat 10 % output coupler (OC). For active amplitude modulation an amplified 80 MHz signal is applied to this device, generating a train of short laser pulses with typical durations of 25 ps each. A real-time autocorrelation system allows continuous supervision of the pulse width. For the purpose of selecting the 1053 nm transition, a Brewster polarizer (BP) is added to the cavity. At the half-wave plate (HWP) the 160 MHz pulse train, consisting of 0.2 nJ pulses, experiences

a 90° rotation of the polarization vector. Using a 4 % reflecting mirror (M3) and a polarizing beam splitter, the oscillator pulses are then injected into the regenerative amplifier unit described by Bado et al.¹⁷ The 76 mm amplifier Nd:YLF rod is pumped by a single flashlamp, controlled by a standard laser power supply (model 204A, Quantronix Inc.). The cavity employs two highly reflecting mirrors with a radius of curvature of 1 m each. Applying a 2 kV voltage signal with up to 1 kHz repetition rate to a LiNbO₃ Pockels cell (PC) provides half-wave retardation per round-trip. In combination with the double-pass half-wave retardation of the intracavity quarter-wave plate (QWP), a selected oscillator pulse is seeded and trapped in the amplifier unit. The driving of the Pockels cell is synchronized to the mode locking process by feeding the 80 MHz signal into a special divider and timer logic. After about 100 roundtrips in the cavity the seeded pulse reaches its saturation limit. The pulse energy can be boosted up to 1 mJ, corresponding to an amplification of 10^6 of the oscillator output energy. Installation of an aperture (A) restricts the laser operation to the fundamental TEM₀₀ mode. At maximum gain the Pockels cell driver switches back to 0 V, causing no retardation. The polarization vector is now rotated by 90° as the pulse double-passes the quarter-wave plate and the Pockels cell in the left part of the cavity. Consequently, the amplified pulse is then reflected at the polarizing beam splitter and dumped out of the regenerative amplifier. Mirror M3 is now transmitting 96 % of the amplified pulse energy. Using mirror M4, the pulse train is finally injected into the application unit. Autocorrelation of these pulses shows that their pulse duration has slightly increased to about 30 ps due to dispersion inside the amplifier cavity.

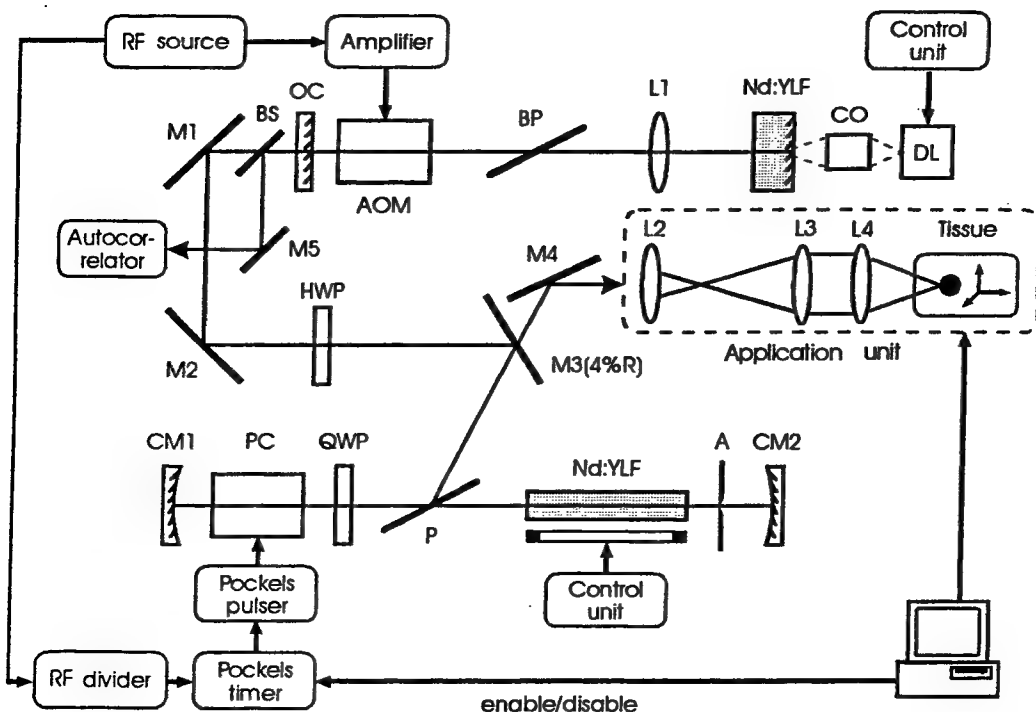


Fig. 1: The picosecond Nd:YLF laser.

For the sake of automating these experiments an application unit was developed. This device consists basically of delivering optics and a computer controlled three-axes translation stage. After expanding the Nd:YLF laser beam four times by the lenses L2 and L3, it is tightly focused onto the tissue sample by the lens L4. This focusing lens is made of SiO_2 and has a focal distance of 100 mm. The focus spot is measured with the knife edge method and has a diameter of about $30 \mu\text{m}$. Stepping motors connected to the translation stage allow precise spot-to-spot movements of the tissue within $1 \mu\text{m}$. A software package gives the user a choice of different ablation patterns. Primarily, square geometries have been selected.

The femtosecond laser system.

In order to investigate the effects of femtosecond laser pulses on hard dental tissues, a Ti:Sapphire laser source (model Spitfire, Spectra-Physics) was used. This laser is able to emit laser pulses with durations of 130 fs at a central wavelength of 780 nm. For these studies, the pulse energy is adjusted to $50 \mu\text{J}$ at a repetition rate of 1 kHz. The laser beam is focused to a spot of $30 \mu\text{m}$ in diameter. The studies on human enamel with this laser system were performed at the Laserzentrum Hannover by the order of Dr. med. A. Kasenbacher (Traunstein, Germany).

Diagnostic system.

For the purpose of analyzing dental decay, a spectroscopical arrangement was set up as shown in Fig. 2. The laser-induced plasma spark is optically imaged onto the entrance pupil of a spectrometer. The readout of the photomultiplier tube (PMT) is triggered by the laser pulses. The spectra are recorded between 400 nm and 600 nm. A BBO crystal is used to normalize the relative intensities at the wavelength of the second harmonic of the laser.¹⁸

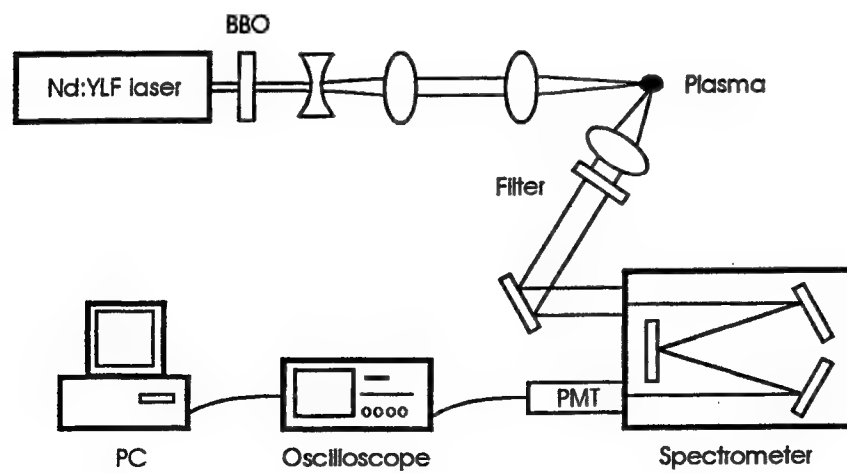


Fig. 2: Spectroscopy of laser-induced plasma sparks.

Tooth preparation.

The teeth were obtained from the Dental School of the University of Heidelberg with a protocol approved by an institutional review board. The molars were always kept in humid environment to avoid cracking due to dryness. Artificial caries was prepared according to Silverstone¹⁹ by using synthetic saliva containing 1 % hydroxymethylcellulosis buffered at pH 4.8 with acetic acid. After the ablation experiments the teeth were dried in the vacuum chamber of an exsiccator and coated with a 30 nm thick gold layer. The morphologic changes induced by the laser radiation were studied using a scanning electron microscope (model 1810, Amray Inc.).

3. RESULTS

Figures 3a-b show scanning electron micrographs (SEM) of cavities generated by the Nd:YLF picosecond laser. Fig. 3a represents a cavity ablated in sound enamel, whereas Fig. 3b shows a cavity within artificial caries. Both cavities have lateral dimensions of $1 \times 1 \text{ mm}^2$ and a depth of about $400 \mu\text{m}$. They were created by distributing 1 mJ laser pulses onto 40 lines over the tooth surface with 400 laser spots per line, and repeating this procedure ten times for the cavity in Fig. 3a and once for the cavity in Fig. 3b. Thus, a total number of 160 000 laser shots was necessary for the cavity in sound enamel and only one tenth of this number was needed to generate the cavity in carious enamel. Hence, at a pulse energy of 1 mJ and a repetition rate of 1 kHz, a cavity as shown in Fig. 3a is ablated within a total time of 160 seconds. Therefore, the efficiency for removing sound enamel with the described laser system is about 0.15 mm^3 per minute and millijoule. By contrast, the cavity shown in Fig. 3b requires a duration of only 16 seconds and is characterized by an efficiency of 1.5 mm^3 per minute and millijoule, respectively. Both cavities have a very precise geometry, and especially the edges are very clean and sharp. The bottom surfaces of cavities within sound enamel are slightly rougher than the surfaces in carious enamel. The overall roughness is of the order of $10 \mu\text{m}$ and ideally suited for most filling materials.

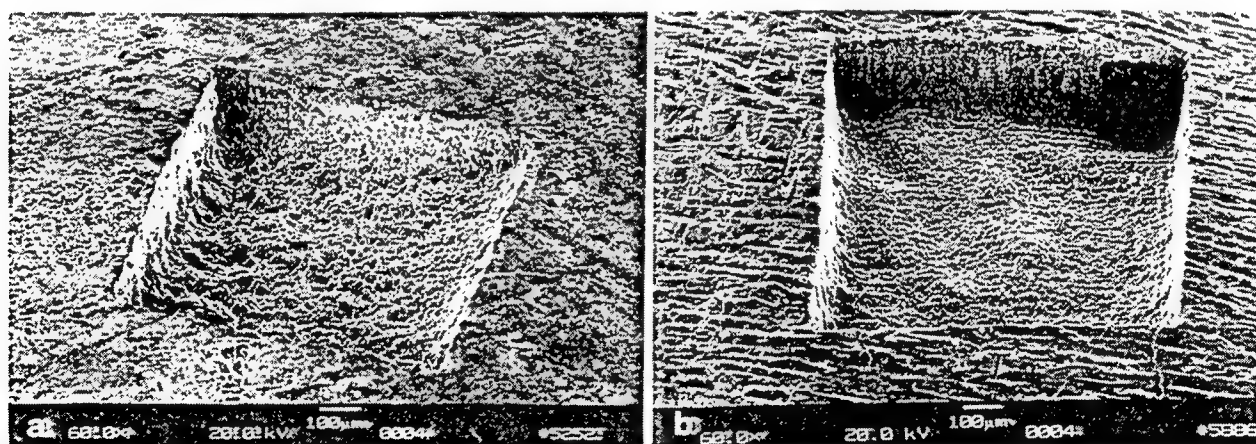


Fig. 3: Sound enamel (a) and carious enamel (b) ablated with the Nd:YLF picosecond laser.

By contrast, Fig. 4 shows a cavity in a human tooth produced by the Ti:Sapphire femtosecond laser. The cavity has lateral dimensions of approximately $1 \times 1 \text{ mm}^2$ and a depth of about $315 \mu\text{m}$. It was created by distributing 12 scans over the tooth surface with a total of approximately two million pulses at an energy of $50 \mu\text{J}$ each. Therefore, the efficiency for removing sound enamel with this femtosecond laser system is about 0.18 mm^3 per minute and millijoule.

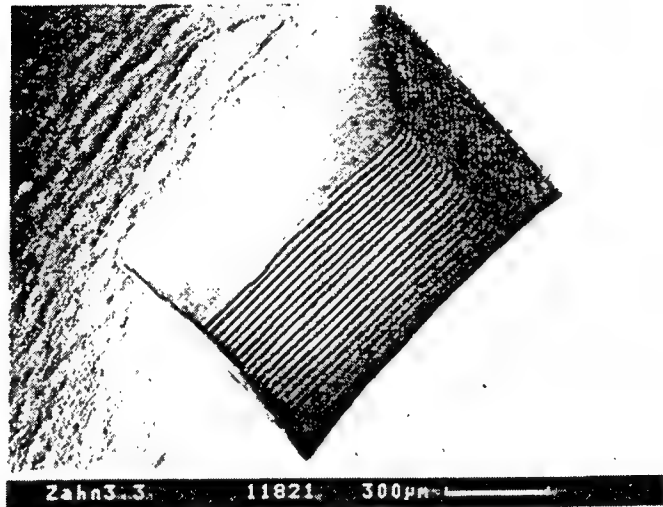


Fig. 4: Sound enamel ablated with the Ti:Sapphire femtosecond laser.

The results of plasma spectroscopy are summarized in Figs. 5a-b. Typical spectra obtained from plasma sparks on either sound enamel (Fig. 5a) or carious enamel (Fig. 5b) are shown. Due to the demineralization associated with dental decay, a strong decrease in intensity of the calcium transitions becomes apparent.

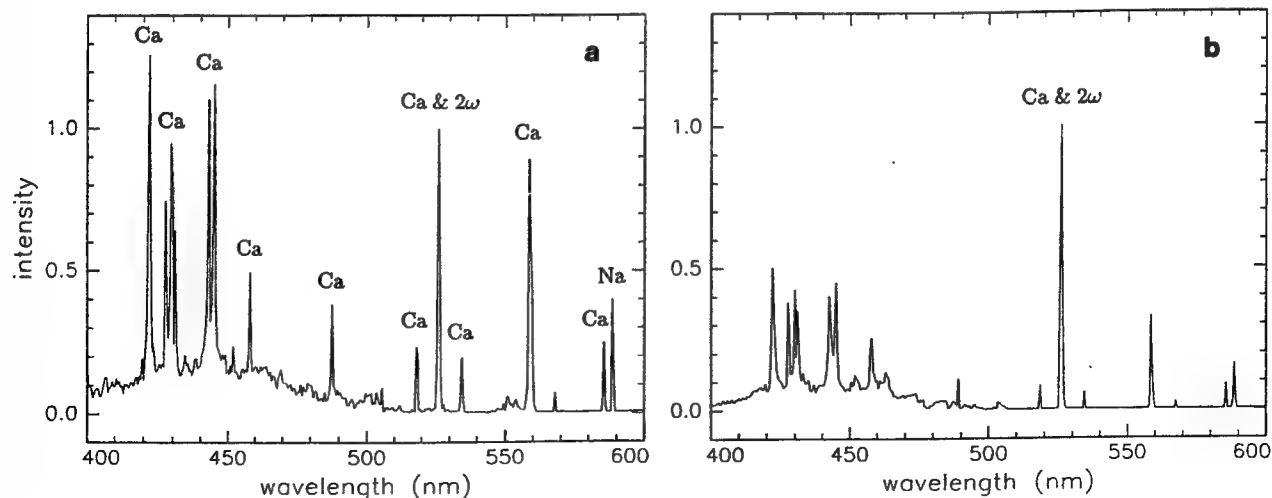


Fig. 5: Plasma spectrum of sound enamel (a) and carious enamel (b).

4. DISCUSSION

The ablation experiments performed with both the Nd:YLF picosecond laser and the Ti:Sapphire femtosecond laser prove that cavity preparation is possible with ultrashort laser pulses without inducing severe thermal or mechanical damage. This is a little surprising, because deep cracks inside the tooth due to shock wave generation were predicted by Frentzen and Koort,⁷ when using ultrashort laser pulses. Such shock wave effects were observed indeed, when focusing the Nd:YLF laser onto 90 μm thick microscope glass plates as reported by Pioch et al.²⁰ However, no tooth alterations due to shock waves – like cracking or structural changes – have been observed so far when applying moderate pulse energies close to the ablation threshold. These observations can probably be attributed to the different morphologic structures of glass and teeth. Acoustic waves are strongly damped by the organic matrix of teeth, while glass easily splinters when being exposed to high pressure waves.

The reproducibility of clean and regularly shaped cavity preparation in teeth with both picosecond and femtosecond lasers is very high, since the cavities obtained in all teeth investigated were of a similar high quality. Hence, strong experimental evidence is given that these lasers are suitable for clinical applications. The observed roughness of the cavity bottoms should enable a proper adhesion of filling materials.

When discussing the limitations of a new technique, one should first look at potential delivery systems. For a clinical application of the lasers discussed above, optical fiber delivery and/or an even faster scanning mirror device need to be developed. When aiming at treatment durations comparable to the conventional drill, energy outputs of a few hundred microjoules at repetition rates of up to 10 kHz should be sufficient for clinical applications. Both Nd:YLF and Ti:Sapphire lasers with repetition rates of 5 kHz and higher are already commercially available. Another limitation is the cost of such highly sophisticated laser systems. Laser therapy alone might not justify more expensive treatment costs. However, the present paper indicates that the mechanism of plasma-induced ablation enables *selective* removal of dental decay, as well. On the one hand, the ablation rate of dental decay is higher than that of sound enamel. On the other hand, the generated plasma spark can be spectroscopically analyzed in real-time. With this additional option a computer controlled picosecond or femtosecond laser system could possibly decide in the near future, whether all dental decay has been removed or not, thereby minimizing the amount of hard dental tissue to be ablated. Since the cavity size is then reduced – even after a refilling –, the number of indications for a dental crown or prothesis might decline. In these cases, i.e. when the advantages of minimally invasive surgery become significant, the problem of cost might be overcome.

5. ACKNOWLEDGEMENTS

The author gratefully acknowledges Dr. med. A. Kasenbacher in Traunstein, Dr. T. Pioch at the Dental School of the University of Heidelberg, and Dr. C. Momma from the Laserzentrum Hannover for their contributions to the results of this study.

6. REFERENCES

1. J. L. Boulnois, "Photophysical processes in recent medical laser developments", *Lasers Med. Sci.* **1**, pp. 47–66, 1986.
2. R. H. Stern, R. F. Sognnaes, "Laser beam effect on dental hard tissues", *J. Dent. Res.* **43**, p. 873, 1964.
3. L. Goldman, P. Hornby, R. Mayer, B. Goldman, "Impact of the laser on dental caries", *Nature* **203**, p. 417, 1964.
4. R. H. Stern, J. Vahl, R. F. Sognnaes, "Lased enamel: ultrastructural observations of pulsed carbon dioxide laser effects", *J. Dent. Res.* **51**, pp. 455–461, 1972.
5. J. W. Frame, "Carbon dioxide laser surgery for benign oral lesions", *Br. Dent. J.* **158**, pp. 125–128, 1985.
6. R. Hibst, U. Keller, "Experimental studies of the application of the Er:YAG laser on dental hard substances", *Lasers Surg. Med.* **9**, pp. 338–344, 1989.
7. M. Frentzen, H. J. Koort, "Lasertechnik in der Zahnheilkunde", *Dtsch. Zahnärztl. Z.* **46**, pp. 443–454, 1991.
8. M. H. Niemz, L. Eisenmann, T. Pioch, "Vergleich von drei Lasersystemen zur Abtragung von Zahnschmelz", *Schweiz. Monatsschr. Zahnmed.* **103**, pp. 1252–1256, 1993.
9. M. Frentzen, C. Winkelsträter, H. van Benthem, H. J. Koort, "Bearbeitung der Schmelzoberflächen mit gepulster Laserstrahlung", *Dtsch. Zahnärztl. Z.* **49**, pp. 166–168, 1994.
10. T. Liesenhoff, T. Bende, H. Lenz, T. Seiler, "Grundlagen zur Anwendung des Excimer-Lasers in der Zahnheilkunde", *Dtsch. Zahnärztl. Z.* **45**, pp. 14–16, 1990.
11. P. Rechmann, T. Hennig, R. Kaufmann, "Laser in der Zahnhartsubstanzabtragung", *Zahnärztl. Welt* **101**, pp. 150–160, 1992.
12. M. H. Niemz, "Laser-tissue interactions: fundamentals and applications", Springer-Verlag, Berlin Heidelberg New York, 1996.
13. C. Momma, S. Nolte, H. Welling, A. Kasenbacher, M. H. Niemz, "Ablation von Zahnhartsubstanz mit ps- und fs-Laserpulsen", *Proc. Laser 97*, München, 1997.
14. J. Neev, L. B. da Silva, M. Feit, M. Perry, A. M. Rubenchik, B. C. Stuart, "Ultrashort pulse laser system for hard dental tissue procedures", *Proc. SPIE* **2672**, pp. 210–221.
15. A. M. Rubenchik, L. B. da Silva, M. Feit, S. Lane, R. London, M. Perry, B. C. Stuart, J. Neev, "Dental tissue processing with ultra-short pulse laser", *Proc. SPIE* **2672**, pp. 222–320.
16. J. Neev, "Preliminary characterization of hard dental tissue ablation with a femtosecond laser", – these proceedings.
17. P. Bado, M. Bouvier, J. S. Coe, "Nd:YLF mode-locked oscillator and regenerative amplifier", *Optics Lett.* **12**, pp. 319–321, 1987.
18. M. H. Niemz, "Investigation and spectral analysis of the plasma-induced ablation mechanism of dental hydroxyapatite", *Appl. Phys. B* **58**, pp. 493–499, 1994.
19. L. M. Silverstone, "Primary translucent zone of enamel caries and of artificial caries-like lesions", *Brit. Dent. J.* **120**, pp. 461–471, 1966.
20. T. Pioch, M. H. Niemz, A. Mindermaier, H. Staehle, "Schmelzablitionen durch Laserimpulse im Pikosekundenbereich", *Dtsch. Zahnärztl. Z.* **49**, pp. 163–165, 1994.

Plasma luminescence feedback control system for precise ultrashort pulse laser tissue ablation

B.-M. Kim, M. D. Feit, A. M. Rubenchik, D. M. Gold, C. B. Darrow, J. E. Marion,
L. B. Da Silva

Lawrence Livermore National Laboratory
Livermore, CA, 94550

ABSTRACT

Plasma luminescence spectroscopy was used for precise ablation of bone tissue without damaging nearby soft tissue using an ultrashort pulse laser (USPL). Strong contrast of the luminescence spectra between bone marrow and spinal cord provided the real time feedback control so bone tissue is selectively ablated while preserving the spinal cord.

Keywords : ultrashort pulse laser, plasma, luminescence spectroscopy, feedback control

1. INTRODUCTION

As lasers are accepted as possible replacements for conventional surgical tools in many medical fields, a focus of research has been on more effectively removing the biological tissues while reducing mechanical and thermal damage to the surrounding tissues. Recently, many studies have shown that ultrashort pulse lasers (< 1 ps) can meet this need¹⁻⁶. In this short pulse domain, the ablation process is distinguished from the conventional longer pulse ablation which mostly depends on the photothermal heating in the media. As the pulse width becomes shorter, multiphoton ionization dominates during the ablation process which leads to the plasma optical breakdown. The plasma is ejected at a rate $\sim 10^7$ cm/s which is faster than the shock wave speed $\sim 10^6$ cm/s and the even slower heat diffusion. Therefore, the mechanical and thermal damage is minimized with these short pulses. Additionally, since the plasma is reflective and absorptive, for longer pulses such as 1 ns pulses, most of the incoming energy is reflected back or channeled into plasma heating instead of being absorbed by the tissue and used for tissue removal. On the other hand, the energy deposition time for ultrashort pulses is much shorter than the plasma expansion time and therefore the ablation is highly efficient ($\sim 1\mu\text{m}/\text{pulse}$)².

Luminescence is generated from a high temperature plasma during ablation. Strong luminescence signals for calcium based plaque in atherosclerotic tissue has been reported⁷⁻⁹. Our studies are focused on a feasibility test of using the luminescence spectroscopy as a tool for optical feedback during micro-spinal surgery where the calcium based bone tissue needs to be removed while preserving the soft nerve tissue which stems from the spinal cord. The results suggest that the hard tissue can be selectively ablated with high accuracy.

2. RESULTS AND DISCUSSIONS

Our ultrashort pulse laser ablation system consists of four separate lasers. An 82 MHz Ti-Sapphire actively mode-locked laser (Spectra Physics, Model # 3960) is pumped by a 5 W, frequency doubled Nd:YAG laser (Spectra Physics Model : Millenia) running at 532 nm. The mode-locked laser pulse has duration of 100 fs at 790 nm. Its pulse is amplified by a Ti-Sapphire regenerative amplifier (Positive Light, Model : Spitfire) through a chirped pulse amplification (CPA) process. This amplifier is pumped by a 10 W, 527 nm Nd:YLF laser (Positive Light, Model : Merlin). The final pulse duration is about 150 fs running at 1 kHz and its amplified energy is more than 1

B.-M. K. (correspondence) : E-mail : kim12@llnl.gov; Telephone : 510-423-3262; FAX : 510-424-2778

mJ/pulse at 790 nm. The ablation rate is approximately 1 mm/s using a 1 kHz beam train. The focused beam size was approximately 100 μm (FWHM) with TEM₀₀ mode.

A fresh porcine spine was frozen and cut transversely to expose the bone marrow and spinal cord. The cross section was cleaned with a soft brush to remove the debris of the soft tissue left in the bone marrow during cutting. The laser pulses were focused onto the cross sections of spinal cord and bone marrow to generate the plasma luminescence.

The luminescence signal was collected by a 1 mm diameter optical fiber and was delivered to the spectrometer and charge coupled device (CCD) camera. The source light was normally incident onto the tissue and the fiber was placed 20° from the normal direction and 5 mm away from the tissue surface. A mechanical shutter for the source laser and a CCD shutter were controlled by a pulse generator. Fig. 1 shows the luminescence spectra from both bone and spinal cord. As seen from the figure, not only the overall luminescence intensity is strong but strong calcium lines are observed from the bone luminescence spectrum. On the other hand, the luminescence from the spinal cord is much smaller and there are no calcium line features.

The overall luminescence intensity decreases as the ablation front moves deeper into the ablation hole because less ablated material is ejected and the distance between the ablation front and detector becomes larger as discussed in the previous study¹⁰. Fig. 2 shows the temporal changes of the absolute luminescence intensities integrated over each 100 shots during 1 sec, 1 kHz pulse train. As expected, the total intensity of luminescence decreases rapidly as the ablation front moves deeper into the sample while the luminescence intensity does not vary significantly for spinal cord. After the first 600 shots, the overall luminescence from spinal cord becomes stronger than that from the bone tissue. From this study, it was concluded that by comparing the luminescence ratio between 616 nm and 575 nm, we can accurately discriminate the two tissue types better than comparing the absolute intensities. The luminescence ratio between the two wavelengths is consistent for both bone and spinal cord despite the fact that the absolute intensity of the bone changes dramatically during 1000 shots as shown in Fig. 3. The ratios between these two wavelengths (616 nm/575 nm) were 4.8 (± 1.06) for bone and 1.4 (± 0.27) for spinal cord.

In a more practical setup as shown in Fig. 4, this beam was delivered and focused onto the tissue using an articulated arm which is composed of seven separate high damage threshold mirrors and one focusing lens. The luminescence signal was collected by a 200 μm optical fiber which is attached on the handpiece of the articulated arm and connected to a 1x2 fiber coupler. This signal was detected by two photomultiplier tubes (PMT) which are equipped with 616 nm and 575 nm bandpass filters respectively. To remove the intense laser source light, an additional short wave pass filter with cut-off wavelength at 650 nm were added to each PMT's providing optical density of 7 for the source light. The typical luminescence signals for these two detectors are shown in Fig. 5(a) for bone and in Fig. 5(b) for spinal cord. The initial strong peak corresponds to the laser source light which is too strong to be filtered even by the OD 7 filters. Each detected signal was gated and integrated immediately after the strong laser signal so that only the plasma luminescence is collected. The integrated signal was compared in a computer and a TTL signal was generated to determine if the tissue is bone or spinal cord and to control the laser shutter. When the laser hit the spinal cord, the computer sends an "off" signal to the mechanical shutter to close it. After the ablation stops, the shutter reopens in 0.5 sec so that the surgeon can keep ablating the bone.

Since luminescence spectroscopy requires a small fraction of the tissue to be ablated, it is of concern how to minimize the damage to the soft tissue. As mentioned earlier, the ablation rate for this short pulse width is approximately 1 $\mu\text{m}/\text{pulse}$. The future goal of the study will focus on limiting the damage to less than 5 μm which is believed to cause negligible damage to nerve tissue. To accomplish this, a fast electronics package is under development. Currently, the possible maximum damage is between 10 - 15 μm .

3. CONCLUSION

We demonstrated that a safe and precise microsurgery system using ultrashort pulse laser is feasible. The two wavelength comparison technique provides accurate selective tissue ablation.

4. ACKNOWLEDGMENTS

This work was performed at Lawrence Livermore National Laboratory under the auspices of the U.S. Department of Energy under contract No. W-7405-ENG-48.

5. REFERENCES

1. B. C. Stuart, M. D. Feit, S. Herman, A. M. Rubenchik, B. W. Shore, and M. D. Perry, "Nanosecond-to-femtosecond laser-induced breakdown in dielectrics," *Physical Review*, **53**, no. 4, pp. 1749-1761, 1996.
2. J. Neev, L. B. Da Silva, M. D. Feit, M. D. Perry, A. M. Rubenchik, and B. C. Stuart, "Ultrashort pulse lasers for hard tissue ablation," *IEEE J. Selected Topics in Quantum Electronics*, **2**, no. 4, pp. 790-800, 1996.
3. A. A. Oraevsky, L. B. Da Silva, A. M. Rubenchik, M. D. Feit, M. E. Glinsky, M. D. Perry, B. M. Mammini, W. Small, and B. C. Stuart, "Plasma mediated ablation of biological tissues with nanosecond-to-femtosecond laser pulses: Relative role of linear and nonlinear absorption," *IEEE J. Selected Topics in Quantum Electronics*, **2**, no. 4, pp. 801-809, 1996.
4. L. B. Da Silva, B. C. Stuart, P. M. Celliers, T. D. Chang, M. D. Feit, M. E. Glinsky, N. J. Heredia, S. Herman, S. M. Lane, R. A. London, D. L. Matthews, J. Neev, M. D. Perry, and A. M. Rubenchik, "Comparison of soft and hard tissue ablation with sub-ps and ns pulse lasers," *SPIE Proceedings*, **2681**, pp. 196-200, 1996.
5. M. D. Feit, A. M. Rubenchik, B.-M. Kim, L. B. Da Silva, and M. D. Perry, "Physical characterization of ultrashort laser pulse drilling of biological tissue," *Applied Surface Science*, 1998, (in press)
6. R. Birngruber, C. A. Puloafito, A. Gawande, W.-Z. Lin, R. T. Schoenlein, and J. G. Fujimoto, "Femtosecond laser-tissue interaction: Retinal injury studies," *IEEE J. Quantum Electronics*, **QE-23**, no. 10, pp. 1836-1844, 1987.
7. A. A. Oraevsky, S. L. Jacques, G. H. Pettit, F. K. Tittle, and P. D. Henry, "XeCl laser ablation of atherosclerotic aorta," *Lasers Surg. Med.*, **13**, pp. 168-178, 1993.
8. L. I. Deckelbaum, J. J. Scott, M. L. Stetz, K. M. O'Brien, and G. Backer, "Detection of calcified atherosclerotic plaque by laser-induced plasma emission," *Lasers Surg. Med.*, **12**, pp. 18-24, 1992.
9. A. A. Oraevsky, R. O. Esenaliev, and V. S. Letokhov, "Temporal characteristics and mechanism of atherosclerotic tissue ablation by nanosecond and picosecond laser pulses," *Lasers in the Life Sciences*, **5**, pp. 75-93, 1992.
- 10 B.-M. Kim, M. D. Feit, A. M. Rubenchik, B. M. Mammini, and L. B. Da Silva, "Optical feedback signal for ultrashort laser pulse ablation of tissue," *Applied Surface Science*, 1998 (in press)

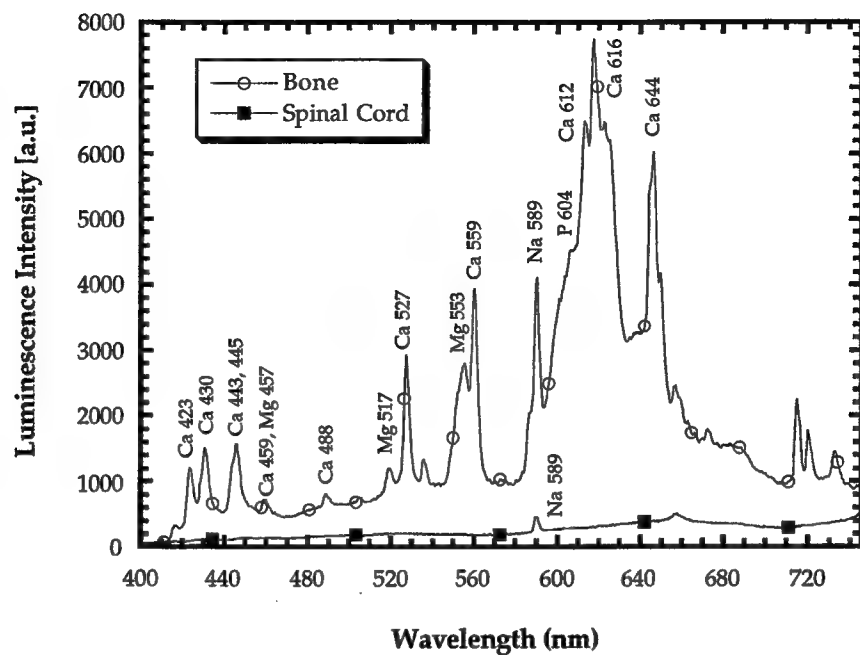


Fig. 1. Luminescence spectra from both porcine bone marrow and spinal cord. Strong calcium lines are observed from the bone spectrum.

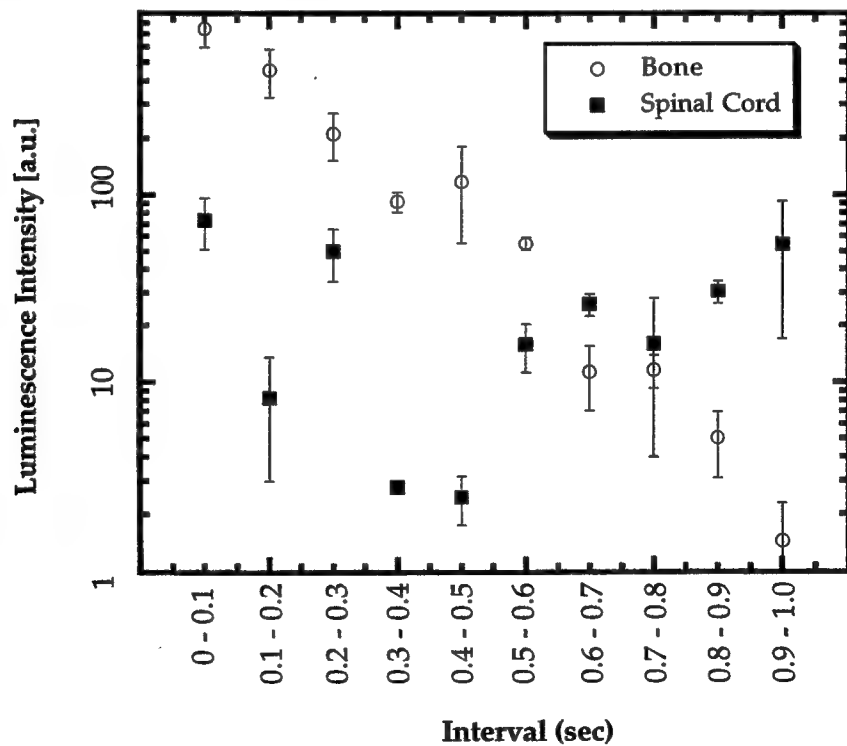


Fig. 2. Temporal changes of the absolute intensity of plasma luminescence from both bone and spinal cord.

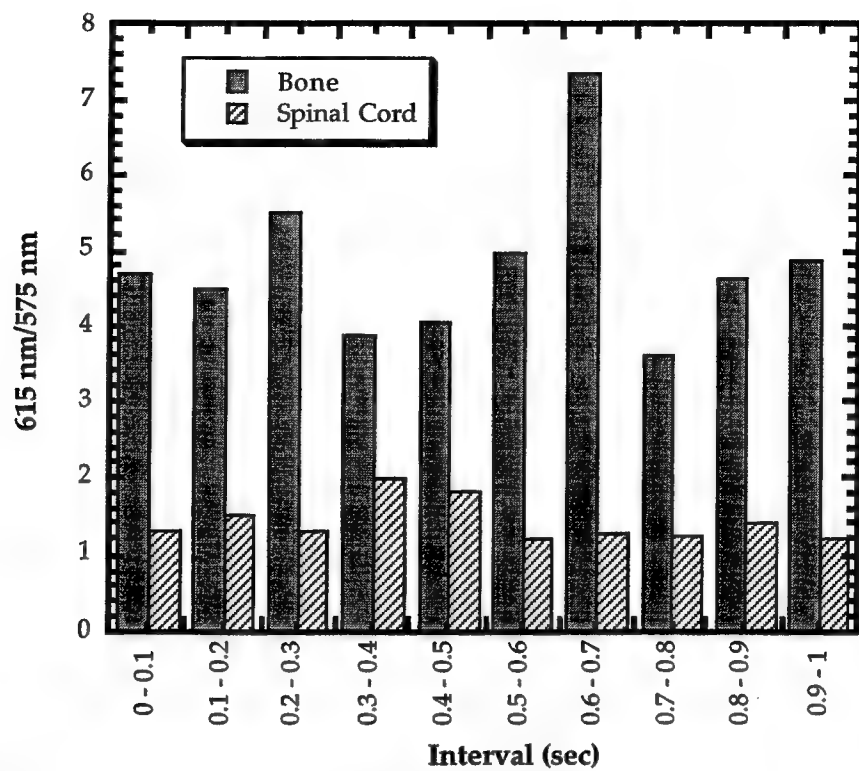


Fig. 3. Ratio of luminescence at 616 nm and 575 nm for both bone and spinal cord. Independent of absolute intensity, the ratio are consistent during 1 sec, 1 kHz pulse train.

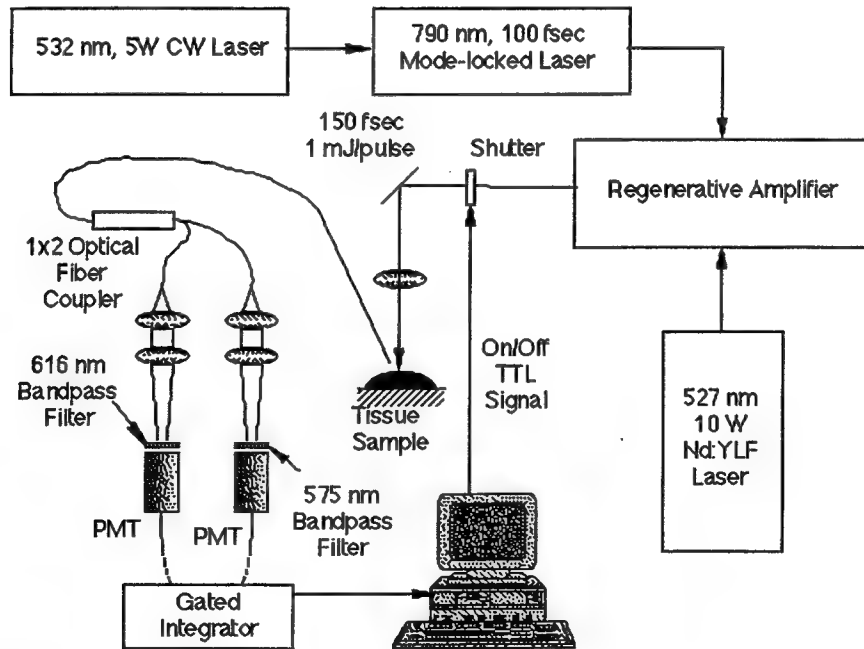
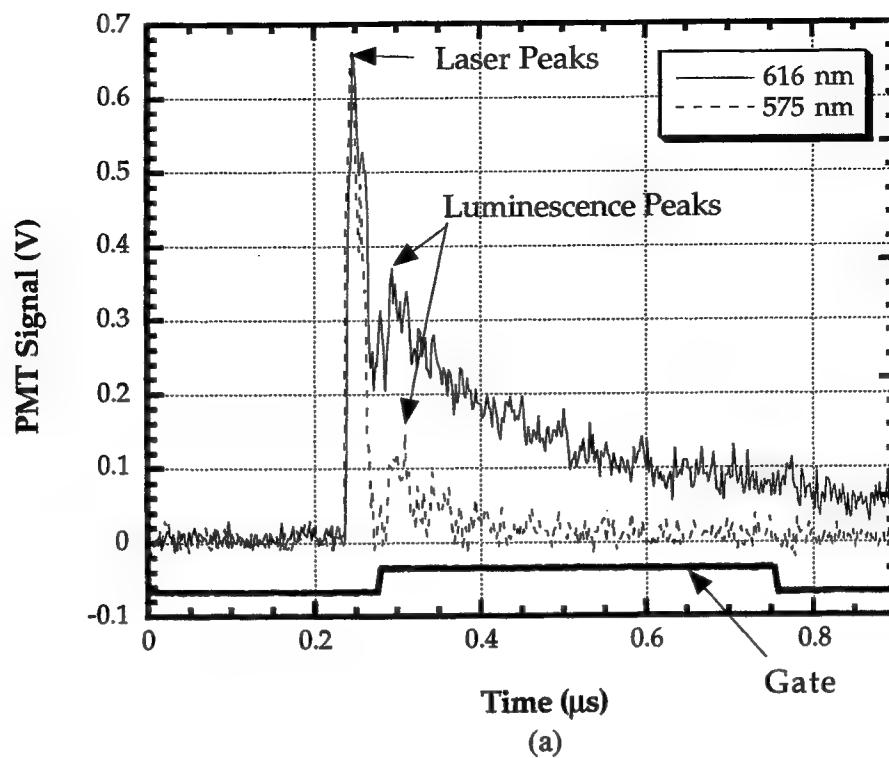
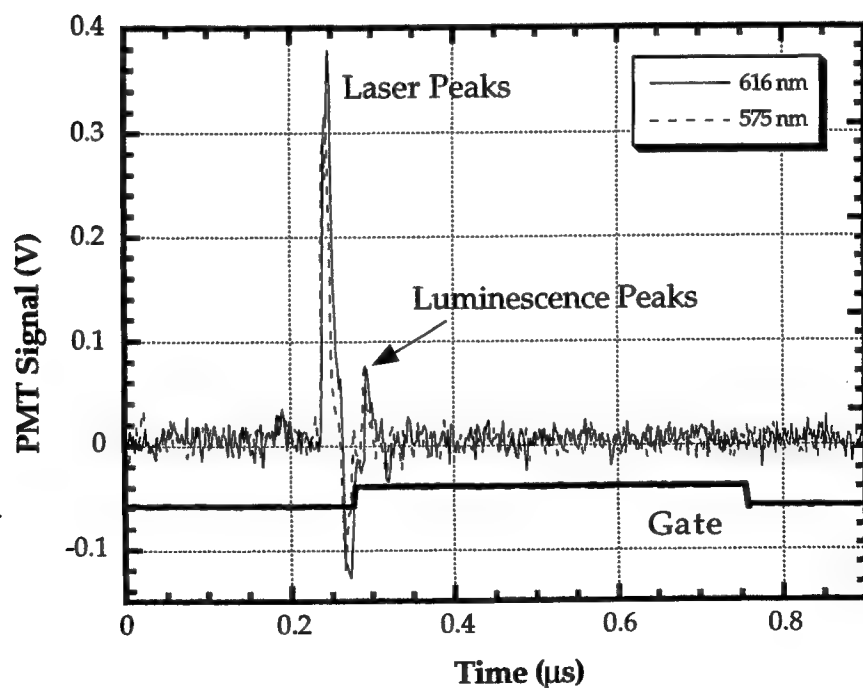


Fig. 4. A schematic for micro-spinal surgery using luminescence feedback control.



(a)



(b)

Fig. 5. Typical luminescence at 616 nm and 575 nm for (a) bone and (b) spinal cord. Initial strong peak represents the laser source light reflection.

Effect of the laser irradiation on the functional activity of enzymes with different structural complexity

Svetlana A. Ostrovtsava^a, Alexander P. Volodenkov^b, Alexander A. Maskevich^b, Irene M. Artsukevich^a, Slavomir S. Anufrik^b, Alexander F. Makarchikov^a, Ivan P. Chernikevich^a, Vitali I. Stepuro^b

^aInstitute of Biochemistry NAS of Belarus, Grodno, Belarus 230017

^bState University of Grodno, Grodno, Belarus 230023

ABSTRACT

Three enzymes differing in their structural composition were irradiated by UV lasers to study the effect of temperature, protein concentration and addition of small molecules on their sensitivity to radiation exposure. The laser - induced effects were due to the structural complexity of the protein molecules and depended on the dose applied, the wavelength and the density of irradiation. The multi-enzyme 2-oxoglutarate dehydrogenase complex (2OGDC) was subjected to pronounced irradiation - induced changes whereas the response of the two other enzymes was less significant. Reduction of the protein levels in irradiated samples was important under the XeCl laser coercion and the effects depended on the doses applied. The laser irradiation effects are suggested to be realized by means of conformational changes in the protein molecules and intermolecular association - dissociation processes.

Keywords: UV laser irradiation, 2-oxoglutarate dehydrogenase complex, fluorescence.

1. INTRODUCTION

Laser irradiation of enzymes causes significant changes in their activity. It has been shown that a chromophore - assisted laser inactivates 93% of β -galactosidase activity and 80% of alkaline phosphatase as well as 87% of acetylcholinesterase activity. Although thermal denaturation and photochemical mechanisms for proteins inactivation were postulated¹, the precise nature of the laser - mediated damage to the protein function has not been established.

Three enzymes differing in the complexity of their structural compositions were studied in connection with laser- induced changes in their functional activities. Thiamine triphosphatase (ThTPase: EC 3.6.1.28), characterized by the simplest structure presented by one polypeptide chain (Mr 28 000), alcohol oxidase (AO: EC 1.1.3.13), built of four identical subunits (Mr 300 000) having coenzyme FAD (flavine adenine dinucleotide) in its composition, and 2 -oxoglutarate dehydrogenase complex as an ensemble of three separate enzymes: 2 - oxoglutarate dehydrogenase (E1o: EC 1.2.4.2), dihydrolipoamide succinyltransferase (E2o:EC 2.3.1.61) and dihydrolipoamide dehydrogenase (E3 : EC 1.8.1.4), possessing TPP, lipoic acid residues and FAD incorporated as cofactors into E1o, E2o and E3, accordingly, have been examined for their activity under the effect of the UV laser irradiation.

The fluorescence of 2-oxoglutarate dehydrogenase complex from bovine heart after the irradiation by the XeCl and the nitrogen lasers was studied. The fluorescence intensity of bound flavine adenine dinucleotide was increased after high doses of the excimer laser treatment.

2. MATERIALS AND METHODS

The sources of coherent UV irradiation were a pulse nitrogen laser and an excimer XeCl laser. The electron discharging XeCl laser designed at the Grodno State University served as a source of UV irradiation ($\lambda = 308$ nm). The laser performs

the following parameters: the generating energy of the pulse was around 2J with a pulse frequency of 1 Hz and halfwidth equal to 50 ns. The specially designed XeCl laser enables us to vary the pulse duration from 25 to 100 ns with generating energy of 0.6 mJ. The protein samples were subjected to laser pulses with energy of 25, 50 and 150 mJ and 60 ns halfwidth. The pulse was generated by separation of the laser beam producing the energy required in the experiment. The beam was focused with a long - focal quartz lens (F=1m) and directed vertically on the tubes containing protein solutions to obtain a spot on the sample with diameter of 5 mm.

Standard nitrogen laser (LGP - 505) was used as source of the UV irradiation ($\lambda=337$ nm) to generate a pulsed laser beam with a pulse width of 10ns at a frequency ranging from 12 to 1000 Hz. The protein samples were subjected to 1 min, 3 min and 5 min of laser pulses of 0.25 mJ per pulse at a frequency of 16 Hz and a power 4 MW that corresponded to the doses of irradiation equal to 240 mJ, 720 mJ and 1200 mJ. Use of different doses of irradiation by the two lasers was caused by the facts that eximeric laser generates twofold higher pulse power then nitrogen one and the activity of the XeCl laser emanation was higher. The experiments done have shown that the lowest dose of nitrogen laser irradiation when some changes of the functional activity of 2OGDC become noticeable corresponded to the 1 min of the protein complex treatment.

2OGDC was extracted from bovine heart and purified by the method of Stanley² with our modifications³. Enzyme activity was assayed by monitoring NADN formation at 340nm and 30°C, alcohol oxidase was isolated from Candida boidinii cells by a specially developed method⁴ and thiamine triphosphatase was purified by a method developed for the enzyme from bovine brain⁵. The computations were performed by using linear least square regression⁶. The kinetic parameters were calculated using Lineweaver- Burk plots⁷.

Steady-state fluorescence spectra of the protein solutions were recorded by the SDL-2 and DFS-52 spectrometers (LOMO, Russia). Fluorescence decay measurements were performed with a nanosecond pulse fluorimeter⁸. The samples were excited using a nitrogen flash lamp generating exciting pulse with a half width of 1 ns. A PC 486DX was used for the operation and data processing. The decay data analysis (deconvolution) was performed according to the method taking into account the finite width of the profiles of the excitation pulse and the response function of the apparatus.^{9,10}

Experimentally obtained fluorescence decay curve $I(t)$ is considered as a convolution of the decay law of the sample $F(t)$ with the instrument response function $L(t)$ ^{11,12}

$$I(t) = \int_0^t L(t') F(t-t') dt' \quad (1)$$

The fluorescence decay law is usually simulated as a sum of exponentials

$$F(t) = \sum_j \alpha_j \exp\left(-\frac{t}{\tau_j}\right) \quad (2)$$

where α_j and τ_j are the decay amplitude and lifetime respectively.

Using non-linear least squares method the fitting parameters α_j , τ_j were determined by minimizing χ^2_v ¹³,

$$\chi^2_v = \frac{1}{v} \sum_i W(t_i) \cdot [I(t_i) - Y(t_i)]^2, \quad (3)$$

where the index i sums over the appropriate channel region. $I(t_i)$ and $Y(t_i)$ denote, respectively, the observed and calculated values corresponding to the i channel, and $W(t_i)$ is the corresponding statistical weight. v represents the number of degrees of freedom for the fluorescence decay surface.

$W(t_i)$ is defined as a magnitude, reciprocal to the variance of the observed fluorescence intensity in i channel.

$$\frac{1}{W(t_i)} = \text{var } I(t_i). \quad (4)$$

We used a modified expression for statistical weights to take into account the influence of noise on the instrument response function $L(t)$.

$$\frac{1}{W(t_i)} = \text{var } I(t_i) + \int_0^{t_i} \text{var } L(t') \cdot F^2(t_i - t') dt'. \quad (5)$$

This modification is useful when the average lifetime is less then or equal to the excitation pulse duration.

To monitor the dependence of the apparatus response function on the wavelength a "shift method"¹¹ was used.

The protein samples of OGDC, AO and ThTPase were prepared by dissolving of the protein either in 0.02 M phosphate or Tris - buffer (pH 7.4).

3. RESULTS AND DISCUSSION

The radiation studies carried on purified enzymes were performed using an UV laser equipment generating 308 and 337 nm laser light. All the irradiation procedures were performed at 4°C (excluding the experiments on increasing temperature effects). The possible effects of the protein concentration in irradiated sample, temperature and the addition of small molecules- dithiothreitol and sodium azide (NaN₃) on the functional activity of three enzymes of interest-were examined.

Thiamine triphosphatase possessing the simplest composition was unaffected by any of the lasers used. The response of alcohol oxidase, a tetrameric flavoprotein, to excimer laser light exposure was noticeable. It was established that the effects obtained depended on the protein concentration. It was shown that when the protein level in the sample was equal to 0.25 mg/ml the laser irradiation at a dose of 50 and 200 mJ diminished the AO activity in both the cases. The kinetic investigations provide evidence for the V_{max} being 80% of the initial value and the Km did not change. In increasing AO concentration to 0.5 mg/ml the effect of these dose irradiation was not detected. However, soon after the treatment of more concentrated preparations (after storing of the enzyme during 24 hours) the AO activity decreased quickly. The preliminary introduction of the alcohol oxidase stabiliser - NaN₃ - to the alcohol oxidase solution did not only protect AO from inactivation but prolonged the enzyme lifetime. The further increasing of the AO concentration to 1 mg/ml led to some activation of the enzyme (up to 130%).

Being the ensemble of tree constituent enzymes, the multi - enzyme 2-oxoglutarate dehydrogenase complex was mostly affected by UV laser irradiation. It has been shown that nitrogen laser caused a significant decrease of the OGDC activity (Table 1). The effect did not depend on the protein concentration in the preparations of the complex. The irradiation of the enzyme solution at 24°C resulted in a loss of 12% of its activity even in the case of short (1min) treatment by the beam possessing medium power of the pulse (720 mJ).

The effect of the temperature increase was unnoticed with using of XeCl laser, whereas the protein level was an important factor. The high dose of the laser irradiation (150 mJ) and reduced protein concentration (up to 0.12 mg/ml) caused a pronounced loss of the OGDC activity (see Table 1). Even lower doses of the laser irradiation resulted in marked inhibition of the diluted preparation of the complex.

Table 1. Activity of the 2-oxoglutarate dehydrogenase complex affected by different doses of UV laser irradiation (t=4°C)

Enzyme concentrations (mg/ml)	ACTIVITY, %					
	XeCl laser (mJ)		Nitrogen laser (mJ)			
	25	50	150	240	720	1200
2OGDC, 0.7	114	108	104	100	108	60
2OGDC, 0.7 + 0.5 mM DTT	-	128	118	108	112	100
2OGDC, 0.25	156	100	-	100	100	70
2OGDC, 0.12	40	40	20	-	-	-
2OGDC, 0.12 + 0.5 mM DTT	100	128	118	-	-	-

The inhibition of the complex activity after the treatment of the enzyme by high doses of both the lasers used in the experiments was almost abolished when a reducing agent dithiothreitol at a concentration of 0.5 mM was presented in the OGDC solution, and even some activation was noticed after the complex was subjected to excimer and nitrogen lasers irradiation. The effect was characteristic both for more concentrated preparations and diluted ones. Interestingly, the low doses of XeCl laser irradiation (25 mJ) resulted in activation of the OGDC in preparations with lower (0.25 mg/ml) protein concentration.

The 2-oxoglutarate dehydrogenase complex isolated from bovine heart possesses two types of active sites with different substrate affinity, the property we have reported earlier¹⁴. We therefore ran an experiment to test the effect of the type of laser irradiation and the dose applied on the kinetics of 2OGDC and possible changes in the $S_{0.5}$ and V_{max} values were determined. The low doses of the XeCl laser (25 mJ) applied for diluted preparations of the complex produced a 3-fold decrease of the $S_{0.5}$ values estimated for the slowly functioning active sites localized on the OGD dimers (from 250 to 33 mM), simultaneously increasing this index calculated for the sites with high affinity to 2-oxoglutarate (from 9 to 14 mM) and producing a 100% increase of the V_{max} of the catalysis by these type of active sites. The effects obtained on the concentrated 2OGDC were realized by the mean of $S_{0.5}$ values decreasing determined for quickly - reacting sites (20%) without noticeable changes in the V_{max} .

The inhibition of OGDC activity by nitrogen laser irradiation was attended by 7.5 - fold increase of the $S_{0.5}$ values determined for the active sites binding 2 - oxoglutarate with high affinity and by 2 - fold decrease of V_{max} . Thus, the laser irradiation affects the affinity of the OGD to the substrate as well as the velocity of the reaction of 2 - oxoglutarate decarboxylation.

The third component of 2OGDC, dihydrolipoamide dehydrogenase, catalysing the terminating reaction of the complex, was more sensitive to the effects of irradiation. The treatment of E 3 by high doses of the nitrogen laser (1200mJ) inhibited 50% of the enzyme activity. The excimer laser effects on the activity of the third component of OGDC depended on the dose of irradiation applied, and the most significant inhibition (45%) was registered in response to the protein irradiation by 308 nm laser light with a dose of 150 mJ.

It is suggested that the radiation - caused changes of multi - enzyme complex functional activity can occur at least partially as a result of changing of conformational states of OGDC protein molecules. Intermolecular association - dissociation processes may also take place. The mechanisms can be realized via breaking of the intersubunit interactions after a high dose irradiation. Radiation damage to protein can also occur by free radical reactions as a result of free radical attacks destroying subunits of the enzymes and producing unexpected target sizes of some protein¹⁵. So DTT protecting OGDC from a loss of activity can act as a free radical scavenger.

The next step of the work was focused on the study of the laser irradiation influence on the fluorescence of tryptophane residues and bound flavine dinucleotide in order to check whether 2OGDC protein molecules underwent some conformational rearrangements induced by the irradiation.

2OGDC was shown to possess significant intrinsic fluorescence (the main parameters of it are listed in the Table 2). Excited at 295 nm, in the region of tryptophane residues absorption, the protein complex exhibits fluorescence with a maximum at 330 nm. This short-wave position of the spectrum may be a result of tryptophane residues localization in low- polar regions of the protein globule, which does not enable water to penetrate. The other possible reason is a significant slowing of relaxation processes in chromophores after excitation. The polarization degree P, determined by segmental mobility of amino acid residues, is characterized by low values (around 0.12), confirming our first suggestion. Obtained small long-wave shift of spectrum (~2 nm, see Table 2) when using "red edge excitation" indicates microenvironment heterogeneity of the excited tryptophanyl.

Table 2. Parameters of 2-OGDC intrinsic fluorescence. $\lambda_{ex}=295$ nm. Protein concentration was 0.3 mg/ml.

Sample	Intensity	λ_{max} , nm	P	ϕ ³⁾
2-OGDC	1.00	330	0.12	0.050
2- OGDC ¹⁾	-	332	0.13	-
2- OGDC ²⁾	0.90	330	0.12	0.045

¹⁾ $\lambda_{ex} = 305$ nm

²⁾ after the XeCl laser irradiation (150 mJ)

³⁾ quantum yield was determined relatively to tryptophane with $\phi=0.20$.

The fluorescence decay was nonexponential (Table 3, Fig.1) and might be described by three exponential terms with fluorescence lifetime $\tau_1= 0.89$ ns, $\tau_2= 2.6$ ns, $\tau_3= 5.4$ ns under conditions of satisfactory values for statistical criteria.

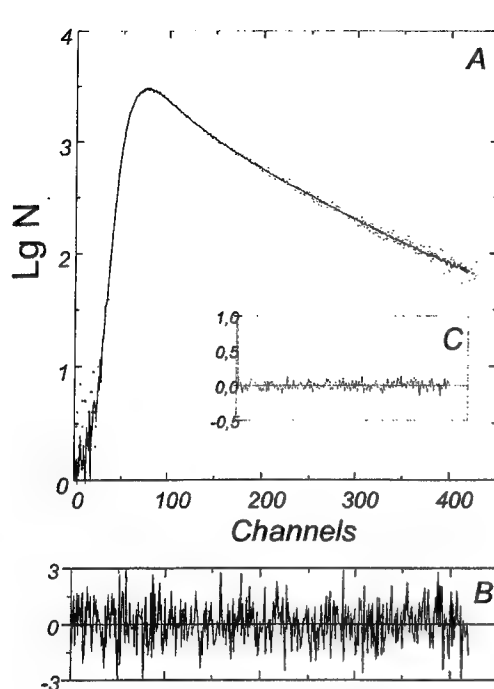


Figure 1. Fluorescence decay curve of 2OGDC. A- experimental and calculated decay curve: dots correspond to experimental data, solid curve is the result of approximation with three-exponential function; B- distribution of weighted residuals; C- autocorrelation function of weighted residuals.

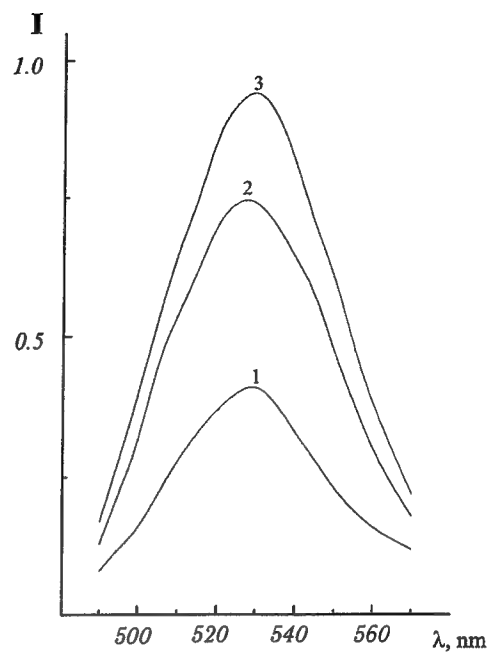


Figure 2. Fluorescence spectra of native 2OGDC (1) and after the XeCl laser irradiation using the doses of 25 (2) and 150 mJ (3).

Table 3. Fluorescence decay lifetimes of OGDC approximated by single, bi-, and three-exponential functions. $\lambda_{\text{ex}} = 297 \text{ nm}$, $\lambda_{\text{em}} = 340 \text{ nm}$. Standard deviation of τ determination did not exceed 5%. $\langle \tau \rangle = \alpha_1 \tau_1 + \alpha_2 \tau_2 + \alpha_3 \tau_3$, $(\alpha_1 + \alpha_2 + \alpha_3 = 1)$

α_1	$\tau_1, \text{ ns}$	α_2	$\tau_2, \text{ ns}$	α_3	$\tau_3, \text{ ns}$	$\langle \tau \rangle, \text{ ns}$	χ^2
1.00	3.30	-	-	-	-	-	13.8
0.37	1.20	0.63	4.60	-	-	-	1.04
0.48	0.88	0.31	2.64	0.21	5.38	2.40	0.97

Nonexponential character of tryptophane fluorescence decay is a typical property of proteins¹². Most of the studied proteins demonstrate the same character of the intrinsic fluorescence decay presented as a sum of three exponentials. There may be three equilibrated conformations of tryptophanyl in respect to a peptide bond where they possess different values for the fluorescence decay constants. The protein structure is not static and undergoes significant fluctuations¹⁶. As a result, the function of decay is occasionally presented by three continuous chromophore distribution according to the constants of emissive transition¹⁷. Such distributions are frequently wide enough and are overlapped, and only one or two chromophore distributions can be determined using mathematical calculations¹⁸. Solving the problem of the distribution type is a

complicated task and need further experiments. The data obtained from the fluorescence decay curves confirm the assumption about high heterogeneity of microenvironment of emitting tryptophanyls.

2OGDC comprises the incorporated FAD as a coenzyme which possesses the property of intrinsic fluorescence with a maximum of the spectrum at 530 nm (Fig.2). The fluorescence intensity of the native protein is low and is equal only to 1% of the free coenzyme fluorescence recorded under the same conditions.

The XeCl laser irradiation of the protein resulted in some decrease of tryptophane fluorescence of the 2-oxoglutarate dehydrogenase complex (Table 2) producing no changes in the emission spectrum, its localization and polarization degree. The FAD fluorescence was more sensitive to the irradiation. The FAD emission intensity increased twofold when treated by a high dose (150 mJ) of the excimer laser (Fig.2).

The data obtained indicate that the active site localized on the E3 component of 2OGDC had a pronounced sensitivity to the XeCl laser irradiation. These results are in agreement with the kinetic studies which showed a loss of this constituent enzyme activity depending on the irradiation dose applied. It is known that the fluorescence of FAD incorporated into the protein is effectively quenched by the neighboring amino acid residues (tyrosine, tryptophane or cysteine) possessing groups which can be electron donors¹⁶. The laser irradiation causes conformational changes in the enzyme structure, thus affecting the structure of the active site. These processes resulted in decreased quenching and enhanced fluorescence of the protein molecule. Moreover, one or several tryptophane residues possibly localized in the vicinity of the active site contribute to the changes in the protein intrinsic fluorescence. Since 2OGDC is a polytryptophane protein, we have not found noticeable changes in a number of fluorescence parameters, such as spectrum localization, polarization degree and others.

4. ACKNOWLEDGEMENTS

We would like to thank Mrs. L. Kiryukhina for help in the preparation of the final English version of the manuscript.

REFERENCES

1. J. Liao, J. Roider and D. Jay, "Chromophore - assisted laser inactivation of proteins is mediated by the photogeneration of free radicals", *Proc.Natl.Acad.Sci.USA* 91, pp.2659 - 2663, 1994.
2. C. Stanley and R. Perham, "Purification of 2 - oxo acid dehydrogenase multienzyme complexes from ox heart by a new method", *Biochem.J.* 191, N 1, pp. 147 - 154, 1980.
3. S. Ostrovtsova and S. Strumilo, "Participation of adenosine diphosphate in regulation of the 2-oxoglutarate dehydrogenase complex from human heart", *Biomed.Biochim.Acta* 49, pp.515 -517, 1990.
4. I. Artsukovich, I. Chernikovich and Yu. Ostrovskii, "The production of yeast alcohol oxidase", USSR Patent N 2032743, 1990.
5. A. Makarchikov and I. Chernikovich, "Purification and characterisation of thiamine triphosphatase from bovine brain", *Biochim. et Biophys.Acta*, 1117, pp.326 - 332, 1992.
6. T. Keleti, *Basic enzyme kinetics*, pp.321 -323, Academiai Kiado, Budapest, 1986.
7. A. Cornish - Bowden, *Principles of enzymatic kinetics (Russ.)*, pp.46 -47, Mir, Moscow, 1979.
8. G.A. Gachko, L.N. Kivach, S.A. Maskevich, "Automatic pulse spectrofluorimeter," *J. Prikl. Spectr.* (in Russian). 47, pp. 335-339, 1987
9. S.K. Basharin, G.A. Gachko, L.N. Kivach, et all., "Deconvolution of fluorescence decay curves", *J. Prikl. Spectr.* (in Russian), 52, pp. 48-52, 1990.
10. A.A. Maskevich, S.K. Basharin, G.A. Gachko et all., "Deconvolution fluorescence decay curves for the case continuos lifetime distribution," *J. Prikl. Spectr.* (in Russian), 53, pp. 557-563, 1990.
11. D.V. O'Connor and D. Phillips, *Time-correlated Single Photon Counting*, pp. 159, Academic Press, London, 1984.
12. J.R. Lakowicz, *Principles of Fluorescence Spectroscopy*, pp. 77, 369; Plenum Press, New York, 1984.
13. P.R. Bevington, *Data reduction and error analysis for the physical sciences*, McGraw-Hill, New York, 1969
14. S. Ostrovtsova, "Inhibition of the 2- Oxoglutarate Dehydrogenase Complex by free fatty acids", *Med.Sci.Res.* 24, N9, pp.625 -627, 1996.
15. E. Kempner and J. Miller, "Effect of Environmental Conditions on Radiation Target Size Analyses", *Anal. Biochem.* 216, pp.451 - 455, 1994

16. Demchenko A.P., *Ultraviolet spectroscopy of proteins*; Springer Verlag, Berlin, 1986.
17. Demchenko A.P., Gallay G, Przhonska O., "Fluorescence lifetimes distributions in the studies of dielectric relaxations in viscous solvents, polymers and protein molecules", *Book of Abstracts XVIIIth International Conference on Photochemistry*, P. I5.1, Warsaw, 1997.
18. Gratton E., Alcala R, Marritt G., Prendergast F. *Fluorescence studies of protein dynamis*, Urbana, 1985. (Preprint /University of Illinois; ILL-(EX)-85/53).

Preliminary Characterization of Hard Dental Tissue Ablation With Femtosecond Lasers

Joseph Neev ^a and Jeff Squier^b

^a950 Acapulco Laguna, Laguna Beach, CA 92651; ^bElectrical and computer engineering department University of California San Diego, La Jolla, CA 92093-0339.

Abstract

Because of low operating speed and excessive collateral damage, lasers have not succeeded in replacing conventional tools in many surgical and dental applications. Recent developments now allow the new generation of amplified ultrashort pulse lasers to operate at high repetition rates and high single pulse energies. A Titanium:sapphire Chirped Pulse Regenerative Amplifier system operating at 1 KHz and 50 fs pulse duration, was used to demonstrate ultrashort pulse ablation of hard and soft tissue. Maximum ablation rates for enamel and dentin were approximately $0.650 \mu\text{m} / \text{pulse}$ and $1.2 \mu\text{m} / \text{pulse}$ respectively. Temperature measurements at both front and rear surface of a 1 mm dentin and enamel slices showed minimal increases. Scanning electron micrographs clearly show that little thermal damage is generate by the laser system. If an effective delivery system is developed, ultrashort pulse system may offer a viable alternative as a safe, low noise dental tool.

Introduction.

Using lasers to ablate hard tissue offers the potential for rapid, precise, accurate operation with minimal thermal and mechanical damage to surrounding tissue. Lasers have therefore been used for a variety of sensitive hard and soft tissue applications such as mid-ear bone ablation, implantation of joint prostheses in orthopedic surgery, removal of malignant tissue and other procedures involving bone, nail, cartilage and other hard and soft tissue.

In the field of dentistry, laser applications include treatment of oral malignancies and periodontal diseases, dental caries prevention, control, and removal of hard tissue for cavity and restoration, preparation, and sterilization (1 - 9). Clearly, the greatest anxiety generators in the dentist's office are the dental drill and the accompanying anesthesia shots that are required for most hard tissue procedures. Indeed, the fear of pain during dental procedures is so great that it deters patients from seeking help while the damage to healthy tooth structure continues to spread (10,11). According to a survey by Smith et al (10), 40% of the population reported that they have fear of dental treatment, with 17% reporting high anxiety.

In a recent review (9) Wigdor et al reported that many patients are so fearful of dental procedures that they frequently wait until the pain from infection is so great that they are willing to endure the perceived painful treatment to gain relief. The long term goal of dental laser research has thus long been the development of a new modality to replace the dental hand piece.

In spite of their promise, lasers has not been able to replace the drill or scalpel in many surgical and dental procedures. The limitation of existing laser systems will be outlined below, essentially, however, there are two interaction characteristics which limit the success of surgical and dental procedures: low removal rates and high collateral damage.

Low removal rates is generally a characteristic of short pulse lasers (~ns). It typically involves material removal on the order of a single to a few μm in depth and low residual heating. Since pulse duration is relatively short, thermal seed electron induce plasma generation through subsequent avalanche process. The plasma mediated ablation, results in plasma shielding as pulse energy is increased which followed by a sharp drop in per-pulse ablation efficiency with energy. As a consequence, all high

intensity short pulse lasers are limited in their ablation rates to the $\mu\text{m}/\text{pulse}$ range.

Longer pulse ablation such as the 100 to 300 μs pulsed free-running normal mode solid state lasers results in ablation on the order of several tens of a micrometer per pulse. Ablation with these systems, however, is also characterized by a considerably larger residual pulse energy, larger amount of material ejection and a larger stress transient.

It is thus possible to generalize and assert that under the current status of laser technology (where ultrashort pulse lasers are not considered), we have a choice between a lower ablation rate, higher precision nanosecond systems with lower thermal and mechanical signature, and that of the considerably higher ablation rate longer pulse system also characterized by higher residual heat and large transient stresses.

When a practical system is considered several concerns must be addressed simultaneously: Tissue selectivity, ablation efficiency, thermal and mechanical damage, confinement of ablative effects, ease of delivery, ablated surface morphology, microhardness and changes in mineralization. The perfect laser tool, of course, need to address and give adequate solutions to all of these problems, since any one of these potential problem could jeopardize the tooth or result in an inferior treatment. In addition, an adequate practical tool must be sufficiently inexpensive to be affordable to private practitioners.

Previous studies of ultrashort pulse regime with hard dental tissue included pulse durations from the 100 fs to the ns range (12, 13, 14, 15). This paper, describes recent experiments using USPL systems operating at very high peak power. It demonstrates the technical advantage of USPL over other, existing laser systems as well as conventional, non-laser technologies. The problems presented by the current high cost of USPL system, and the

relatively large size of current USPL systems must naturally be addressed.

Material and Methods

Ultrashort pulse Laser system.

For plasma mediated ablation studies, laser pulses generated by a Ti:Sapphire Chirped Pulse Amplifier (CPA) system with an frequency-doubled, Nd:YAG pump laser. The 800 nm Ti:Sapphire oscillator was pumped by a Millennia Laser (Spectra Physics, CA) used also pumped by an Nd:YAG source. Output compressed pulses, 50 fs long and up to 500 μ J in energy at 1 KHz were used. Various attenuator allowed determination of threshold fluence and ablation characteristics over the entire energy range. A spot size of 100 μ m allowed studies of fluences ranging from 0.4 J/cm² to 4 J/cm².

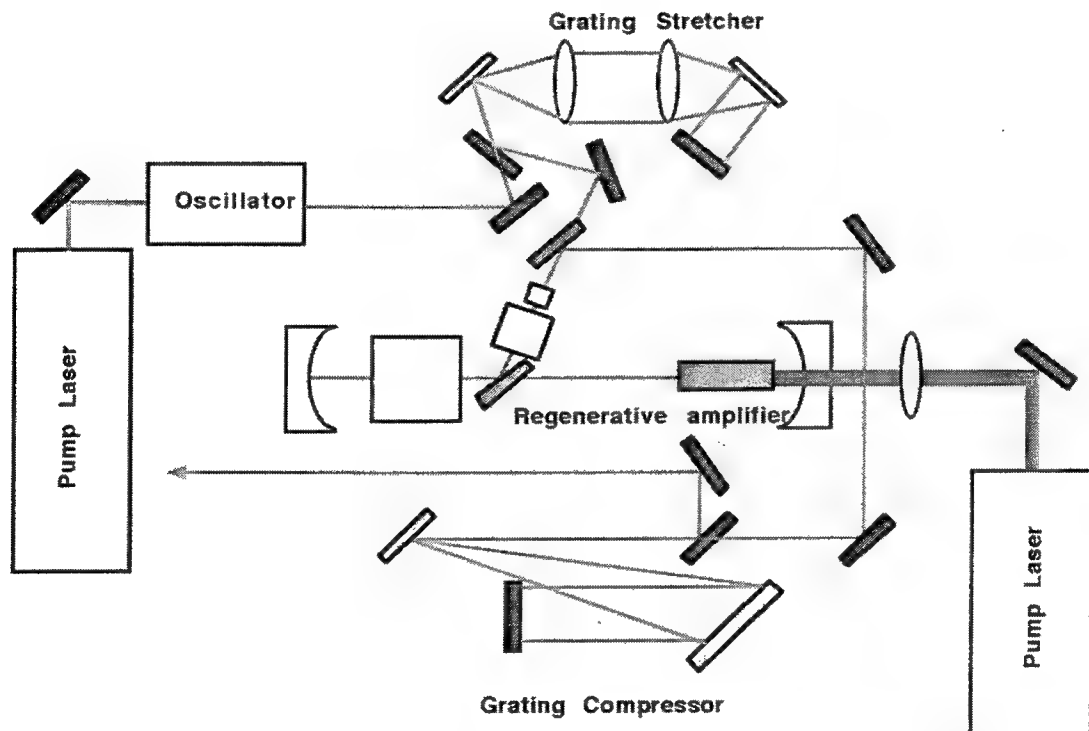


Figure 1. The kilohertz Ti:Sapphire system used in the experiments. A Ti:Sapphire oscillator produces the seed pulses which are stretched using a 1200 1/mm grating pair. The pulses are amplified to 1 mJ in the regenerative amplifier at kilohertz repetition rates. The pulses are recompressed by a 1200 1/mm grating pair which results in 50 fs, 500 μ J pulses.

Ablation studies were performed using thin dentin slices. Dentin slices 0.5 to 1.0 mm thick were cut from the middle section of freshly extracted third molars, in a plane perpendicular to the occlusal-cervical direction. Teeth were treated with 0.5M EDTA for 2 minutes to remove the smear layer, then stored in 10% thymol solution until treatment. Tissue was sliced parallel to the crown and washed with demineralized water. Slices included an external ring of enamel tissue on the outside and dentin.

Ablation rates were determined by monitoring the ablated slice with a video camera. A frame by frame analysis allowed detection of ablation start point as well as that of the perforation endpoint.

A thermal camera (Inframetrics Model 600 Imaging Radiometer, Bedford, MA) with a scan speed of 32 frames per second was used for temperature measurements. The center temperature adjustment ranges from 20 to 1,500 °c. The camera field of view could be adjusted from 1:1 to 8:1, and was maintained at 2:1 or 4:1. The camera detector was a liquid nitrogen cooled HgCdTe with spectral sensitivity from 8 to 12 μ m. The thermal camera was placed so that the surface temperature (ST) could be viewed directly. The camera was operated in the point mode so that both the entire temperature field could be viewed with false color presentation and a single point (specified by the operator) numerical value could be read directly with the camera specified accuracy of \pm 0.5 degrees. Temperatures were measure on the back surface of the 1 mm dentin slices while the laser was ablating the front surface. Camera emissivity was calibrated by comparing temperature of dentin slice half painted with black ink. The emissivity of specification for the camera software was adjusted until the temperature reading of the non painted section matched that of section painted with the black ink. The camera was further checked against a standard thermometer readings of water reservoir which temperature was gradually varied.

Results

Ablation rates

The ablation rates in enamel and dentin at all fluence levels studied are summarized in figure 2 through 6. The threshold for plasma formation for both enamel and dentin was 0.4 J/cm^2 . As is evident from the figure 2 and figure 3, both enamel and dentin show a clear pattern of diminishing amount of material removed per pulse as the pulse fluence increases. From the ablation threshold at approximately 0.5 J/cm^2 , ablation rate (AR) increased rapidly to about $1 \mu\text{m}/\text{pulse}$ at 3 J/cm^2 where ablation for both tissue types were very similar. While the ablation threshold appears higher for interaction with enamel, this is really a consequence of our method of measuring ablation depth per pulse (slice perforation) and the stalling that occurs earlier in enamel unless higher fluences are used. Beyond that level, only a very small increase occurs in AR with fluence

For comparison, figure 4 illustrate ablation with higher pulse energies and fluences but longer pulse duration, namely that of 350 fs (and $1.054 \mu\text{m}$) and one nanosecond. As can be seen from the figure, the ablation pattern for the 350 fs pulses is similar to that of the 50 fs one. Once the pulse duration crosses the ultrashort threshold ($\sim 10 \text{ ps}$) the ablation fluence threshold for the $1.054 \mu\text{m}$ 1 ns pulses is considerably higher (20 J/cm^2), and the ablation characteristics change.

As figure 4 shows, the nanosecond pulse ablation at 34 J/cm^2 illustrated the AR differences. Here, 3 J/cm^2 is well below the ablation threshold of either enamel or dentin. Ablation threshold for the nanosecond system was observed at approximately 20 J/cm^2 but is not shown here since it was not the object of this study. For the same fluence level in the nanosecond regime AR are very different for enamel and dentin (dentin ablation is almost a factor of four greater). The comparison thus shows the considerably enhance efficiency of the CPA pulses (approximately $1 \mu\text{m}/\text{mJ}$ at 1 J/cm^2 for both enamel and dentin) in comparison to the

34 J/cm² 1ns pulse with 0.03 $\mu\text{m}/\text{mJ}$ for ablation of Enamel, and 0.12 $\mu\text{m}/\text{mJ}$ of dentin. It also shows the lack of material sensitivity of the fs ablation, especially when compared to the ns regime.

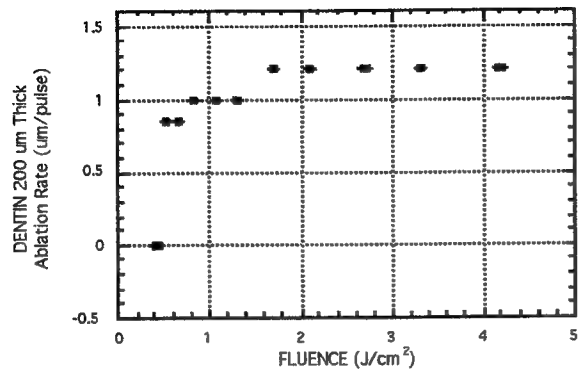


Figure 2.
Dentin ablation rates as a function of 50 fs pulse fluence.

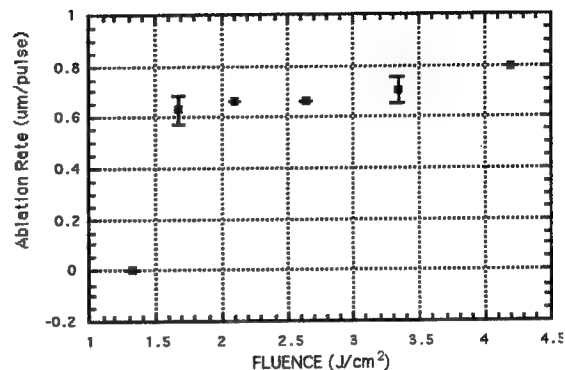


Figure 3.
Enamel ablation rates as a function of 50 fs pulse fluence.

Figure 5 and Figure 6 show the dependence of the per-pulse ablation rate on the sample thickness. As was discussed previously (16) the ablation spot size changes as a function of penetration depth into the tissue. To investigate if that change also translated into a per-pulse ablation rate changes various slice thickness were tested.

As both figure 5 and 6 show, essentially no statistically significant variation were noted in either enamel or dentin. On the other hand, at the maximum pulse energy of 400 μJ per pulse the largest enamel slice that was penetrated was 380 μm thick, while the largest dentin slice that was penetrated was 900 μm thick.

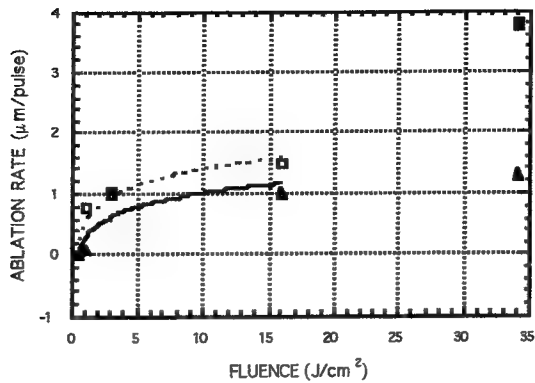


Figure 4 Dentin (triangles) and enamel (squares) ablation rates as function of fluence for 350 fs pulses (empty symbols) and 1 ns pulses (full symbols).

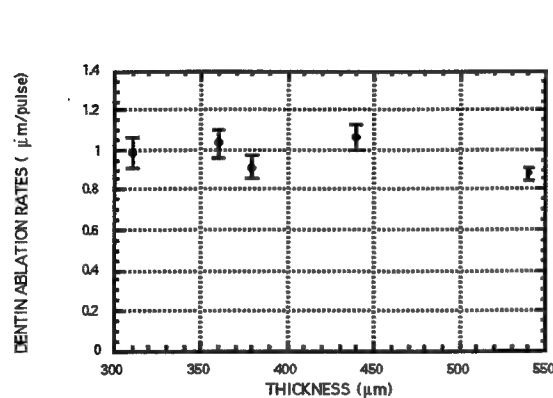


Figure 5
Dentin ablation rates as a function of ablated slice thickness

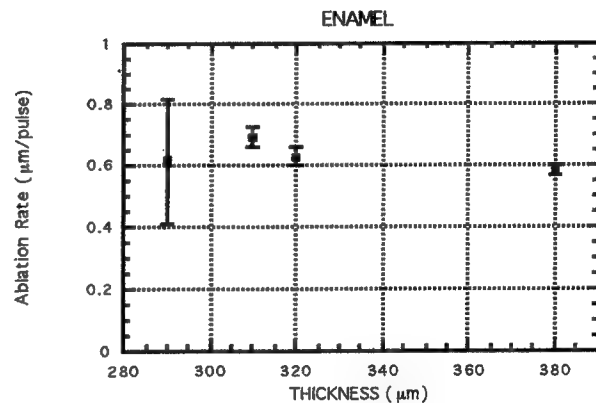


Figure 6.
Enamel ablation rates as a function of ablated slice thickness

Temperature measurements.

Temperature observed at the back surface of a 1mm thick dentin showed an increase of up to 45°C when the beam was applied continuously for a period of several minutes. This increase, however, was observed only when the laser beam ablation penetrate the 1mm dentin slice and the interaction was taking place very close to the back (i.e. monitored) surface. When the ablation was

confined to interactions at the front surface alone, temperature increases at a surface 1 mm away were confined to only 5 to 10 $^{\circ}\text{C}$.

Scanning electron microscopy

The ablation fluence of 3 J/cm^2 exhibits surface characteristics observed in slightly longer pulses of 350 fs (15). The lack of crumbling and clean crater edge illustrate this point and the high localization of the interaction processes with ultrashort pulse. The extremely smooth damage-free characteristics of the crater walls is clearly evident. Ablation crater walls demonstrated small granules a few micrometer in size. Exposed dentinal tubules and the lack of significant amount of melted dentin clearly indicate a lack of significant heating and the mechanical nature of the ablation process with fs pulses.

Enamel ablation is similar in appearance to that of dentin. The main difference is that in the range of 0.5 to 5 J/cm^2 dentin ablation results in larger deeper craters (see discussion of ablation rate below). Morphologically, ablated surface are very smooth, free of thermal damage or cracking.

Conclusion

Negligible collateral damage and highly efficient ablation rate per pulse in the ultrashort pulse regime was demonstrated. A comparison of 50 fs and 350 fs to pulses 1 ns long, clearly demonstrated the ultrashort pulse regime reduced sensitivity to material composition. The strong dependence of ultrashort pulse multi-photon interaction processes on threshold fluence, along with scanning electron micrographs illustrate a sharply defined ablation threshold and the highly precise spatial nature of the interaction. Analysis of our temperature increases during the interaction confirms expectations of relatively small temperature increases and confinement of thermal effects. Thus, the potential for an efficient, precise, and minimally damaged ultrashort pulse operation was demonstrated, offering hope for practical application of such devices in the near future.

References

1. Willenborg GC. Dental laser applications: emerging to maturity. *Laser Surg Med* 1989; 9:309-313.
2. Neev J, Goodis HE, and White JM. Thermal characteristics during Nd:YAG and carbon dioxide laser application on enamel and dentin *SPIE*, 1994.
3. White JM, Goodis HE, Setcos JC, Eakle WS, Hulscher BE, Rose, CL. Effects of pulsed Nd:YAG laser energy on human teeth: a three year follow-up study. *JADA* 1993; 124 : 45-51.
4. Hibst R, Keller U. Experimental studies of the application of the Er:YAG laser on dental hard substances: I. measurement of the ablation rate. *Laser Surg Med* 1989; 9:352-7.
5. Keller U, Hibst R. Experimental studies of the application of the Er:YAG laser on dental hard substances: II. Light microscopy and SEM investigations. *Laser Surg Med* 1989; 9:345-351.
6. Neev J, Liaw LL, Raney DV, Fujishige JT, Ho PT, and Berns MW. Selectivity and efficiency in the ablation of hard Dental tissue with ArF pulsed excimer lasers, *Laser Surg Med* 1991; 11:499-510.
7. Neev J, Stabholz A, Liaw LL, Torabinejad M, Fujishige JT, Ho PH, Berns MW. Scanning electron microscopy and thermal characteristics of dentin ablated by a short-pulse XeCl laser. *Laser Surg Med* 1993; 13: 3:353-361.
8. Neev J, Raney DV, Whalen WE, Fujishige JT, Ho PT, McGrann JV, and Berns MW. Dentin ablation with two excimer lasers: a comparative study of physical characteristics. *Lasers in the Life Sciences*, 4(3), 1992, pp. 1-25.

9. Wigdor HA, Walsh JT, Featherstone JDB, Visuri SR, Fried D, and Waldvogel JL. Lasers in Dentistry. *Laser Surg Med* 1995; 16: 103:133
10. Smith TA, Thomson JA, Lee WE. Assessing Patient Pain During Dental Laser Treatment. *JADA* Feb. 1993; 124:90-93
11. Milgrom P, Fiset L, Melnick S, Weinstien P. The Prevalence and Practice Management Consequences of Dental Fear in a Major US City. *JADA*. May 1988;116:641-647.
- 12 Niemz MH, "Cavity Preparation with the Nd:YLF Picosecond Laser", *J Dent. Res.*, 75, 1194-1199, May 1995.
- 13 Niemz MH Invited Paper, "Ultrashort Laser Pulses in Dentistry: Advantages and Limitations" These Proceedings.
- 14 Niemz MH, "Laser-Tissue Interactions: Fundamentals and Applications" Springer-Verlag, Berlin, Heidelberg, New York, (1996).
- 15 Joseph Neev, Luiz B. Da Silva, Michael D. Feit, Michael D. Perry, Alexander M. Rubenchik, and Brent C. Stuart; "Ultrashort Pulse Lasers for Hard Tissue Ablation" Invited paper, IEEE, Journal of Selected Topics in Quantum electronics, Vol.2, No.4 , 790--800, December 1996.
16. A.M. Rubenchik, L.B. daSilva, M.D. Feit, S. Lane, R. London, M.D. Perry, B.C. Stuart and J. Neev. "Dental Tissue Processing With Ultra-Short Pulse Laser" SPIE Proceedings, Progress in Biomedical Optics; 2672: pp 222-230; 1996.

SESSION 5

Diagnostics and Imaging with Ultrashort-Pulse Lasers

Optical parameters measurements by collimated light transmission

Alberto Colasanti, Giovanni Guida, Annamaria Kisslinger, Raffaele Liuzzi,
Maria Quarto, Giuseppe Roberti, Fulvia Villani

Faculty of Medicine and Surgery, University of Naples "Federico II"

ABSTRACT

Some medical applications involving the interaction between light and biological tissues require both the knowledge of optical characteristics of tissues and a realistic treatment of light transport into them. In this work we describe a transillumination technique testing water solutions of Intralipid by the transmitted radiation intensity. The experimental apparatus includes a diode laser ($\lambda_{\text{emiss}} = 820 \text{ nm}$), a detection fiber, a PMT and a Digital Signal Analyzer. The performances of this very simple and cheap system are comparable to those ones obtained with more sophisticated apparatus; the results show that this technique could represent a preliminary step toward the realization of an user-friendly and cheap laser system for measuring optical parameters of tissues.

Keywords: transillumination, Intralipid

1. INTRODUCTION

The research on the breast cancer by transillumination represents one of the most promising diagnostic application of light. The comprehension of phenomena that govern the interaction between light and biological tissues has an important part in the use of transillumination.

To describe the problem of light propagation in biological tissues, two different theories have been formulated: the analytical theory and the transport theory. The analytical theory, that bases on the Maxwell's equations, represents the most rigorous approach allowing, as a rule, to take into account the effects connected to the multiple scattering, the diffraction and the interference. However, the unawareness of dielectric characteristics of tissues and the mathematical difficulties make it useless in the practice. In the transport theory the energy transported by light is highly considered in spite of light wave nature. In this case, the optical behaviour of biological tissues is fixed by the scattering coefficient μ_s , the absorption coefficient μ_a and the phase function $p(\theta)$ [1]. In practice, a general solution of the transport equation isn't available yet. It is demonstrated that, in particular conditions, it is possible to get rough but simple enough analytical solution. In particular, the diffusion approximation is used to define the distribution of light intensity in a medium where the diffusion is dominant; this happens for the biological tissues in the so-called "therapeutic window", 700-1300 nm [2,3]. In fact, in this spectral range, where the largest penetration of light in the biological tissues (about 10 cm) is obtained, the scattering coefficient is much higher than the absorption one [3]; on this account we can assert the light attenuation in this spectral region is mainly due to the scattering that origins from the changes of the refractive index of connective tissue and cellular constituents, as membrans, cell organelles and nuclei [4].

In this work, we present measurements of spatial distribution of transmitted light through samples irradiated at 820 nm. The technique presented in this work, although very simple, could be used as an alternative to the time-resolved transillumination. In fact the light detection is performed with an optical fiber whose numerical aperture allows to select the less diffused photons. The effect of such a detection could be considered as that one obtained by reducing the time-gate in time-resolved techniques and allows to detect only the photons that covered the shortest paths.

2. MATERIAL AND METHOD

The experimental apparatus used for the trasmittance measurements is represented in Fig. 1. A continous laser beam emitted by a diode laser (Hamamatsu PLP02, $\lambda = 820 \text{ nm}$, CW = 0.1mW), after having been collimated thanks to an aspheric lens (NA = 0.50, effective focal = 2.00), hits the sample placed in a fixed position on a sample-holder.

The transmitted radiation was collected by a multimodal optical fiber (diameter core = 600 μm , NA = 0.4) whose head was moved in a vertical plane ortogonal to the laser beam direction by two computer controlled micrometric translators (Physik Instrument, travel range 5 cm, resolution 1 μm). The motion was performed along the vertical direction at a value of the horizontal coordinate corresponding to the center of the cuvette, for a travel equal to 3 cm at 600 $\mu\text{m/s}$ speed. The detection

has been carried out by a PMT (Hamamatsu R406) and a Digital Signal Analyser (Tektronix DSA602, sampling rate = 2 Gsample/s, bandwidth = 1 GHz).

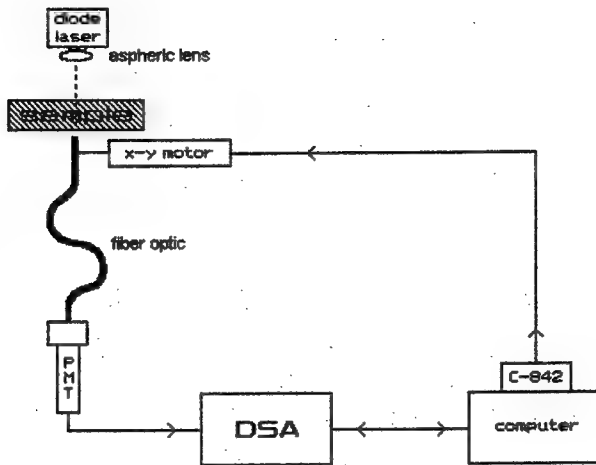


Fig. 1 Experimental set-up.

The samples have been obtained mixing suitable quantities of distilled water and Intralipid 10% (Farmacia, Italy) and placed in plastic cuvette (1 cm thick). The power measured on each sample has been normalized to the power transmitted through the same cuvette filled with distilled water. Since the refractive index of Intralipid solutions is very close to that one of the water, the normalization allows to disregard the reflections at the glass-air and glass-sample interfaces due to the discontinuity of the refractive index. To obtain the scattering and absorption coefficients of the samples, the spatial profile of transmitted intensity has been compared with the solutions of the diffusion equation in case the sample is irradiated by a collimated beam with a small diameter and gaussian spatial profile [5].

The Intralipid attenuation coefficient μ_t , has been determined thanks to the Beer's law by absorption measurements on diluted solutions placed in 0.5 cm thick cuvette to reduce multiple scattering effects. On the other hand, since Intralipid is a highly scattering medium (μ_a is several orders of magnitude smaller than μ_s), the μ_t value could be approximated to the μ_s value. The value obtained for the scattering coefficient is $\mu_s = (227 \pm 11) \text{ cm}^{-1}$. As far as the absorption coefficient is concerned, we choose the value equal to 0.003 cm^{-1} reported in literature [6]. Finally, for the anisotropy factor, we choose the value of 0.75, obtained by the extrapolation of literature data at 800 nm [6,7,8].

3. RESULTS AND DISCUSSION

The measurements of the power of the light transmitted by the analyzed water solutions of Intralipid as a function of the coordinate r which represents the vertical position of the fiber with respect to the intersection between the direction of laser beam and the scanning plane are reported in Fig. 2. The data are normalized as described above. The plots refer to four Intralipid-water concentration ratio (1:10, 1:15, 1:20 and 1:40). The solid line superimposed on the experimental data represents the solution of the diffusion equation obtained by using the μ_s and μ_a values obtained by the linear scaling of the values reported in the previous paragraph as a function of the concentration. The plots show a good agreement between the experimental and theoretical data. The normalized light power behaviour shows that the beam is highly attenuated mainly owing to the diffusion that spreads the photons away from the input direction, the beam broadening decreasing with decreasing Intralipid concentration.

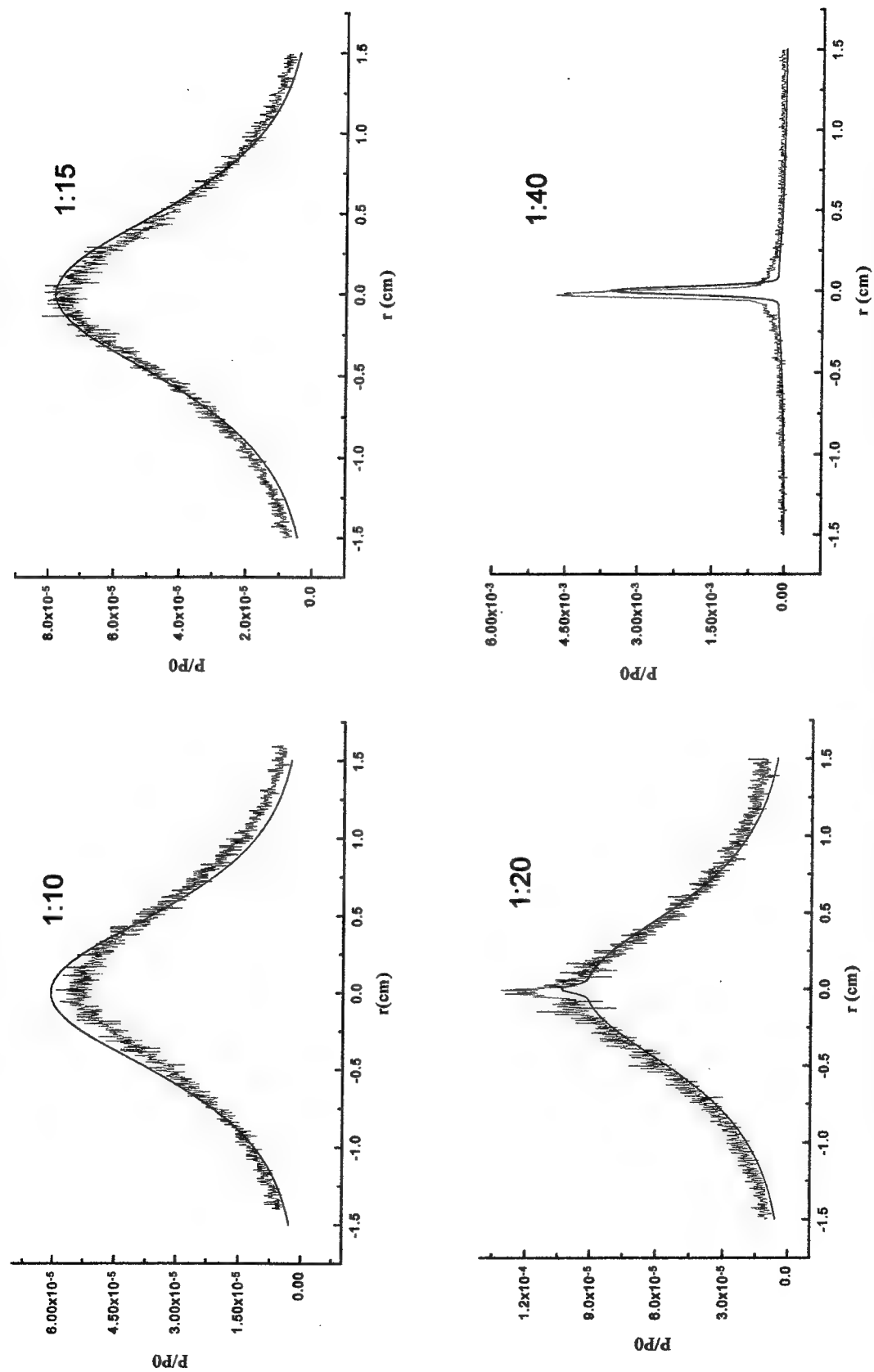


Fig. 2 - One-dimensional space dependence of light power transmitted by water solutions of Intralipid (thickness=1 cm) at different concentrations (labels on each plot represent the concentrations ratios water-Intralipid). P_0 is a normalization factor (see text for the explanation). The continuous smooth line is the theoretical curve obtained with the diffusion approximation.

4. REFERENCES

1. F. Bevilacqua, P. Marquet, O. Coquoz and C. Depeursinge, "Role of tissue structure in photon migration through breast tissue" *Appl. Opt.* **36**, pp. 44-51, 1997.
2. K. P. Chan, B. Devaraj, M. Yamada and H. Inaba, "Coherent detection technique in optical imaging of tissue" *Phys. Med. Biol.* **42**, pp. 855-860, 1997.
3. J. Mier, S. Walker and E. Gratton, "Frequency-domain optical spectroscopy and imaging of tissue" *Proc. NATO ASI Serie (E)* **235**, pp. 121-142, 1996.
4. H. Key, E. R. Davies, P. C Jackson and P. N. T. Well, Optical attenuation characteristics of breast tissue at visible and near-infrared wavelengths" *Phys. Med. Biol.* **36**, pp. 579-590, 1991.
5. U. Bernini, A. Ramaglia and P. Russo "Quasi-CW tissue transillumination at 1064 nm" *Proc. SPIE* **2979**, pp 688-696, 1996.
6. H. J. van Staveren, C. J. M. Moes, J. van Marle, S. A. Prahl and M. J. C. van Gemert, "Light scattering in Intralipid-10% in the wavelength range of 400-1100 nm" *Appl. Optic.* **30**, pp4507-4514, 1991.
7. S. T. Flock, S. L. Jacques, B. C. Wilson, W. M. Star and M. J. C. van Gemert, "Optical properties of Intralipid: a phantom medium for light propagation studies" *Las. Surg. Med.* **12**, pp. 510-519, 1992.
8. C. J. M. Moes, M. J. C. van Gemert, W. M. Star, J. P. A. Maijissen and S. A. Prahl, "Measurements and calculations of the energy fluence rate in a scattering and absorbing phantom at 633 nm" *Appl. Opt.* **28**, pp. 2292-2296, 1989.

Addendum

The following papers were announced for publication in this proceedings but have been withdrawn or are unavailable.

- [3255-02] **Transparent media**
A. L. Gaeta, J. Ranka, Cornell Univ.
- [3255-04] **Pressure and temperature evolution induced by ultrashort-laser-pulse ablation**
A. M. Rubenchik, L. B. Da Silva, M. D. Feit, B.-M. Kim, M. D. Perry, B. C. Stuart, Lawrence Livermore National Lab.
- [3255-06] **Ultrashort-laser-pulse propagation through hollow-core fibers**
M. D. Feit, B.-M. Kim, L. B. Da Silva, A. M. Rubenchik, B. W. Shore, Lawrence Livermore National Lab.
- [3255-10] **Refractive surgical applications with ultrashort-pulse lasers**
T. Juhasz, Univ. of Michigan; C. Horvath, Univ. Heidelberg (FRG); H.-H. Liu, R. M. Kurtz, Univ. of Michigan
- [3255-17] **Ultrafast laser sources for optical coherence tomography**
B. E. Bouma, G. J. Tearney, S. A. Boppart, L. E. Nelson, D. J. Jones, C. Pitris, J. Herrmann, Massachusetts Institute of Technology; M. E. Brezinski, Massachusetts General Hospital; J. G. Fujimoto, Massachusetts Institute of Technology
- [3255-20] **Real-time 2-photon confocal microscopy**
M. Müller, A. H. Buist, G. J. Brakenhoff, Univ. of Amsterdam (Netherlands); J. A. Squier, D. N. Fittinghoff, K. R. Wilson, Univ. of California/San Diego
- [3255-21] **Novel image reconstruction algorithm in optical mammography**
M. V. Klibanov, T. R. Lucas, Univ. of North Carolina/Charlotte

Author Index

Amnote, Rodney E., 50
Anufrik, Slavomir S., 98
Artsukevich, Irine M., 98
Birngruber, Reginald, 34
Boppart, Stephen A., Addendum
Bouma, Brett E., Addendum
Brakenhoff, G. J., Addendum, 8, 18
Brezinski, Mark E., Addendum
Buist, Arjan H., Addendum, 18
Cain, Clarence P., 50
Chernikovich, Ivan P., 98
Chiu, Eric K., 77
Colasanti, Alberto, 118
Da Silva, Luiz B., Addendum, 92
Darrow, Christopher B., 92
Druessel, Jeffrey J., 50
Eilert, Brent, 50
Feit, Michael D., Addendum, 92
Fenn, Ralph, 67
Fittinghoff, David N., Addendum, 22
Fujimoto, James G., Addendum
Gaeta, Alexander L., Addendum
Gold, D. M., 92
Guida, Giovanni, 118
Hammer, Daniel X., 34, 50
Herrmann, J., Addendum
Hopkins, Richard A., 50
Horvath, Christopher, Addendum, 56
Jones, David J., Addendum
Juhasz, Tibor, Addendum, 56, 67
Jumper, J. Michael, 77
Kennedy, Paul K., 50
Kim, Beop-Min, Addendum, 92
Kisslinger, Annamaria, 118
Klibanov, Michael V., Addendum
Kurtz, Ron M., Addendum, 56, 67
Liu, Hsiao-Hua, Addendum, 56
Liuzzi, Raffaele, 118
Loesel, Frieder H., 67
Lucas, Thomas R., Addendum
Makarchikov, Alexander F., 98
Marion, John E., 92
Maskevich, Alexander A., 98
Mourou, Gerard A., 67
Müller, Michiel, Addendum, 8, 18
Nahen, Kester, 34
Neev, Joseph, 2, 105
Nelson, Lynn E., Addendum
Niemz, Markolf H., 84
Noack, Joachim, 34
Noojin, Gary D., 34, 50
Ostrovtsova, Svetlana A., 98
Payne, Dale J., 50
Perry, Michael D., Addendum
Phillips, Shana L., 50
Pitrис, Constantino, Addendum
Quarto, Maria, 118
Ranka, Jayshree, Addendum
Roach, William P., 50
Roberti, Giuseppe, 118
Rockwell, Benjamin A., 34, 50, 77
Rubenchik, Alexander M., Addendum, 92
Sacks, Zachary S., 67
Shore, Bruce W., Addendum
Simon, Ulrich, 8, 18
Squier, Jeff A., Addendum, 8, 18, 105
Stepuro, Vitali I., 98
Stolarski, David J., 50
Stuart, Brent C., Addendum
Tearney, Guillermo J., Addendum
Theisen, Dirk, 34
Thomas, Robert J., 50
Toth, Cynthia A., 50, 77
Villani, Fulvia, 118
Vogel, Alfred, 34
Volodenkov, Alexander P., 98
Wilson, Kent R., Addendum
Yakovlev, Vladislav V., 18